2016-03-01

Novel Sputtered Stationary Phases for Solid Phase Microextraction, and Other Coatings and Materials for Surface Applications

Anubhav Diwan
Brigham Young University

BYU ScholarsArchive Citation

Diwan, Anubhav, "Novel Sputtered Stationary Phases for Solid Phase Microextraction, and Other Coatings and Materials for Surface Applications" (2016). *All Theses and Dissertations*. 6204.
https://scholarsarchive.byu.edu/etd/6204

Novel Sputtered Stationary Phases for Solid Phase Microextraction, and Other Coatings and Materials for Surface Applications

Anubhav Diwan

A dissertation submitted to the faculty of
Brigham Young University
in partial fulfillment of the requirements for the degree of

Doctor of Philosophy

Matthew R. Linford, Chair
Milton L. Lee
Jaron C. Hansen
Adam T. Woolley
Robert C. Davis

Department of Chemistry and Biochemistry

Brigham Young University

March 2016

ABSTRACT

Novel Stationary Phases for Solid Phase Microextraction and Surface Coatings for Various Applications

Anubhav Diwan
Department of Chemistry and Biochemistry, BYU
Doctor of Philosophy

The primary focus of my work has been to prepare new solid adsorbents for solid phase microextraction (SPME) via sputtering of silicon. The orientation of the silica substrates/fibers and the sputtering pressure induced the formation of porous and columnar structures. Sputtering was performed for different times to yield fibers with different thicknesses. Piranha treatment of the surface increased the concentration of silanol groups, which underwent condensation with vapor deposited octadecyldimethylmonomethoxy silane to incorporate octadecyl chains onto the fiber surfaces. Silanized, sputtered fibers were preconditioned for 3 h at 320 °C to remove the unreacted chains. Comparison of the extraction efficiencies of 1.0 and 2.0 µm sputtered, silanized fibers with a commercial fiber (7 µm PDMS) for a series of analyte mixtures, which included alkanes, alcohols, aldehydes, esters, and amines, was demonstrated. The silanized, sputtered fiber performed better than the commercial fiber in extraction of most of the compounds. These fibers demonstrated long life as no degradation was seen even after 300 extractions. Carry-over between runs was not observed. The repeatability of the sputtered fibers was similar to commercial ones. The extraction of more than 50 compounds from a real world botanical sample using the 2.0 µm sputtered, silanized fiber was also demonstrated.

In my second project, a facile method for the preparation of superhydrophobic surfaces (SHS) on glass and silicon surfaces was developed. A two-tier topography (needed for an SHS) was created in 60 min by the aggregation of nanosilica during *in situ* urea-formaldehyde polymerization. Scanning electron microscopy (SEM) and atomic force microscopy (AFM) demonstrated rough topography. Vapor deposition of a low surface energy silane imparted hydrophobicity, which was confirmed by the presence of an F 1s signal in X-ray photoelectron spectroscopy (XPS). The prepared surfaces exhibited water contact angles (WCA) of greater than 150 °C with very low sliding angles.

In my third project, a multilayer assembly of nitrilotris(methylene)triphosphonic acid, a corrosion inhibitor, and zirconium was constructed on alumina at room temperature. Attempts to prepare a layer-by-layer assembly at higher temperature (70 °C) was unsuccessful due to etching of the alumina surface. A suite of analytical techniques, XPS, AFM, time-of-flight secondary ion mass spectrometry, and spectroscopic ellipsometry was used to characterize these surfaces.

This thesis also contains appendices of tutorial articles I wrote on modeling in ellipsometry, and data analysis tools (classical least squares and multivariate curve resolution).

Keywords: Solid phase microextraction, surface coatings, superhydrophobic surface, layer-by-layer

ACKNOWLEDGEMENTS

I would like to thank Dr. Matthew R. Linford for his mentorship, encouragement, and insightful discussions. I am grateful to have worked under his supervision.

I am thankful to my committee members: Dr. Milton L. Lee, Dr. Jaron H. Hansen, Dr. Adam T. Woolley, and Dr. Robert C. Davis for their valuable suggestions and insights throughout my graduate work.

I appreciate and acknowledge all my friends and labmates: Dr. Chuan-Hsi Hung, Dr. Landon Wiest, Dr. Supriya S. Kanyal, Dr. David S. Jensen, Hao Wang, Cody Cushman, Tuhin Roychowdhury, Anupriya, Shiladitya Chatterjee and Varun Jain for their support and help. I would like to thank Dr. Nitesh Madaan for teaching analytical instruments to me. I have worked on multiple projects with Dr. Bhupinder Singh and would like to acknowledge him for making the graduate life memorable.

In addition, I would like to thank, P2i and Moxtek Inc., for helping my research financially. I would also like to thank Fred Lane, Eric Gardner and Brian Bowers for their support. I am deeply thankful to the Department of Chemistry and Biochemistry for giving me the opportunity to pursue my graduate studies at Brigham Young University.

I would like to thank my parents, Dr. Rajinder Kumar Diwan and Mrs. Ritu Diwan, my brother, Abhinav Diwan, my sister-in-law, Ite Diwan, and my niece, Amaira Diwan for their love and support during all these years. I would like to dedicate my dissertation to my parents.

TABLE OF CONTENTS

Chapter 2 Porous, High Capacity Coatings for Solid Phase Microextraction (SPME) by Sputtering* 43

LIST OF TABLES

LIST OF FIGURES

LIST OF ABBREVIATIONS

AFM	Atomic force microscopy
CB	Cassie-Baxter
CLS	Classical least squares
CVD	Chemical vapor deposition
EDX	Energy-dispersive X-ray spectroscopy
FTIR	Fourier transform infrared spectroscopy
HS	Headspace
LBL	Layer-by-layer
LLE	Liquid-liquid extraction
MCR	Multivariate curve resolution
NTMP	Nitrilotris(methylene)triphosphonic acid
OAD	Oblique angle deposition
PVD	Physical vapor deposition
PA	Phosphonic acid
SAM	Self-assembled monolayer
SE	Spectroscopic ellipsometry

SEM	Scanning electron microscopy
SFE	Supercritical fluid extraction
SHS	Superhydrophobic surface
SPE	Solid phase extraction
SPME	Solid phase microextraction
TEM	Transmission electron microscope
ToF-SIMS	Time-of-flight secondary ion mass spectrometry
UF	Urea-formaldehyde
WCA	Water contact angle
XPS	X-ray photoelectron spectroscopy
XRD	X-ray diffraction

Chapter 1 Introduction*

1.1 Introduction to Surface Engineering

Surface engineering is a broad scientific term that encompasses the design and formation of surface layers, investigation/characterization of surfaces, and their utilization for various applications.[1] In addition to information about the coating, a fundamental understanding of the substrate/core material is of singular importance in this type of work.[1] Surface engineering is critical for many industries as it leads to the development of products with properties that are essential/needed for specific applications. Engineered surfaces have found many uses in such areas as corrosion resistance, anti-wear materials, hydrophobic and hydrophilic surfaces, adhesion, catalysis, optics, microfluidics, and biomedicals.[2] Advancing the technology, new tools and methods have been introduced to tailor/engineer surfaces. These include physical vapor deposition (PVD), chemical vapor deposition (CVD), electroplating, ion implantation, plasma processes, laser treatment, photolithography, spin coating, etching processes, sol-gel processes, self-assembled monolayers (SAM), layer-by-layer assemblies (LBL), and so on.[1, 3] Because engineered surfaces have become a necessity for so many industries, improvements in metrology have also been needed. Nowadays, numerous analytical tools can be employed to obtain both physical and chemical information about surfaces. Imaging at the nanometer scale can be performed by scanning electron microscopy (SEM), transmission electron microscopy (TEM), and atomic force microscopy (AFM).[3] Analytical tools such as X-ray photoelectron spectroscopy (XPS), time-of-flight secondary ion mass spectroscopy (ToF-SIMS), energy-dispersive X-ray spectroscopy

*Some of the sections of this chapter were taken, sometimes verbatim, from the introductory paragraph of Chapters 2-4 of this thesis. Permission was obtained from the publishers of the documents to reproduce the introductions of the papers reworked herein. See individual chapters in this thesis.

(EDX), and Fourier transform infrared spectroscopy (FTIR) provide information about the chemical make-up of surfaces.[3] X-ray diffraction determines the crystallinity of materials. The thicknesses and optical properties, e.g., refractive index and extinction coefficent, of thin films and coatings can be obtained by spectroscopic ellipsometry.[3] Wetting or water contact angle measurements are used to determine whether the surface is hydrophilic or hydrophobic.[2-3] Physical parameters such as hardness,[2, 4] residual stress,[4] adhesion,[2, 4] and corrosion resistance [2, 4] can be evaluated using other tests.[4] It is important to emphasize here that a single analytical tool is almost always incapable of yielding complete information about a surface. Therefore, a suite of analytical tools needs to be employed in surface/material analysis.[5]

I have worked on three projects in which I have engineered and characterized surfaces that can be employed for different applications. These projects are (i) preparation of novel solid adsorbents for solid phase microextraction (SPME), (ii) superhydrophobic surfaces prepared via aggregation of silica nanoparticles during *in situ* urea-formaldehyde polymerization, and (iii) construction of a multi-layer assembly using an aminophosphonate and zirconium. The majority of my time and effort was spent on the first project. The common aspects among all these projects were the manipulation of surface chemistries, followed by their characterization with several analytical tools.

1.2 Novel Stationary Phases for Solid Phase Microextraction via Sputtering

1.2.1 Review of Different Extraction Methods

Various methods are used for extracting organic compounds from solid and liquid matrices. For example, liquid-liquid extraction (LLE) is used to extract soluble organic compounds from solutions,[6] and Soxhlet and ultrasonic extraction are used to extract molecules from solid organic matrices.[6] In many cases, these methods require large volumes of high purity organic solvents. These solvents are often carcinogenic and/or expensive – both to purchase and to dispose of. Moreover, these extractions can involve multiple steps that are time consuming and can lead to loss of analytes.[6-7] It is not unusual for sample preparation to take hours and in some cases days. There are other extraction methods that require less organic solvent. These methods can be broadly classified on the basis of the extraction medium. They comprise:[6]

(i) Gas phase extraction,[6] which includes headspace GC, the purge and trap method, and supercritical fluid extraction (SFE). The instrumentation for the latter two methods is expensive and somewhat difficult to use, whereas for the former approach, the lack of preconcentration of the analytes is the main drawback.

(ii) Membrane extraction,[6] which involves analyte extraction through a polymeric membrane. This method is applicable to volatile compounds but cannot be applied to polar analytes due to a lack of selective membranes.

(iii) Sorbent extractions,[6] which include solid phase extraction (SPE) and solid phase microextraction (SPME). In SPE, the sample mixture in solution form is passed through a bed of stationary phase. The analytes are retained on the stationary phase and later eluted using a small volume of solvent, which helps preconcentrate the analytes. It can be used for polar as well as non polar compounds.[6-7] SPME is a technique that does not require a solvent for extraction.[6-7] It was developed in 1990 by Pawliszyn and Arthur.[6, 8-9] Since then the technique has been widely used for extraction of numerous compounds. SPME has several advantages over conventional techniques. For example, sampling, enrichment, and extraction can be performed in a single step. It is a fast, simple, environmental friendly, relatively cheap technique that involves fibers that can be used multiple times.[9-11] As a non-exhaustive extraction technique, it has many uses, e.g., it can be used to monitor unbound drug fractions in living organisms.[12] It can also be used for field applications.[7]

1.2.2 Stationary phases for SPME

Generally, SPME extraction is performed via an open bed method that includes the use of fibers, vessels coated with stationary phase, or an in-tube method wherein the inside of a capillary is coated with the stationary phase.[7] This approach using solid substrates or fibers coated with stationary phase has been the main focus of research and practical application for several years. The stationary phase of the coated fibers can be either a liquid or a solid depending on the application, and the mechanism of extraction is different for these two types of phases.[13-14] Absorption occurs primarily in the extraction of analytes with liquid stationary phases.[13] The attainment of equilibrium signals the completion of the extraction process. This results in linear isotherms. The main disadvantage of absorption extraction is longer extraction times.[13-14] For solid stationary phases, adsorption is the main process. [13]Accordingly, analyte extractions are faster. However, these extractions are greatly affected by higher analyte concentrations, which lead to saturation of the fiber and results in competitive adsorption.[13-14] Nevertheless, a solid phase provides faster extraction, better selectivity, and it can be used for polar compounds.[13-14]

1.2.3 Modes of SPME

SPME extraction can be performed using three different approaches: a) direct sampling, b) head space (HS) extraction, and c) extraction with a membrane-protected stationary phase.[15] In direct sampling, the fiber is directly introduced into the analyte sample. This approach generally requires agitation by sonication or stirring to remove the boundary layer around the fiber for better analyte extraction. It is important for extraction of non-volatile compounds with high polarity.[13] The headspace method is mostly preferred for volatile and low-polarity compounds. It may be performed at room temperature or with sample heating or sonication to allow analytes to diffuse/partition into the headspace. HS-SPME protects the fiber from the adverse effects of pH and/or dirty sample matrices, which helps ensure long lifetimes for the fiber.[13, 16] The third sampling method involves use of a membrane, which is coated around the stationary phase. The membrane acts as a molecular sieve, allowing only molecules of a specific size to pass through it. This approach helps in the extraction of nonvolatile analytes from complex matrices and also protects the stationary phase from deterioration.[13]

1.2.4 Theory of SPME

SPME involves extraction of analytes from an aqueous solution or its headspace using a stationary phase of specified thickness coated on a solid support. The process involves transfer of an analyte from a solution to a stationary phase until equilibrium of the analytes is established between them.[13] The amount/mass of analyte extracted by the stationary phase at equilibrium for an SPME process (mainly for liquid stationary phases) is:[6, 13, 15]

$$n = K_{fs}V_fV_sC_o/K_{fs}V_f + V_s \tag{1.1}$$

where K_{fs} is the distribution constant of the analyte between the fiber coating and the sample matrix, C_o is the initial concentration of a given analyte in the sample, and V_f and V_s are the volumes of the fiber coating and the sample, respectively.

In the case of large sample volumes, the denominator in Equation 1.1 becomes V_s and Equation 1.1 reduces to:[6, 13, 15]

$$n = K_{fs}V_fC_o \tag{1.2}$$

Hence, the amount of extracted analyte does not depend on the sample volume, which makes this approach particularly important in portable field devices.[6, 13, 15] This theory was developed by Pawliszyn and is only applicable to liquid stationary phases such as PDMS and polyacrylate.[15] In certain cases, however, it can be applied to solid adsorbents when the concentration of analyte to be extracted is small.[13-14]

Gorecki et al.[14] described the process of extraction of analytes onto porous solid adsorbents using the Langmuir adsorption isotherm. Their theory encompasses PDMS-DVB, Carbowax-DVB, and Carbowax-TR as stationary phases, but it cannot be applied to the Carboxen stationary phases because their pore size is very small, which results in capillary condensation.[14, 17] The assumptions of the Langmuir adsorption isotherm are: (i) a single binding site for a single analyte molecule, i.e., only a monolayer of analyte can be deposited on the stationary phase, (ii) adsorbed analyte molecules are not free to move on the stationary phase, (iii) all binding sites on the stationary phase are equivalent, and (iv) adsorbed analytes at different binding sites are noninteracting. According to this theory, the amount of analyte adsorbed by the solid adsorbent at equilibrium is:[14]

$$n = K_AC_{OA}V_sV_f(C_{fmax} - C_{fA}^{\infty})/(V_s + K_AV_f(C_{fmax} - C_{fA}^{\infty})) \tag{1.3}$$

where K_A is the adsorption equilibrium constant, C_{OA} is the starting/initial concentration of the analyte in the sample solution, C_{fmax} represents the maximum concentration of active sites on the solid stationary phase, C_{fA}^{∞} represents the equilibrium concentration of the analyte on the solid stationary phase, and V_s and V_f are the volume of the sample and solid stationary phases, respectively.

The concentration of the analyte on the fiber at equilibrium is given as:[14]

$$C_{fA}^{\infty} = K_A C_{fmax} C_{sA}^{\infty} / (1 + K_A C_{sA}^{\infty}) \quad (1.4)$$

where C_{sA}^{∞} represents the equilibrium concentration of the analyte in a sample.

It can be seen that when $K_A C_{sA}^{\infty}$ is small, $C_{fA}^{\infty} = C_{fmax}$. This occurs only when the analyte's affinity is low towards the stationary phase or when the analyte concentration in the sample is very low.

To account for real life situations where there is more than one analyte present in the sample matrix and where they compete for extraction, Gorecki et al. provided the following expression:[14]

$$C_{fA}^{\infty} = K_A C_{fmax} C_{sA}^{\infty} / (1 + K_A C_{sA}^{\infty} + K_i C_{si}^{\infty}) \quad (1.5)$$

where K_i is the adsorption constant of each interfering compound and C_{si}^{∞} is the equilibrium concentration of interfering compounds in the sample solution.[14]

When the concentrations of analytes are high, shorter extraction times should be employed to avoid the loss of selectivity due to competitive adsorption. Competitive adsorption occurs when all the sites of the stationary phase are occupied, which leads to replacement of lower affinity compounds by higher affinity ones.[13] The amount of analyte extracted over the sampling time (t) is given by:[13, 18]

$$n(t) = 2\pi D_g L C_g t / \ln(b + \delta / b) \quad (1.6)$$

where D_g is the diffusion coefficient of the analyte in the gaseous phase, L is the length of the rod coated with stationary phase, b is the outer radius of the coated fiber, C_g is the concentration of analyte in bulk air, and δ is the boundary layer thickness formed outside the coated fiber. Hence, short sampling times can be used to prevent competitive adsorption, and the extraction process can be performed in a linear adsorption range.[13]

1.2.5 Shortcomings of Commercial Fibers and Recent Developments in SPME

The commercially available SPME fibers provided by SUPELCO are expensive,[9, 19-20] have relatively short life times,[19-22] and often show applicability to limited numbers of compounds.[9, 19, 22] As a result, there has been an increase in interest in homemade SPME fibers prepared from different materials such as graphene,[8-9, 23] carbon nanomaterials,[8-9] ionic liquids,[9] polymeric ionic liquids,[8-9] molecularly imprinted polymers,[9] conductive polymers,[8-9, 20] functionalized silica,[8, 22, 24-25] and metallic nanoparticles.[8-9, 26-29] These custom-made phases are immobilized on different solid substrates by sol-gel chemistry[9], electrochemical deposition,[20, 30-31] physical deposition,[9] and sometimes even using a thermally stable glue[9, 19, 24, 32]. Some of the stationary phases for SPME are porous solids, which provide high surface areas for extraction, increased adsorption capacity, and faster analysis[19, 28, 30, 33-34] Because of the advantages of solid phase SPME fibers, there has been increased interest in this area. Various nanoporous SPME coatings have been synthesized from CMK-1,[8, 33] CMK-3,[8, 19] MCM-48,[8] C_{16}-MCM-41,[35] carbon nanotubes,[8-9] graphene,[8-9, 23] SBA-15,[8-9, 24] anodic alumina,[8, 34] and zinc oxide nanorods.[8, 26, 29] These adsorbents show improved extraction efficiency and thermal stability. However, the preparation of these coatings has been cumbersome. For example, the preparation of anodic alumina required an 8 h oxidation step, followed by a long drying process.[34] The syntheses of CMK-1[33], C_{16}-MCM-41[35] and SBA-15[24] nanoparticles involved difficult, time consuming synthetic procedures. Moreover, carbon based coatings are difficult to functionalize and so are not easily adapted to the extraction of compounds with varying polarity.

1.2.6 Sputtering

In consideration of the points listed above, there is a need for a robust coating for SPME that will be highly porous, operate over a wide temperature range, be relatively thin, be strongly bonded to its fiber surface, be created in a straightforward and reproducible manner, not swell in organic solvents, and be stable under diverse working conditions and therefore enjoy a long life. Sputtering is the most extensively used thin film vacuum deposition method in industry. It is safe and reproducible. Sputtering functions by the ejection of atoms from a target by collisions with energetic ions from a plasma. In general, sputtered films show excellent adhesion to their substrates.[21, 36] However, sputtering is not well known among many university researchers, especially chemists, probably because it is an industrial technique, and less expensive vapor deposition apparatuses, e.g., thermal and electron beam, are often available at universities and adequate for many academic projects. Nevertheless, thermal and electron beam vapor deposition systems are not well suited for most industrial applications because their deposition rates (i) tend to be low and (ii) are strongly influenced by any variation in the temperature of the material being deposited through its vapor pressure. Rossnagel described the extent to which sputtering is employed in the semiconductor industry as follows: “[Sputtered] layers are used as diffusion barriers, adhesion or seed layers, primary conductors, antireflection coatings, and etch stops.”[37] Sputtering has played a significant role in the manufacturing of almost every optical disc (CD, DVD, and Blu-ray) that has ever been made (many billions), where sputtered films include reflective layers, dielectric layers, and/or read/write (data storage) films.[38-40] As the third of many possible examples, series of sputtered coatings are regularly applied in very large vacuum systems to commercial window glass, often to improve its energy performance. Because sputtering has been widely used to create relatively inexpensive commercial products, we believe that it will be possible to manufacture sputtered SPME coatings in an economical fashion. Sputtering has also been used to develop materials for catalysis, optical devices, biochip arrays, and sensing devices.[41-42] However, it has not been reported for making stationary phases for SPME. The only paper we are aware of that in any way connects sputtering to SPME is from Liu and coworkers,[21] who used sputtering to deposit an adhesion layer onto a stainless steel fiber onto which their SPME bonded phase of multi-walled carbon nanotubes was deposited. Here, the authors stated that their sputtered adhesion layer had *not* influenced the extraction performance of their SPME device.

Various parameters in a physical vapor deposition influence the resulting film microstructure. For example, if the substrate is cold enough that the atoms that strike it have little or no mobility after they impinge on the surface (limited adatom diffusion),[43-44] and if the flux of atoms strikes the material at an oblique angle, a porous, typically columnar, structure is obtained due to shadowing effects.[45-46] Shadowing refers to the process by which surface features shield their neighbors from incoming vapor flux. In his description of these processes, Thornton noted that: “Shadowing induces open boundaries because high points on the growing surface receive more coating flux than valleys, particularly when a significant oblique component is present in the flux”.[47] Shadowing can be promoted in different ways. One possibility, oblique angle deposition (OAD), involves a low chamber pressure and a shallow angle between the substrate and the incoming flux of atoms. Alternatively, with appropriate substrate geometry, shadowing can occur at relatively high chamber pressures, where the higher pressure will reduce the mean free paths (directionality) of impinging atoms so that they ultimately approach the substrate at multiple angles.

1.3 Preparation of Superhydrophobic Surface Using a Urea-Formaldehyde-Nanosilica Composite and a Hydrophobic Silane

1.3.1 Background Information

Nature provides numerous examples of superhydrophobic surfaces (SHS) including the lotus leaf,[48-61] duck feathers,[51] butterfly wings,[48, 51] rice leaves,[49] and the legs of water striders.[50, 56] These surfaces/materials have water contact angles greater than 150° and very low sliding angles – the angle at which a droplet of water of a given mass slides down an inclined surface.[62] Significant insights into superhydrophobic surfaces were revealed in the study of Barthlott and Neinhuis on the lotus leaf, which emphasized the significance of two-tier topography. The combination of a two-tier topography and a hydrophobic coating results in the Lotus effect.[48-54] Accordingly, the main requirements for an SHS material are surface roughness and a low surface energy material.[48-51, 54, 56-58, 60, 63-64] Preparations of SHS have been broadly classified as (i) preparation of a rough surface followed by deposition of a low surface energy material and (ii) the use of a low surface energy material that is roughened.[48-49, 51, 57, 63] In this work we take the first of these two approaches. Recently, various research groups have mimicked the lotus leaf's hierarchical structure to prepare SHS.[52, 56-57, 59-61, 63]

1.3.2 Hydrophobicity of Rough Surfaces

The Wenzel and Cassie-Baxter (CB) wetting regimes are commonly used to explain the hydrophobicity of rough surfaces.[48, 50-51, 54-55, 57, 59, 61, 63-64] In the Wenzel state, water droplets are pinned on a rough surface, which they fully wet, resulting in low receding angles and high hysteresis.[50, 54-55, 57, 59, 61, 63-64] The Wenzel state is defined as:

$$\cos\theta_w = r_w \cos\theta \tag{1.7}$$

where θ_w is the apparent (measured) water contact angle, r_w is the roughness factor, which is a ratio of the actual surface area to the projected surface area, and θ is the water contact angle of the same material on a hypothetical smooth surface.

In the CB state, the water droplets make contact with the substrate and another material, i.e., entrapped air. This state can be defined as:

$$\cos\theta_{CB} = f_1\cos\theta_1 + f_2\cos\theta_2 \tag{1.8}$$

where θ_{CB} is the apparent (measured) water contact angle, f_1 and f_2 are the surface fractions of the probe droplet in contact with the solid and air, respectively, and θ_1 and θ_2 are the contact angles of the homogeneous, planar surfaces representing the solid and the air, respectively. This effect results in high receding angles and lower sliding angles.[50, 54-55, 57, 59, 61, 63-65] The lotus effect can be considered as a special case of the CB state with very low contact angle hysteresis.[55] By adding in a roughness term, r_{CB} (defined as r_w above), for the portion of the droplet that makes contact with the surface, taking the contact angle of water on air, θ_2, to be 180°, and assigning $f_1 = f$ and $f_2 = 1 - f$, one obtains the more specific statement of the CB effect as:[66]

$$\cos\theta_{CB} = r_{CB}f\cos\theta_1 + f - 1 \tag{1.9}$$

1.3.3 Urea-Formaldehyde Polymer

Urea-formaldehyde (UF) polymers have been employed for many years in various industries, e.g., the wood panel industry,[67-70] where their ease of polymerization, high reactivity and low cost are important advantages.[67-70] However, UF polymers release formaldehyde and are susceptible to moisture.[69-70] Nanosilica has been added to UF polymers to improve their mechanical properties.[67-68] That is, some researchers have suggested that silanol groups from the nanosilica form hydrogen bonds with the UF resin, which would impart mechanical strength to the adhesive.[67-68, 70] Recently, Roumeli et al. reported the aggregation of silica particles with increasing silica concentration in UF - nanosilica resin,[67] and Chen et al. used a UF polymer and nanosilica for the preparation of superficially porous particles.[71]

1.3.4 Applications and Different Methods of Preparation of Superhydrophobic Surfaces

SHS have been employed in numerous applications such as self-cleaning surfaces,[48-51, 55, 57, 63-64] antibiofouling paints,[50-51] anti-icing coatings on windows and antennas,[49-50, 54] waterproof clothes,[48, 50-51, 60] anti-reflective coatings for optical windows,[51] for fluidic drag reduction,[51] and for separation of oil and water.[49, 51] Various research groups have used silica nanoparticles to prepare SHS by dip coating,[56, 72] electrostatic layer-by-layer deposition,[57-58, 63] sol gel processing,[64] and wet impregnation in carbon fabric composites.[59] SHS have also been prepared by coating cotton textiles with epoxy or amine functionalized silica nanoparticles,[60] and by sputtering in combination with silica colloidal assemblies.[61] Coating surfaces with nanosilica followed by calcination or sintering at high temperatures has been an effective method for preparing robust coatings.[56-59, 61] In chapter 3, I demonstrate for the first time the formation of SHS via the polymerization of urea and formaldehyde in the presence of nanosilica and a planar substrate. This work differs in a fundamental way from most of the studies in this area that have used silicon nanoparticles in that these studies tend to use either a standard or a modified Stöber process to prepare their superhydrophobic surfaces. The Stöber process,[73] in general, uses a silicate ester such as tetraethyl orthosilicate which acts as a precursor in a solution containing ethanol, ammonium hydroxide, and water for the synthesis of silica particles. The synthesized silica particles are hydrophilic, which are treated with a hydrophobic silane,[74-76] or they can be made hydrophobic using precursors such as methyl trimethoxy silane.[77-78] Modification of a surface with an alkyl monolayer can significantly change its properties, and much work has been done in this area to understand these systems.[79-82] Some of the other processes for making SHS involve the use of a polymer and hydrophobic silica to prepare hydrophobic surfaces. In these processes, a polymer such as polyisobutylene or polycaprolactone is mixed with hydrophobic silica in an organic solution. Substrates are then dip coated with this solution to yield superhydrophobic surfaces.[83-84] The preparation reported in chapter 3 results in the aggregation of silica nanoparticles and a textured surface, where this aggregation and surface roughness increase with increasing polymerization time. After hydrophobization with a silane adsorbate, the resulting surfaces show extremely high advancing and receding water contact angles and very low hysteresis. Chemical vapor deposition of silanes,[85-87] which is employed herein, as opposed to the liquid phase deposition of silanes, which is more common,[88-90] is an important and reproducible approach for deposition of these useful reagents.

Table 1.1 provides a summary of reports in the literature on the use of silica particles in superhydrophobic surfaces. The purpose of this tabular format is to be able to more directly compare the papers vis-à-vis their methods of coating, resulting water contact angles, particle size of the silica employed, materials used, and substrate.

Table 1.1 Summary of reports in literature using silica particles to prepare SHS.

Title	Method of Coating	Water contact angle (WCA)(º)	Particle size	Materials used	Substrate	Ref no.
Facile fabrication of superhydrophobic films with fractal structures using epoxy resin microspheres	Epoxy resin and polyamide was dissolved in a hydrophobic silica sol which was dripped on substrates followed by curing to form SHS.	Curing time of solution > 9 h WCA(4 µL) > 158° Sliding angle (9 µL) < 5°	Colloidal silica particles in sol before use were 40 -80 nm in size	Hydrophobic polyamide, hexamethyldisilazane, epoxy resin, and tetraethoxysilane (TEOS)	Glass	91
Superhydrophobic dual-sized filler epoxy composite coatings	Ultrasonic mixing of all materials, casting on microscopic slides, followed by sandblasting, RF etching and hydrophobization.	WCA - 152° Hysteresis - 8°	Alumina (11 ± 3 nm) Silica (26 ± 7 µm)	Diglycidyl ether of bisphenol-A epoxy resin, amine hardener, alumina nanoparticles, silica, and 1H,1H,2H,2H-perfluorodecyltrichlorosilane	Microscopic slides	92
Fabrication of superhydrophobic fabric coating using microphase-separated dodecafluoroheptyl-containing polyacrylate and nanosilica	Dip Coating method was used Nanosilica coated cotton fabric was dip coated with dodecafluoroheptyl-containing polyacrylate (DFPA).	With DFPA: 138.5° With DFPA + nanosilica - 153.6°	Silica (20-30 nm)	Dodecafluoroheptyl-containing polyacrylate (DFPA), dodecafluoroheptyl methacrylate (DFMA)-*co*-butyl acrylate (BA)-*co*-dimethylaminoethyl methacrylate (DM)-*co*-2-hydroxypropyl acrylate (HPA), and nanosilica	Cotton fabric	93

Robust amphiphobic coatings from bi-functional silica particles on flat substrates	Polymers were grafted onto silica (Stöber process) via sol –gel reactions. Epoxy resin was coated on the glass slide. Silica grafted with polymers was sprayed on the glass slide and cured. Long preparation times.	WCA > 160°	Silica TEM diameter (415 ± 15 nm)	Epoxy resin, silica co-grafted poly[3-(triisopropyloxysilyl)propyl methacrylate]-*block*-poly(2-perfluorooctylethyl methacrylate) (PIP-SMA-*b*-PFOEMA or P1), and poly[3-(triisopropyloxysilyl)propyl methacrylate]-*block*-poly(*tert*-butyl acrylate) (PIPSMA-*b*-PtBA or P2)	Glass plate	94
Fabrication of superhydrophobic surfaces using structured colloids	"Aqueous dispersions of silica aggregates were placed onto glass substrate and water was evaporated at room temperature."	WCA > 150° Max. reported 154.2°	Silica size (modified Stöber process) – 250, 410, and 520 nm Seeded growth method – 750 nm.	Silica nanospheres, (heptadecafluoro-1,1,2,2,-tetrahydrodecyl) triethoxysilane, hexadecane, and hypermer 2296 (emulsion stabilizer)	Glass	95
Direct breath figure formation on PMMA and superhydrophobic surface using *in situ* perfluoro-modified silica nanoparticles	PMMA was roughened using direct breath figure formation (DBF) method *In situ* hydrophobic silica was synthesized using hydrophobic silane, TEOS, ethanol, water and ammonia and dip coated on rough PMMA to prepare superhydrophobic surface. The *in situ* synthesis took 24 h.	Sessile WCA - 175°	Silica - 18 – 600 nm	1H,1H,2H,2H-perflurooctyltriethoxysilane (perfluoro silane) tetraethoxysilane, methanol, ethanol, THF, and ammonia.	PMMA	96
Highly monodisperse polysilsesquioxane spheres: Synthesis	Polysilsesquioxane (silica spheres) were synthesized using MTMS+SDBS+PVP followed by	WCA Methyl-spheres -155°	Average diameters:	Methyltrimethoxysilane (MTMS), vinyltrimethoxysilane (VTMS), 3-	Cotton fabric	97

and application in cotton fabrics	addition of TEA. The vinyl and thiol spheres were synthesized using VTMS and MPTMS. Finally, the cotton fabrics to be coated were dipped in the above silica spheres along with a cross-linker to prepare a SHS. Preparation time was long.	Vinyl-spheres -150° Thiol-spheres -125°	Methyl spheres – 1.1µm Vinyl spheres – 1.5µm Thiol-spheres- 1.9µm	mercaptopropyltrimethoxysilane (MPTMS), Triethylamine (TEA), sodium dodecyl benzene sulfonate (SDBS), polyvinylpyrrolidone (PVP), and AF3600		
Triple-scale structured superhydrophobic and highly oleophobic surfaces	"Superhydrophobic films via a layer-by-layer particle deposition approach: large silica particles (1.2 µm in diameter) were first partially embedded in an epoxy matrix, followed by electrostatic deposition of medium (180 nm) and small (20 nm) particles."	WCA (10 µL) ~ 167° Roll-off angle (10 µL) - 1° WCA (1 µL) ~ 171° Roll-off angle (1 µL) - 1°	Large silica particles (1.2 µm), medium (180 nm), and small (20 nm)	Tetraethylorthosilicate (TEOS), 3-aminopropyl triethoxysiloxane (APS), 3-glycidoxypropyl trimethoxysilane (GPS), silicon tetrachloride (SiCl4) , 1H,1H,2H,2H-perfluorodecyl trichlorosilane (Rf-Si), and epoxy resin materials	Silicon	98
Deforming water droplets with a superhydrophobic silica coating	"Sol containing nano-sized silica particles was prepared firstly by means of the Stöber process and was then doped with excess hexamethyldisilazane (HMDS), which gave rise to a gel coating with the surface covered by a high ratio of −CH3 groups."	WCA - 156°	Silica particles - 20 nm in diameter	Silica particles prepared by the Stöber process and hexamethyldisilazane (HDMS)	Glass slides and tubes	75
Facile fabrication of superhydrophobic raspberry-like	"Vinyl-functionalized silica (vinyl-SiO2) particles were prepared via a one-step sol–gel process using vinyltriethoxysilane as the precursor. Nanosized polystyrene particles were	WCA – 157.4°	Vinyl silica - 500 nm	Vinyltriethoxysilane (VTES), sodium dodecyl benzene sulfonate (SDBS), ammonium	Glass slides	99

SiO_2/polystyrene composite particles	then adsorbed onto the vinyl-SiO_2 particles to form raspberry-like composite particles by emulsion polymerization."			persulfate (APS), styrene (St), ethanol, and deionized water		
Effect of thermal treatment on hydrophobicity of methyl-functionalised hybrid nano-silica particles	"Methyl silica particles with superhydrophobic nature were prepared by sol–gel hydrolysis from methyltrimethoxysilane with tetraethyl orthosilicate."	WCA - 124°	Synthesized particle size - 140 nm (reduced to 90 nm on heating)	Methyltrimethoxysilane, ammonium hydroxide, tetraethyl orthosilicate, and double distilled water	Glass tube	[78]
Template synthesis of raspberry-like polystyrene/SiO2 composite microspheres and their application in wettability gradient surfaces	Firstly, carboxyl functionalized polystyrene (PS) template particles were prepared using acrylic acid, styrene, water, and KPS via emulsion polymerization. Then composite spheres of SiO_2/PS were prepared via sol-gel processing of TEOS with ammonia on carboxyl functionalized PS template particles dispersed in dehydrated ethanol. Preparation time was long upto 24 h.	WCA > 110°		Styrene (St), acrylic acid, potassium persulfate (KPS) initiator, tetraethoxysilane (TEOS), dehydrated ethanol and aqueous ammonia		[100]
Bulk synthesis of ordered macroporous silica particles for superhydrophobic coatings	"Large polystyrene (PS) beads and small silica nanoparticles were assembled simultaneously inside an emulsion, which formed composite structured particles during the evaporation of droplets. Then, by burning out PS beads, macroporous ceramic particle films were produced on substrate." The macroporous	WCA - 166.7°	Polystyrene beads - 800 nm Silica - 20 nm	Styrene monomer, potassium persulfate (initiator), sodium chloride, divinylbenzene (cross-linker), tetraethylorthosilicate (TEOS), octadecyltrimethoxysilane (OTMOS), ammonium hydroxide, and ethanol	Glass	[101]

	surface was coated with a flourinated molecule.					
A facile method to fabricate superhydrophobic cotton fabrics	"The superhydrophobic cotton fabric surface was synthesized by layer-by-layer self-assembly deposition of cationic poly(dimethyldiallylammonium chloride) and negative charged silica particles, followed with the modification of (heptadecafluoro-1,1,2,2-tetradecyl)trimethoxysilane reagent."	WCA – 155 ± 2°	Average diameter of silica particles - 266.7 nm	Tetraethyl orthosilicate (TEOS), ammonium hydroxide (NH_4OH), ethanol, aqueous solution of poly (dimethyldiallylammonium chloride) (poly-DMDAAC), and (heptadecafluoro-1,1,2,2-tetradecyl) trimethoxysilane	Cotton fabric	[102]
Enrichment in hydrophobicity and scratch resistant properties of silica films on glass by grafted microporosity of the network	"Sol-gel process using spin coating method from an alcoholic solution containing silica precursors; (methyltrimethoxysilane (MTMS), methanol (MeOH), ammonium fluoride (NH_4F), and polyvinyl alcohol (PVA))." This was followed by a spin coating on glass substrates followed by annealing.	WCA (10 µl) - 169 ± 1° Sliding angle - 5 ± 1°	Silica < 10 nm	Methyltrimethoxysilane (MTMS), methanol (MeOH), ammonium fluoride (NH_4F), and polyvinyl alcohol (PVA).	Glass	[103]
Superhydrophobic SiO_2 micro-particle coatings by spray method	"The superhydrophobic coatings were prepared using sol–gel derived SiO_2 micro-particles by spray method. A methyltrimethoxysilane (MTMS) was used as a sol–gel precursor to prepare a coating sol."	Static WCA - 162 ± 2° Roll-off angle - 6 ± 1°	SiO_2 particles were between 8 and 14 µm in diameter	Methyltrimethoxysilane (MTMS), methanol, and ammonium hydroxide	Glass	[77]

Investigation of the effect of dual-size coatings on the hydrophobicity of cotton surface	Layer-by-layer deposition of epoxy and amino functionalized silica particles of different sizes.	WCA < 150º (when lower size silica was the bottom layer)	Silica – 7, 12, 20, 40 nm	Epichlorohydrin, toluene, sodium hydroxide, methanol, Triton surfactant, citric acid, oleic acid, ethanol, 3-aminopropyltriethoxysiloxane (APTES), and 3-glycidoxypropyltrimethoxysilane (GPTMS)	Cotton	104
Electrochemical and mechanical properties of superhydrophobic aluminum substrates modified with nano-silica and fluorosilane	“Nano-silica particles were deposited on acid-etched hydrophilic aluminum (Al) substrates by immersion in well-dispersed nano-silica aqueous suspension and tetramethylammonium hydroxide, followed by a heat treatment. The surface was then further treated by a reaction with fluorosilane.”	WCA – 155° to 158°	Silica – 45 ± 5 nm	Silica slurry, tetramethylammonium hydroxide (TMAH), sulfuric acid, hydrogen peroxide, hydrofluoric acid, chloroform, hexadecane, and 1H,1H,2H,2H perfluorodecyltrichlorosilane (FDTS)	Aluminum	105
Facile preparation of superhydrophobic polymer surfaces	“In the first step a thin film of the desired polymer was coated onto the glass slide. This was followed by spin-coating of two layers of hydrophobic fumed silica using a dispersion in tetrahydrofuran. Finally to obtain a durable surface, a very thin film of the parent polymer was spin-coated from a very dilute solution containing 2.5% by weight hydrophobic silica and 0.25% by weight matrix polymer in tetrahydrofuran.”	Static WCA (10 µL) after 3 layers of hydrophobic silica + thin layer of polymer PS - 173.7 ± 0.5° PMMA – 172.9 ± 1.2° TPU - 170.8 ± 1.7° PC - 164.6 ± 1.9° TPSU- 172.6 ± 1.2° Epoxy- 174.8 ± 0.7°	Hydrophobic silica - 5 to 30 nm	Polydimethylsiloxane–urea copolymer (TPSU), a polyether based polyurethaneurea (TPU), poly(methyl methacrylate) (PMMA), polystyrene (PS), polycarbonate (PC) and a crosslinked epoxy resin (EPOXY), tetrahydrofuran (THF), hydrophobic silica, toluene, isopropyl alcohol, methylene chloride	Glass	106

		Hysteresis < 3° for all samples				
Robust superhydrophobic surfaces prepared with epoxy resin and silica nanoparticles	A mixture of bisphenol A based epoxy and silica particles was coated on a glass slide. The coated slides were oxygen plasma etched to increase their roughness followed by surface fluorination with perfluorooctyl trichlorosilane (PFOS).	WCA -169.2 ± 1.1°	Silica – 100 nm	Bisphenol A diglycidyl ether (EPON 828), hexahydro-4-methylphthalic anhydride, imidazole, and perfluorooctyl trichlorosilane (PFOS)	Glass	107
Effect of surface metrology on the wettability of SiO2 nanoparticle coating	SiO_2 nanoparticles of different sizes (7, 12, 14 and 40 nm) mixed with (heptadecafluoro-1,1,2,2-tetra-hydrodecyl) trichlorosilane were layer-by-layer spin-coated on glass.	WCA (5 μL) 7 nm + 40 nm – 156 ± 2° 12 nm + 40 nm –148 ± 2°	Silica - 7, 12, 14 and 40 nm	Aerosil OX 50 (40 nm), 150 (14 nm), 200 (12 nm), 380 (7 nm), and (heptadecafluoro-1,1,2,2-tetra-hydrodecyl) trichlorosilane (HDTC)	Glass	108
Superhydrophobic nanofiber membranes: effects of particulate coating on hydrophobicity and surface properties	"Electrospun polyacrylonitrile (PAN) nanofibers were dip-coated in as-synthesised silica nanoparticle-based coating solution at 10, 20, 30, 40, 50 min and 1 h after mixing" followed by treatment with a fluorinated silane. The treated fibers were then cured at 110 °C for 1 h.	WCA > 155° Sliding angle < 20° with 35 % silica particles loading	"After 10 min of hydrolysis, the average particle size was about 80 nm, and the size increased to around 170 nm after one hour of reaction. In the second half hour, the average particle size increased by only	Polyacrylonitrile (PAN; Mw 86,200 g/ml), tetraethylorthosilicate (TEOS), tridecafluorooctyltriethoxysilane (FAS), ethanol, dimethyl formamide, and ammonia solution in water.	PAN fibers	109

			28 nm (from 146 to 174 nm)."			
Do self-cleaning surfaces repel ice?	Substrates were dip coated with a two-layered coating: the outer layer with a flourinated polyhedral oligomeric sesquioxane (FPOSS) compound and the inner layer with a hydrophilic fumed silica.	Sessile WCA (5 µL) (i) 1 wt % silica + 3 wt % FPOSS2 - WCA >165° (ii) 0.5 wt % silica + 1.5 wt % FPOSS2 - WCA >165° Hysteresis > 1° for both procedures	Fumed silica - Aerosil 200 (did not mention the size)	Trifluoro cyclopentyl POSS ($C_{50}H_{93}F_{39}O_{12}Si_{10}$), fluoro disilanol isobutyl POSS ($C_{38}H_{75}F_{13}O_{12}Si_{8}$), and fumed silica	Polycarbonate	110
Superhydrophobic cotton fabrics prepared by one-step water-based sol–gel coating	"modified silica hydrosols were prepared by water-based sol–gel method, using methyl trimethoxy silane and hexadecyltrimethoxysilane as precursors, in the presence of the base catalyst and surfactant. The modified silica hydrosols were coated onto the cotton fabrics to achieve superhydrophobic surfaces by one-step process."	WCA (5 µL) - 151.9° Water shedding angle (15 µL) of 13°		Sodium dodecyl benzenesulfonate, ammonium hydroxide, methyl trimethoxy silane, and hexadecyltrimethoxysilane	Cotton fabric	111
Preparation of superhydrophobic silica nanoparticles by microwave assisted sol–gel process	Hydrophobic silica was synthesized using tetraethyl orthosilicate and hexadecyl trimethoxysilane with microwave assisted irradiation.	Sessile WCA ~ 142° to 154° (all experiments) Hysteresis < 12° (all experiments)	Silica – 25, 50, and 150 nm	Tetraethyl orthosilicate, hexadecyltrimethoxysilane, ammonia, ethanol, and deionized water	Glass	112

Preparation of superhydrophobic surface with a novel sol–gel system	“Sol–gel made from hydrolysis and condensation of the by-product of polymethylhydrosiloxane (PMHS) reacting with γ-aminopropyltriethoxysilane (KH550) was sprayed on glass slides.”	Mass ratio of KH550/PMHS - 0.25 WCA (8μL) - 157 ± 2° Water shedding angle (10μL) < 1°	Two tier topography after reaction with 200 nm and 2 μm sizes	Polymethylhydrosiloxane, γ-aminopropyltriethoxysilane, dibutyltin dilaurate, ammonia water, and ethanol	Microscope slides	[113]
Superamphiphobic diblock copolymer coatings	Diblock copolymer, poly[3-(triisopropyloxysilyl)propyl methacrylate]-block-poly[2-(perfluorooctyl)ethyl methacrylate] (P1 or PIPSMA-b-PFOEMA) consisting of a fluorinated PFOEMA block was grafted onto the synthesized silica nanoparticles. Coverslips were coated by casting and evaporating drops of the silica solution onto the slips. Printing paper (Lyreco)was immersed into a P1-coated silica solution for 5 s.	On glass: Static WCA - 167 ± 2° Hysteresis~ 7° Diiodmethane CA Static CA- 157 ± 2° Hysteresis ~ 10° HexadecaneCA Static CA- 149 ± 2° Hysteresis ~ 13° On paper: Static WCA -160 ± 2°	Silica synthesized by Stöber process TEM diameter – 325 ± 10 nm	Tetrahydrofuran (THF), benzophenone, hydrochloric acid, potassium, monomer IPSMA ([3-(triisopropyloxysilyl)propyl methacrylate]), monomer FOEMA ([2-(perfluorooctyl)ethyl methacrylate]), *sec*-butyl lithium, diphenyl ethylene, tetraethoxysilane, lithium chloride, α,α,α-trifluorotoluene (TFT), ammonia, and isopropanol	Glass microscope slides and printing paper	[114]

		Static cooking oil – 153 ± 2°				
Superhydrophobic sol–gel nanocomposite coatings with enhanced hardness	“embedding fumed silica nanoparticles in a partially condensed hybrid sol of methyltriethoxysilane (MTEOS) and colloidal silica. Fumed silica particles of size 25–30 nm were incorporated in the sol and the mixture was spray-coated on glass substrate.”	Coatings with 16.58 wt. % silica exhibited static WCA (8 μL) as high as 162.5°	Fumed silica – 25-30 nm Colloidal silica – 12 nm	Colloidal silica [LUDOX® LS, solid contents 30 wt%, aqueous dispersion, particle size 12 nm, pH 8.2], ethanol, and fumed nanosilica (CAB-O-SIL M5)	Glass slides	115
Synthesis of monodisperse fluorinated Silica nanoparticles and their superhydrophobic thin films	“silica nanoparticles with varying sizes were prepared in the laboratory using standard Stöber process and further functionalized with fluoroalkylsilane (FAS17) in an ethanolic solution to obtain fluorinated silica nanoparticles. These fluorinated silica nanoparticles dispersed solutions were spin-coated on aluminum alloy substrates to obtain superhydrophobic thin films.”	WCA using different diameters of silica (a) WCA with 119 ± 12 nm fluorinated silica - 151 ± 4° (b) WCA with 169 ± 8 nm fluorinated silica - 162 ± 6° (c) WCA with 300 ± 7 nm fluorinated silica - 165 ± 5°	Diameters of fluorinated silica nanoparticles synthesized by Stöber process were 119 ± 12 nm, 169 ± 8 nm, and 300 ± 7 nm nm	Fluoroalkylsilane or FAS17 ($C_{16}H_{19}F_{17}O_3Si$), ethanol, tetraethoxysilane, and ammonium hydroxide	AA-6061 aluminum alloy and silicon	116
Fabrication of mechanically robust superhydrophobic surfaces based on silica micro-nanoparticles and polydimethylsiloxane	Stöber process synthesized 100 nm silica spheres. The 100 nm spheres were modified by growing an octadecyltrichlorosilane (OTS) monolayer on them. Commercially bought 500 nm SiO_2 was used in conjunction with the modified 100 nm silica spheres for the	Sessile WCA of 155 ± 2° Sliding angle of ~ 6°	Diameter of silica spheres (Stober process) was 100 ± 10 nm Silica particles received – 500 nm	Octadecyltrichlorosilane, PDMS, ethanol, silica particles, hexane, and curing agent	Glass	74

	synthesis of the superhydrophobic surface. “Droplets of 500 nm M-SiO_2 mixture in ethanol were first applied on slightly inclined glass substrates, followed by drying at 100 °C for 3 min, and then droplets of 100 nm M-SiO_2 mixture were applied. The fine structure was then generated using the same coating approach for three cycles, and then covered with a layer of PDMS. Samples were finally dried and sintered at 60–140 °C for 24 h.”					
Fabrication of superhydrophobic silica film by removing polystyrene spheres	Co-sedimentation of two different sized polystyrene (PS) spheres followed by 3 times impregnation of silica in the voids between the PS spheres using acidic silica sol. Then, PS was removed by heating to yield silica films which were further modified with dodecafluoroheptyl-methyl-dimethoxysilane (DFMS) to give a SHS.	Static WCA (5µL) - 156.4°	PS spheres with diameters of 1.0–2.2 µm and 180 nm	PS spheres, tetraethyl orthosilicate, ethanol, hydrochloric acid, dodecafluoroheptyl-methyl-dimethoxysilane (DFMS), and deionized water	Glass slides	117
Superhydrophobic and anti-icing coating and method for making same	Silica nanoparticles with a primary size of about 50 nm attached to a micrometer-sized silica particle (purchased from Sigma-Aldrich) were made via the Stöber reaction. Both the synthesized silica nanoparticles and the micrometer-sized particles that they are attached to were functionalized with	Static WCA >160°	Silica nanoparticles around 50 nm Silica particles purchased -1 µm	Tetraethyl orthosilicate, ethanol, tridecafluoro- 1,1,2,2, -tetrahydrooctyl) trichlorosilane, acetone, DC3000, and DCH3070 (both commercial products).	Aluminum	118

	(tridecafluoro- 1,1,2,2, -tetrahydrooctyl) trichlorosilane. “The coating is made by mixing the components contemporaneously in any order at room temperature at the following weight percentages: DC3000 (20-40%), DCH3070 (7- 12%), silica or Fe_2O_3 particles (2- 10%), the fluorinated surfactant (0. 1-2%), and acetone (40-60%). The coating cures at room temperature in approximately 12 hours.”					
Nanotextured surfaces	Polymers such as polycaprolactone, polybutyl methacylate, polystyrene, and polyisobutylene were mixed with triazine crosslinker and hydrophobic silica to prepare superhydrophobic coatings. The coating composition was sprayed onto the surface followed by irradiation with UV light.	Static WCA > 150°	Cab-O-Sil® TS-720 silica nanoparticles	Polymers such as polycaprolactone, polybutyl methacylate, polystyrene, and polyisobutylene, triazine crosslinker, and CAB-0-SM® TS-720 silica nanoparticles	LNB surface	84
Nanotextured super or ultra hydrophobic coatings	Polymers such as polycaprolactone, nylon 6, 6, polystyrene, and polyisobutylene were mixed with a cross linker and hydrophobic silica to prepare superhydrophobic coatings. The coating composition was sprayed onto different surfaces followed by irradiation with UV light.	Sliding angle > 10°	CAB-O-SIL TS-720 silica nanoparticles	Different polymers such as polycaprolactone, nylon 6,6, polystyrene, and polyisobutylene, CAB-0-SIL TS-720 silica nanoparticles, UV cross-linker, and tetrahydrofuran	N-octyltrimethoxysilane treated glass, aluminum, high density polyethylene, and low density polyethylene slides	83

1.4 Nitrilotris(methylene)triphosphonic acid and Zr(IV) Layer- By-Layer Assembly

1.4.1 Self-Assembled Monolayers

Self-assembled monolayers (SAMs) have numerous applications, including for surface passivation,[119] biological sensors,[119-121] electronic devices,[119-120, 122] and lubrication.[119, 123] Some of the most studied SAM components include the silanes, which effectively bind to silica surfaces,[124-125] the alkanethiols, which form monolayers on gold,[121, 126-127] alkanes and alkenes, which bind to hydrogen-terminated and scribed (bare) silicon,[80, 82, 128-130] and the phosphonic acids (PAs), which adhere well to metal oxides,[127] including alumina,[121, 127, 131-137] iron oxide,[136, 138] tantalum oxide,[126, 137] silicon oxide,[139-140] copper oxide,[136] titania,[137, 139, 141-143] zirconia,[137, 139] niobium oxide,[137] and indium tin oxide.[144] Phosphonates form the most densely packed monolayers on aluminum reported.[135] In addition, they have different affinities for different metals and metal oxides – depending on the substrate, the binding of a phosphonate can be monodentate, bidendate or tridendate.[138, 144]

1.4.2 Layer-By-Layer (LBL) Assembly of Phosphonates

In general, LBL assemblies are prepared as follows. First, a solid planar substrate is used that has positive or negative surface charges. To this end, silicon substrates are commonly employed because of their silanol groups – they are negatively charged at neutral pH values. The general procedure for the formation of multilayer assemblies on silicon then involves immersion of the planar silicon in a solution of a polycation, which leads to adsorption of the polycation on the surface. This adsorption flips the surface charge. The surface with the polycation layer is then immersed in a solution of a polyanion, which results in deposition of this material, again due to electrostatic interactions. The process is repeated multiple times to obtain the desired number of layers.[145-146]

In 1987, Mallouk and co-workers[146-147] demonstrated a sequential LBL deposition of a biphosphonic acid with a long hydrocarbon chain on zirconium on silicon and gold. The thickness increase after deposition of a single bilayer (the bisphosphonate followed by zirconium) was 17 Å.[146-147] Subsequently, a series of studies have reported the LBL preparation of multi-layer films from various long chain phosphonates and zirconium.[148-149] All of these SAM systems have been extensively studied using multiple characterization techniques.

1.4.3 Nitrilotris(methylene)triphosphonic Acid and its Applications

Amino phosphonates have been employed for years in various industries as corrosion inhibitors,[131] where nitrilotris(methylene)triphosphonic acid (NTMP) (see Figure 1.1) is an important example of one of these species. In particular, NTMP has been used as a corrosion inhibitor in water plants,[132, 150] to prevent staining of painted or treated wood surfaces by tannins,[151] to improve the durability of adhesively bonded aluminum structures,[134] and as a cement hydration inhibitor.[152] It has also limited the corrosion of alumina/aluminum optical devices without affecting the optical properties of these devices.[133] The efficacy of NTMP can be attributed to the presence of three phosphonic acid groups that may attach to the target substrate. It has been proposed that phosphonic acids chemisorb on the surface of alumina, undergo condensation reactions with hydroxyl groups on it, and form P-O-Al bonds.[131]

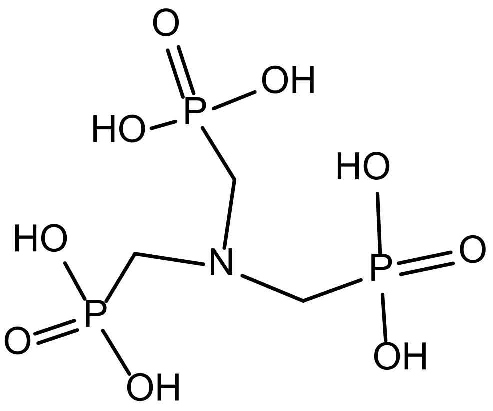

Figure 1.1 Structure of nitrilotris(methylene)triphosphonic acid (NTMP)

Preparation of LBL[153-156] films of NTMP and zirconium at two different temperatures (room temperature and 70 °C) on e-beam deposited alumina (ca. 22 nm) on Si/SiO_2 substrates[157-158] is described in chapter 4. The films are characterized after deposition of each layer by a suite of techniques,[5, 159] including ellipsometry, X-ray photoelectron spectroscopy (XPS), time-of-flight secondary ion mass spectrometry (ToF-SIMS) and atomic force microscopy (AFM). This work is important for two reasons. First, the preparation of very thin films from a corrosion inhibitor and Zr(IV) has been demonstrated. By spectroscopic ellipsometry (SE) the films are 1.7 nm thick after deposition of 4.5 bilayers of NTMP and Zr(IV) (5 NTMP + 4 Zr layers). The thinness of these films will be advantageous for optical devices that may suffer in performance if coated with thicker layers. The multi-instrument characterization of this work is also significant. First, the alumina films were characterized by SE. The resulting dispersion relationship for n(λ) follows a simple Cauchy model and reveals that the films are under dense. The Cauchy dispersion relation is given as:[160]

$$n(\lambda) = A + \frac{B}{\lambda^2} + \frac{C}{\lambda^4} \tag{1.10}$$

where A, B, and C are empirical fit coefficients and λ is the wavelength. The extinction coefficient (k) should be 0 for the Cauchy model to be applicable, i.e., the material is transparent. This model provides a good approximation of the thickness of this film and its refractive index over a rather wide wavelength range.[160] However, the Cauchy model breaks down in the limits of very long and very short λ. For very short λ it predicts that n → ∞, which is unphysical, while for very long λ it predicts that n approaches a constant value, i.e., 'A' in the model, which is also not true for materials. For this study, a wavelength range of 300-1000 nm is used to allow proper application of the Cauchy model. A series of careful SE measurements then show a steady increase in film thickness with film growth/LBL deposition. XPS shows the expected decrease in substrate signal with film growth and concomitant increases in signals from P, N, and Zr, where these signals depend subtly on the LBL deposition. In ToF-SIMS, a pulsed primary ion beam is directed towards a surface, which leads to secondary emission of neutrals, electrons, and charged secondary ions. Unfortunately, most of the secondary species produced in this process are neutral and cannot be directly analyzed by mass spectrometry. The charged ions are extracted to the detector using a bias of a few thousand volts. These charged species are analyzed on the basis of their masses, revealing information about the chemical composition of the surface.[161] Various projectiles are available to be used as primary ion beams, including Ga^+, Cs^+, Bi^+ and its clusters, Ar^+, C_{60}^+, etc. For this study, Cs^+ was employed as the primary ion beam as it provides enhancement in the yield of the electronegative ions.[161] In my work, time-of-flight secondary ion mass spectrometry with a Cs^+ primary ion source shows a decrease in substrate signal (Al^+) and increase in neighboring hydrocarbon signal ($C_2H_3^+$) with increasing film growth, where both ions have the same nominal mass. ToF-SIMS also shows the appearance of the expected PO^-, PO_2^-, PO_3^-, and CN^- signals with NTMP deposition, and reveals some nitrogen contamination in the substrate. Atomic force microscopy shows that all depositions result in extremely smooth films. XPS and ToF-SIMS further show the corrosive nature of the Zr(IV) solution on the alumina substrate at 70 °C.

1.5 References

1. Burakowski, T.; Wierzchon, T., *Surface engineering of metals: principles, equipment, technologies*. CRC press: 1998.

2. Oshida, Y., *Surface Engineering and Technology for Biomedical Implants*; Momentum Press: New York, 2014.

3. Vladkova, T. G., *Surface Engineering of Polymeric Biomaterials*; Smithers Rapra: Shrewsbury, 2013.

4. Takadoum, J., Characterization of Coatings. In *Nanomaterials and Surface Engineering*; John Wiley & Sons, Inc.: 2013; pp 293-328.

5. Jensen, D. S.; Kanyal, S. S.; Madaan, N.; Hancock, J. M.; Dadson, A. E.; Vail, M. A.; Vanfleet, R.; Shutthanandan, V.; Zhu, Z.; Engelhard, M. H. *Surf. Interface Anal.* **2013,** *45* (8), 1273-1282.

6. Prosen, H.; Zupančič-Kralj, L. *Trends Anal. Chem.* **1999,** *18* (4), 272-282.

7. Pawliszyn, J., 1 - Solid-Phase Microextraction in Perspective. In *Handbook of Solid Phase Microextraction*; Elsevier: Oxford, 2012; pp 1-12.

8. Mehdinia, A.; Aziz-Zanjani, M. O. *Trends Anal. Chem.* **2013**, 42, 205-215.

9. Xu, J.; Zheng, J.; Tian, J.; Zhu, F.; Zeng, F.; Su, C.; Ouyang, G. *Trends Anal. Chem.* **2013**, 47, 68-83.

10. Bruheim, I.; Liu, X.; Pawliszyn, J. *Anal. Chem.* **2003,** *75* (4), 1002-1010.

11. Jiang, R.; Pawliszyn, J. *Trends Anal. Chem.* **2012,** *39* (0), 245-253.

12. Bojko, B.; Cudjoe, E.; Pawliszyn, J.; Wasowicz, M. *Trends Anal. Chem.* **2011,** *30* (9), 1505-1512.

13. Pawliszyn, J. *J. Chromatogr. Sci.* **2000,** *38* (7), 270-278.

14. Górecki, T.; Yu, X.; Pawliszyn, J. *Analyst* **1999,** *124* (5), 643-649.

15. Pawliszyn, J., 2 - Theory of Solid-Phase Microextraction. In *Handbook of Solid Phase Microextraction*; Elsevier: Oxford, 2012; pp 13-59.

16. Zhang, Z.; Pawliszyn, J. *Anal. Chem.* **1993,** *65* (14), 1843-1852.

17. Cho, H.-J.; Baek, K.; Lee, H.-H.; Lee, S.-H.; Yang, J.-W. *J. Chromatogr. A* **2003,** *988* (2), 177-184.

18. Koziel, J.; Jia, M.; Pawliszyn, J. *Anal. Chem.* **2000,** *72* (21), 5178-5186.

19. Rahimi, A.; Hashemi, P.; Badiei, A.; Arab, P.; Ghiasvand, A. R. *Anal. Chim. Acta* **2011,** *695* (1), 58-62.

20. Li, X.; Li, C.; Chen, J.; Li, C.; Sun, C. *J. Chromatogr. A* **2008,** *1198*, 7-13.

21. Liu, H.; Ji, L.; Li, J.; Liu, S.; Liu, X.; Jiang, S. *J. Chromatogr. A* **2011,** *1218* (20), 2835-2840.

22. Du, X.-Z.; Wang, Y.-R.; Tao, X.-J.; Deng, H.-L. *Anal. Chim. Acta* **2005,** *543* (1), 9-16.

23. Zhang, S.; Du, Z.; Li, G. *Anal. Chem.* **2011,** *83* (19), 7531-7541.

24. Hashemi, P.; Shamizadeh, M.; Badiei, A.; Poor, P. Z.; Ghiasvand, A. R.; Yarahmadi, A. *Anal. Chim. Acta* **2009,** *646* (1), 1-5.

25. Hashemi, P.; Shamizadeh, M.; Badiei, A.; Ghiasvand, A. R.; Azizi, K. *Chromatographia* **2009,** *70* (7-8), 1147-1151.

26. Ji, J.; Liu, H.; Chen, J.; Zeng, J.; Huang, J.; Gao, L.; Wang, Y.; Chen, X. *J. Chromatogr. A* **2012,** *1246*, 22-27.

27. Mehdinia, A.; Mousavi, M. F.; Shamsipur, M. *J. Chromatogr. A* **2006,** *1134* (1), 24-31.

28. Feng, J.; Sun, M.; Liu, H.; Li, J.; Liu, X.; Jiang, S. *J. Chromatogr. A* **2010,** *1217* (52), 8079-8086.

29. Alizadeh, R.; Najafi, N. M.; Kharrazi, S. *Anal. Chim. Acta* **2011,** *689* (1), 117-121.

30. Hafez, A. M.; Wenclawiak, B. W. *Anal. Bioanal. Chem.* **2013,** *405* (5), 1753-1758.

31. Budziak, D.; Martendal, E.; Carasek, E. *Anal. Chim. Acta* **2007,** *598* (2), 254-260.

32. Liu, Y.; Shen, Y.; Lee, M. L. *Anal. Chem.* **1997,** *69* (2), 190-195.

33. Anbia, M.; Khazaei, M. *Chromatographia* **2011,** *73* (3-4), 379-384.

34. Zhang, Z.; Wang, Q.; Li, G. *Anal. Chim. Acta* **2012,** *727*, 13-19.

35. Hou, J.-g.; Ma, Q.; Du, X.-z.; Deng, H.-l.; Gao, J.-z. *Talanta* **2004,** *62* (2), 241-246.

36. Ji, L.; Li, H. X.; Zhao, F.; Chen, J. M.; Zhou, H. D. *Key Eng. Mater.* **2003,** *373-374*, 151-154.

37. Rossnagel, S. M. *IBM J. Res. Dev.* **1999,** *43* (1.2), 163-179.

38. Wang, H.; Lunt, B. M.; Gates, R. J.; Asplund, M. C.; Shutthanandan, V.; Davis, R. C.; Linford, M. R. *ACS Appl. Mater. Interfaces* **2013,** *5* (17), 8407-8413.

39. Abbott, J.; Niederhauser, T. L.; Hansen, D. P.; Perkins, R. T.; Bell, D. A.; Bard, E. C.; Lunt, B. M.; Worthington, M. O.; Miller, C. M.; Hyatt, D. F. *ACS Appl. Mater. Interfaces* **2010,** *2* (8), 2373-2376.

40. Wang, H.; Madaan, N.; Bagley, J.; Diwan, A.; Liu, Y.; Davis, R. C.; Lunt, B. M.; Smith, S. J.; Linford, M. R. *Thin Solid Films* **2014,** *569*, 124-130.

41. Harris, K. D.; Brett, M. J.; Smy, T. J.; Backhouse, C. *J. Electrochem. Soc.* **2000,** *147* (5), 2002-2006.

42. Wu, A. T.; Brett, M. J. *Sensor Mater.* **2001,** *13* (7), 399-431.

43. Robbie, K.; Brett, M. J. *J. Vac. Sci. Technol. A* **1997,** *15* (3), 1460-1465.

44. Martin, P. M., *Handbook of Deposition Technologies for Films and Coatings*. Third ed.; 2009; p 936.

45. Smith, D. O.; Cohen, M. S.; Weiss, G. P. *J. Appl. Phys.* **1960,** *31* (10), 1755-1762.

46. Dick, B.; Brett, M. J.; Smy, T. *J. Vac. Sci. Technol. B* **2003,** *21* (1), 23-28.

47. Thornton, J. A. *J. Vac. Sci. Technol. A* **1986,** *4* (6), 3059-3065.

48. Ma, M.; Hill, R. M. *Curr. Opin. Colloid Interface Sci.* **2006,** *11* (4), 193-202.

49. Feng, L.; Li, S.; Li, Y.; Li, H.; Zhang, L.; Zhai, J.; Song, Y.; Liu, B.; Jiang, L.; Zhu, D. *Adv. Mater.* **2002,** *14* (24), 1857-1860.

50. Li, X.-M.; Reinhoudt, D.; Crego-Calama, M. *Chem. Soc. Rev.* **2007,** *36* (8), 1350-1368.

51. Zhang, X.; Shi, F.; Niu, J.; Jiang, Y.; Wang, Z. *J. Mater. Chem.* **2008,** *18* (6), 621-633.

52. Gao, L.; McCarthy, T. J. *Langmuir* **2006,** *22* (7), 2966-2967.

53. Barthlott, W.; Neinhuis, C. *Planta* **1997,** *202* (1), 1-8.

54. Roach, P.; Shirtcliffe, N. J.; Newton, M. I. *Soft Matter* **2007,** *4* (2), 224-240.

55. Wang, S.; Jiang, L. *Adv. Mater.* **2007,** *19* (21), 3423-3424.

56. Ling, X. Y.; Phang, I. Y.; Vancso, G. J.; Huskens, J.; Reinhoudt, D. N. *Langmuir* **2009,** *25* (5), 3260-3263.

57. Bravo, J.; Zhai, L.; Wu, Z.; Cohen, R. E.; Rubner, M. F. *Langmuir* **2007,** *23* (13), 7293-7298.

58. Soeno, T.; Inokuchi, K.; Shiratori, S. *Appl. Surf. Sci.* **2004,** *237* (1), 539-543.

59. Hsieh, C.-T.; Wu, F.-L.; Yang, S.-Y. *Surf. Coat. Technol.* **2008,** *202* (24), 6103-6108.

60. Xue, C.-H.; Jia, S.-T.; Zhang, J.; Tian, L.-Q. *Thin Solid Films* **2009,** *517* (16), 4593-4598.

61. Xiu, Y.; Zhu, L.; Hess, D. W.; Wong, C. *Langmuir* **2006,** *22* (23), 9676-9681.

62. Miwa, M.; Nakajima, A.; Fujishima, A.; Hashimoto, K.; Watanabe, T. *Langmuir* **2000,** *16* (13), 5754-5760.

63. Zhai, L.; Cebeci, F. C.; Cohen, R. E.; Rubner, M. F. *Nano Lett.* **2004,** *4* (7), 1349-1353.

64. Shang, H.; Wang, Y.; Limmer, S.; Chou, T.; Takahashi, K.; Cao, G. *Thin Solid Films* **2005,** *472* (1), 37-43.

65. Cassie, A.; Baxter, S. *Trans. Faraday Society* **1944,** *40*, 546-551.

66. Marmur, A. *Langmuir* **2003,** *19* (20), 8343-8348.

67. Roumeli, E.; Pavlidou, E.; Papadopoulou, E.; Vourlias, G.; Bikiaris, D.; Paraskevopoulos, K.; Chrissafis, K. *Thermochim. Acta* **2012**, 527, 33-39.

68. Lin, Q.; Yang, G.; Liu, J.; Rao, J. *Front. For. China* **2006,** *1* (2), 230-237.

69. Park, B. D.; Kang, E. C.; Park, J. Y. *J. Appl. Polym. Sci.* **2008,** *110* (3), 1573-1580.

70. Samaržija-Jovanović, S.; Jovanović, V.; Konstantinović, S.; Marković, G.; Marinović-Cincović, M. *J. Therm. Anal. Calorim.* **2011,** *104* (3), 1159-1166.

71. Chen, W.; Wei, T.-c. Superficially porous particles and methods of making and using same. US Patent 20,100,206,797, August 19, 2010.

72. Gu, G.; Dang, H.; Zhang, Z.; Wu, Z. *Appl. Phys. A* **2006,** *83* (1), 131-132.

73. Stöber, W.; Fink, A.; Bohn, E. *J. Colloid Interface Sci.* **1968,** *26* (1), 62-69.

74. Ke, Q.; Fu, W.; Jin, H.; Zhang, L.; Tang, T.; Zhang, J. *Surf. Coat. Technol.* **2011,** *205* (21–22), 4910-4914.

75. Li, X.; Shen, J. *Chem. Commun.* **2013,** *49* (85), 10016-10018.

76. Bae, G. Y.; Min, B. G.; Jeong, Y. G.; Lee, S. C.; Jang, J. H.; Koo, G. H. *J. Colloid Interface Sci.* **2009,** *337* (1), 170-175.

77. Latthe, S. S.; Rao, A. V. *Surf. Coat. Technol.* **2012,** *207* (0), 489-492.

78. Sutha, S.; Yuvakkumar, R.; Rajendran, V.; Palanivelu, R. *Mater. Lett.* **2013,** *90* (0), 68-71.

79. Yang, L.; Lua, Y.-Y.; Tan, M.; Scherman, O. A.; Grubbs, R. H.; Harb, J. N.; Davis, R. C.; Linford, M. R. *Chem. Mater.* **2007,** *19* (7), 1671-1678.

80. Lee, M. V.; Guo, D.; Linford, M. R.; Zuilhof, H. *Langmuir* **2004,** *20* (21), 9108-9113.

81. Yang, L.; Lua, Y.-Y.; Jiang, G.; Tyler, B. J.; Linford, M. R. *Anal. Chem.* **2005,** *77* (14), 4654-4661.

82. Shirahata, N.; Linford, M. R.; Furumi, S.; Pei, L.; Sakka, Y.; Gates, R. J.; Asplund, M. C. *Chem. Commun.* **2009,** (31), 4684-4686.

83. Lawin, L. R.; Guire, P.; Wen, J.; Taton, K. Nanotextured super or ultra hydrophobic coatings. US Patent 7,943,234: 2011.

84. Guire, P. E.; Taton, K.; Wen, J.; Lawin, L. R. Nanotextured surfaces. US Patent 20,110,268,973: 2011.

85. Gupta, V.; Madaan, N.; Jensen, D. S.; Kunzler, S. C.; Linford, M. R. *Langmuir* **2013,** *29* (11), 3604-3609.

86. Saini, G.; Sautter, K.; Hild, F. E.; Pauley, J.; Linford, M. R. *J. Vac. Sci. Technol. A* **2008,** *26* (5), 1224-1234.

87. Zhang, F.; Sautter, K.; Larsen, A. M.; Findley, D. A.; Davis, R. C.; Samha, H.; Linford, M. R. *Langmuir* **2010,** *26* (18), 14648-14654.

88. Balachander, N.; Sukenik, C. N. *Langmuir* **1990,** *6* (11), 1621-1627.

89. Husseini, G. A.; Peacock, J.; Sathyapalan, A.; Zilch, L. W.; Asplund, M. C.; Sevy, E. T.; Linford, M. R. *Langmuir* **2003,** *19* (12), 5169-5171.

90. Maoz, R.; Sagiv, J. *J. Colloid Interface Sci.* **1984,** *100* (2), 465-496.

91. Quan, Y.-Y.; Zhang, L.-Z. *Appl. Surf. Sci.* **2014,** *292* (0), 44-54.

92. Psarski, M.; Celichowski, G.; Marczak, J.; Gumowski, K.; Sobieraj, G. B. *Surf. Coat. Technol.* **2013,** *225* (0), 66-74.

93. An, Q.; Xu, W.; Hao, L.; Fu, Y.; Huang, L. *J. Appl. Polym. Sci.* **2013,** *128* (5), 3050-3056.

94. Xiong, D.; Liu, G.; Scott Duncan, E. J. *Polymer* **2013,** *54* (12), 3008-3016.

95. Cho, Y.-S.; Moon, J.; Lim, D.; Kim, Y. *Korean J. Chem. Eng.* **2013,** *30* (5), 1142-1152.

96. Farbod, F.; Pourabbas, B.; Sharif, M. *J. Polym. Sci., Part B: Polym. Phys.* **2013,** *51* (6), 441-451.

97. Ma, W.; Zhang, D.; Duan, Y.; Wang, H. *J. Colloid Interface Sci.* **2013,** *392* (0), 194-200.

98. Zhao, J.; Leng, B. B.; Shao, Z. Z.; With, d. G. B.; Ming, W. W. *RSC Adv.* **2013,** *3*, 22332 - 22339

99. Shang, Q.; Wang, M.; Liu, H.; Gao, L.; Xiao, G. *Polym. Compos.* **2013,** *34* (1), 51-57.

100. Fan, X.; Zheng, L.; Cheng, J.; Xu, S.; Wen, X.; Cai, Z.; Pi, P.; Yang, Z. *Surf. Coat. Technol.* **2012,** *213* (0), 90-97.

101. Cho, Y.-S.; Choi, S.-Y.; Kim, Y.-K.; Yi, G.-R. *J. Colloid Interface Sci.* **2012,** *386* (1), 88-98.

102. Zhang, M.; Wang, S.; Wang, C.; Li, J. *Appl. Surf. Sci.* **2012,** *261* (0), 561-566.

103. Kavale, M.; Mahadik, S. A.; Mahadik, D. B.; Parale, V. G.; Rao, A. V.; Vhatkar, R. S.; Wagh, P. B.; Gupta, S. C. *J. Sol-Gel Sci. Technol.* **2012,** *64* (1), 9-16.

104. Athauda, T.; Ozer, R. *Cellulose* **2012,** *19* (3), 1031-1040.

105. Shi, X.; Nguyen, T. A.; Suo, Z.; Wu, J.; Gong, J.; Avci, R. *Surf. Coat. Technol.* **2012,** *206* (17), 3700-3713.

106. Yilgor, I.; Bilgin, S.; Isik, M.; Yilgor, E. *Polymer* **2012,** *53* (6), 1180-1188.

107. Yonghao, X.; Yan, L.; Balu, B.; Hess, D. W.; Chingping, W. *IEEE Trans. Compon. Packag. Manuf. Technol.* **2012,** *2* (3), 395-401.

108. Athauda, T. J.; Decker, D. S.; Ozer, R. R. *Mater. Lett.* **2012,** *67* (1), 338-341.

109. Fang, J.; Wang, H.; Wang, X.; Lin, T. *J. Text. I.* **2011,** *103* (9), 937-944.

110. Dodiuk, H.; Kenig, S.; Dotan, A. *J. Adhes. Sci. Technol.* **2012,** *26* (4-5), 701-714.

111. Xu, L.; Zhuang, W.; Xu, B.; Cai, Z. *J. Text. I.* **2011,** *103* (3), 311-319.

112. Santiago, A.; González, A.; Iruin, J. J.; Fernández-Berridi, M. J.; Irusta, L. *J. Sol-Gel Sci. Technol.* **2012,** *61* (1), 8-13.

113. Su, D.; Huang, C.; Hu, Y.; Jiang, Q.; Zhang, L.; Zhu, Y. *Appl. Surf. Sci.* **2011,** *258* (2), 928-934.

114. Xiong, D.; Liu, G.; Hong, L.; Duncan, E. J. S. *Chem. Mater.* **2011,** *23* (19), 4357-4366.

115. Lakshmi, R. V.; Bharathidasan, T.; Basu, B. J. *Appl. Surf. Sci.* **2011,** *257* (24), 10421-10426.

116. Brassard, J.-D.; Sarkar, D. K.; Perron, J. *ACS Appl. Mater. Inter.* **2011,** *3* (9), 3583-3588.

117. Shang, Q.; Gao, L.; Liu, H.; Xiao, G. *J. Sol-Gel Sci. Technol.* **2011,** *59* (2), 334-337.

118. Gao, D., Superhydrophobic and anti-icing coating and method for making same. WO Patent 2,012,156,172, November 22, 2012.

119. Pellerite, M. J.; Dunbar, T. D.; Boardman, L. D.; Wood, E. J. *The Journal of Physical Chemistry B* **2003,** *107* (42), 11726-11736.

120. Dubey, M.; Gouzman, I.; Bernasek, S. L.; Schwartz, J. *Langmuir* **2006,** *22* (10), 4649-4653.

121. Attavar, S.; Diwekar, M.; Linford, M. R.; Davis, M. A.; Blair, S. *Appl. Surf. Sci.* **2010,** *256* (23), 7146-7150.

122. Gouzman, I.; Dubey, M.; Carolus, M. D.; Schwartz, J.; Bernasek, S. L. *Surf. Sci.* **2006,** *600* (4), 773-781.

123. Hoque, E.; Derose, J. A.; Hoffmann, P.; Mathieu, H. J.; Bhushan, B.; Cichomski, M. *J. Chem. Phys.* **2006,** *124* (17), 174710.

124. Sagiv, J. *J. Am. Chem. Soc.* **1980,** *102* (1), 92-98.

125. Wasserman, S. R.; Tao, Y. T.; Whitesides, G. M. *Langmuir* **1989,** *5* (4), 1074-1087.

126. Textor, M.; Ruiz, L.; Hofer, R.; Rossi, A.; Feldman, K.; Hähner, G.; Spencer, N. D. *Langmuir* **2000,** *16* (7), 3257-3271.

127. Hoque, E.; DeRose, J.; Hoffmann, P.; Bhushan, B.; Mathieu, H. *The Journal of Physical Chemistry C* **2007,** *111* (10), 3956-3962.

128. Linford, M. R.; Fenter, P.; Eisenberger, P. M.; Chidsey, C. E. *J. Am. Chem. Soc.* **1995,** *117* (11), 3145-3155.

129. Niederhauser, T. L.; Jiang, G.; Lua, Y.-Y.; Dorff, M. J.; Woolley, A. T.; Asplund, M. C.; Berges, D. A.; Linford, M. R. *Langmuir* **2001,** *17* (19), 5889-5900.

130. Cannon, B. R.; Lillian, T. D.; Magleby, S. P.; Howell, L. L.; Linford, M. R. *Precision engineering* **2005,** *29* (1), 86-94.

131. Ramsier, R.; Henriksen, P.; Gent, A. *Surf. Sci.* **1988,** *203* (1), 72-88.

132. Zanzucchi, P.; Thomas, J. *J. Electrochem. Soc.* **1988,** *135* (6), 1370-1376.

133. Lines, M.; Perkins, R. T., Corrosion resistant wire-grid polarizer and method of fabrication. US patent 20,030,227,678, December 11, 2003.

134. Venables, J. D.; Tadros, M. E.; Ditchek, B. M., Durability of adhesively bonded aluminum structures and method for inhibiting the conversion of aluminum oxide to aluminum hydroxide. US patent 4,308,079, December 29, 1981.

135. Liakos, I. L.; Newman, R. C.; McAlpine, E.; Alexander, M. R. *Surf. Interface Anal.* **2004,** *36* (4), 347-354.

136. Van Alsten, J. G. *Langmuir* **1999,** *15* (22), 7605-7614.

137. Hofer, R.; Textor, M.; Spencer, N. D. *Langmuir* **2001,** *17* (13), 4014-4020.

138. Raman, A.; Dubey, M.; Gouzman, I.; Gawalt, E. S. *Langmuir* **2006,** *22* (15), 6469-6472.

139. Gao, W.; Dickinson, L.; Grozinger, C.; Morin, F. G.; Reven, L. *Langmuir* **1996,** *12* (26), 6429-6435.

140. Fontes, G. N.; Malachias, A.; Magalhães-Paniago, R.; Neves, B. R. A. *Langmuir* **2003,** *19* (8), 3345-3349.

141. Guerrero, G.; Mutin, P.; Vioux, A. *Chem. Mater.* **2001,** *13* (11), 4367-4373.

142. Adden, N.; Gamble, L. J.; Castner, D. G.; Hoffmann, A.; Gross, G.; Menzel, H. *Langmuir* **2006,** *22* (19), 8197-8204.

143. Gawalt, E. S.; Avaltroni, M. J.; Koch, N.; Schwartz, J. *Langmuir* **2001,** *17* (19), 5736-5738.

144. Paramonov, P. B.; Paniagua, S. A.; Hotchkiss, P. J.; Jones, S. C.; Armstrong, N. R.; Marder, S. R.; Brédas, J.-L. *Chem. Mater.* **2008,** *20* (16), 5131-5133.

145. Lvov, Y.; Decher, G.; Sukhorukov, G. *Macromolecules* **1993,** *26* (20), 5396-5399.

146. Lee, H.; Kepley, L. J.; Hong, H. G.; Akhter, S.; Mallouk, T. E. *J. Phys.Chem.* **1988,** *92* (9), 2597-2601.

147. Lee, H.; Kepley, L. J.; Hong, H. G.; Mallouk, T. E. *J. Am. Chem. Soc.* **1988,** *110* (2), 618-620.

148. Hoekstra, K. J.; Bein, T. *Chem. Mater.* **1996,** *8* (8), 1865-1870.

149. Hong, H. G.; Sackett, D. D.; Mallouk, T. E. *Chem. Mater.* **1991,** *3* (3), 521-527.

150. Latos, E. J.; Payne, J. C., Corrosion inhibitors. US patent 4,409,121, October 11, 1983.

151. McNeel, T. E.; Harrell, J. A., Method for the reduction or prevention of tannin-staining on a surface susceptible to tannin-staining through the use of a complexing agent for a transition-metal ion and compositions containing such a complexing agent. US patent 5,320,872, June 14, 1994.

152. Bishop, M.; Bott, S. G.; Barron, A. R. *Chem. Mater.* **2003,** *15* (16), 3074-3088.

153. Schütte, M.; Kurth, D. G.; Linford, M. R.; Cölfen, H.; Möhwald, H. *Angew. Chem. Int. Ed.* **1998,** *37* (20), 2891-2893.

154. Linford, M. R.; Auch, M.; Möhwald, H. *J. Am. Chem. Soc.* **1998,** *120* (1), 178-182.

155. Lvov, Y.; Decher, G.; Moehwald, H. *Langmuir* **1993,** *9* (2), 481-486.

156. Caruso, F.; Niikura, K.; Furlong, D. N.; Okahata, Y. *Langmuir* **1997,** *13* (13), 3422-3426.

157. Jensen, D. S.; Kanyal, S. S.; Madaan, N.; Vail, M. A.; Dadson, A. E.; Engelhard, M. H.; Linford, M. R. *Surf. Sci. Spectra* **2013,** *20* (1), 36-42.

158. Madaan, N.; Kanyal, S. S.; Jensen, D. S.; Vail, M. A.; Dadson, A. E.; Engelhard, M. H.; Samha, H.; Linford, M. R. *Surf. Sci. Spectra* **2013,** *20* (1), 43-48.

159. Jiang, G.; Rivera, F.; Kanyal, S. S.; Davis, R. C.; Vanfleet, R.; Lunt, B. M.; Shutthanandan, V.; Linford, M. R. *Opt. Eng.* **2011,** *50* (1), 015201-015201-10.

160. Synowicki, R. A. *Thin Solid Films* **1998,** *313–314*, 394-397.

161. Sodhi, R. N. S. *Analyst* **2004,** *129* (6), 483-487.

Chapter 2 Porous, High Capacity Coatings for Solid Phase Microextraction (SPME) by Sputtering*

2.1 Abstract

A new process for preparing porous solid phase microextraction (SPME) coatings by the sputtering of silicon onto silica fibers is described. The microstructure of these coatings is a function of the substrate geometry and mean free path of the silicon atoms, and the coating thickness is controlled by the sputtering time. Sputtered silicon structures on silica fibers were treated with piranha solution (a mixture of conc. H_2SO_4 and 30% H_2O_2) to increase the concentration of silanol groups on their surfaces, and the nanostructures were silanized with octadecyldimethylmethoxysilane in the gas phase. The attachment of this hydrophobic ligand was confirmed by X-ray photoelectron spectroscopy (XPS) and contact angle goniometry on model, planar silicon substrates. Sputtered silicon coatings adhered strongly to their surfaces, as they were able to pass the Scotch tape adhesion test. The extraction time and temperature for headspace extraction of mixtures of alkanes and alcohols on the sputtered fibers were optimized (5 min and 40 °C), and the extraction performances of SPME fibers with 1.0 or 2.0 μm of sputtered silicon were compared to those from a commercial 7 μm poly(dimethylsiloxane) (PDMS) fiber. For mixtures of alcohols, aldehydes, amines, and esters, the 2.0 μm sputtered silicon fiber yielded signals that were 3 – 9, 3 – 5, 2.5 – 4.5, and 1.5 – 2 times higher, respectively, than those of the commercial fiber. For the heavier alkanes (undecane – hexadecane), the 2.0 μm sputtered fiber yielded signals that were ca. 1.0 – 1.5 times higher than the commercial fiber. The sputtered fibers

---

*This chapter has been reproduced with permission from (Anubhav Diwan, Bhupinder Singh, Tuhin Roychowdhury, DanDan Yan, Laura Tedone, Pavel N. Nesterenko, Brett Paull, Eric T. Sevy, Robert A. Shellie, Massoud Kaykhaii, and Matthew R. Linford), *Anal.Chem.* **2016**, 88, 1593-1600. Copyright 2016 American Society.

extracted low molecular weight analytes that were not detectable with the commercial fibers. The selectivity of the sputtered fibers appears to favor analytes that have both a hydrophobic component and hydrogen-bonding capabilities. No detectable carryover between runs was noted for the sputtered fibers. The repeatability (RSD%) for a fiber (n = 3) was less than 10% for all analytes tested, and the between-fiber reproducibility (n = 3) was 0 – 15%, generally 5 – 10%, for all analytes tested. The repeatabilities of sputtered fibers and the commercial 7 µm PDMS fiber are essentially the same. Fibers could be used for at least 300 extractions without loss of performance. More than 50 compounds were identified in a gas chromatography-mass spectrometry headspace analysis of a real world botanical sample with the 2.0 µm fiber.

2.2 Introduction

Solid phase microextraction (SPME) was first described in 1990 by Arthur and Pawliszyn.[1] It is a solvent-free technique that integrates into a single step analyte sampling, isolation, and concentration. It is relatively inexpensive, fast, and straightforward. In general, SPME employs a bonded phase, either solid or liquid, coated as a thin layer on a fiber substrate. The primary extraction mechanism of liquid bonded phases, e.g., poly(dimethylsiloxane) (PDMS) or polyacrylate, is absorption/partitioning.[2, 3] Solid bonded phases, e.g., PDMS-divinylbenzene (PDMS-DVB) or Carboxen-PDMS (CAR-PDMS), work mainly by adsorption.[2-4] Commercial SPME fibers generally suffer from one or more of the following drawbacks, which include relatively high cost, fragility, a low operating temperature range, swelling of the coatings in organic solvents, e.g., chlorinated solvents, which are common in chemical extraction, limited selectivity, carryover between runs (with careful method development, this can often be eliminated), loss of the coating during use (often through swelling during direct immersion extractions), and/or a relatively short lifetime (as low as 50 – 100 analyses).[5]

A number of interesting SPME bonded phases have been developed over the past few years that show different selectivities and/or address some of the issues raised above. All of these coatings have the drawback of rather tedious and cumbersome methods of preparation. For example, it takes more than 24 h to prepare fibers via a conventional sol-gel technique.[6]

Sputtering functions by the ejection of atoms from a target by collisions with energetic ions from a plasma. In general, sputtered films show excellent adhesion to their substrates.[7, 8] Sputtering has been used to develop materials for catalysis, optical devices, biochip arrays, and sensing devices.[9, 10] However, it has not been reported for making stationary phases for SPME.

This study focuses on the development of silica-based, porous, thin, ca. 1.0 and 2.0 µm, SPME coatings deposited via the sputtering of silicon. The deposition conditions (throw distance, pressure, and substrate geometry) lead to the production of vertical, porous, columnar structures that are well adhered to their substrates. After deposition, the sputtered silicon is hydroxylated with piranha solution (H_2SO_4/H_2O_2) and then rendered hydrophobic with octadecyldimethylmethoxysilane. Fibers are tested against commercial, 7 µm, PDMS fibers for extraction of alkanes, aldehydes, amines, esters, and primary alcohol standards. Fibers with ca. 2.0 µm of sputtered, silanized, porous silicon/silica consistently show noticeably better extraction efficiencies than commercial 7 µm PDMS fibers for almost all of the compounds tested. Fibers with ca. 1.0 µm of sputtered, silanized silicon also demonstrate better extraction performance than the commercial comparison in the cases of amines, alcohols and aldehydes. The repeatabilities and reproducibilities of these fibers are good (%RSD values generally less than 10%), and linear ranges, limits of detection, and limits of quantitation for representative compounds are provided. The fiber coatings are strongly adhered to their substrates. Sputtered fibers do not show detectable carryover between runs. These new sputtered, silanized fibers show good lifetimes – they have been used in excess of 300 times without showing any decrease in performance – these fibers appear to have retained complete integrity to this point in the testing. There are reports in the literature of commercial fibers being used for over 600 extraction cycles in headspace mode.[11] All extractions described in this work are of the headspace variety.

2.3 Experimental

2.3.1 Materials and Reagents

Polyimide coated silica fibers were obtained from Polymicro Technologies (Downers Grove, IL). Commercial SPME fibers were obtained from Sigma Aldrich (St. Louis, MO), and included 7 µm PDMS. Empty SPME assemblies were also obtained from Sigma Aldrich. A silicon sputtering target (99.999 %) with a copper backing plate was obtained from Plasmaterials (Livermore, CA). The primary alkanes: decane (99%), undecane (99%), dodecane (99%), tridecane (99%), tetradecane (99%), pentadecane (99%), and hexadecane (99%), the primary alcohols: heptanol (98%), octanol (99%), nonanol (98%), decanol (99%), and dodecanol (98%), the primary aldehydes: heptanal (95%), octanal (95%), nonanal (95%), and decanal (95%), the primary amines: heptyamine (99%), octylamine (99%), and decylamine (95%), and the esters: propyl propionate (99%), butyl propionate (99%), pentyl propionate (99%), and ethyl octanoate (99%) were obtained from Sigma Aldrich. The n-octadecyldimethylmonomethoxysilane was purchased from Gelest (Morrisville, PA). Sulfuric acid (Macron Fine Chemicals, Center Valley, PA) and hydrogen peroxide (30%) Fisher Scientific, Pittsburgh, PA) were used to prepare the piranha solution.

2.3.2 Silica Fiber Preparation

Polyimide-coated silica fibers (140 µm in diameter) were cut into ca. 3.3 cm lengths, and the polyimide was burned off. The resulting fibers were 120 – 124 µm in diameter. The fibers were visually inspected to confirm the absence of any remaining polyimide.

2.3.3 Sputter Deposition

Cut, bare fibers were fixed onto the platen (sample holder) of a commercial PVD 75 sputter system (Kurt J. Lesker Co., Pittsburgh, PA) such that the fibers were positioned essentially perpendicular to the platen and to the target. The platen was located ca. 20 cm above the target, it was not rotated, and the fibers were positioned within 1 – 2 cm over the center of the sputter target, which was 3” (7.6 cm) in diameter. Silicon was then DC magnetron sputtered at 4 mTorr and 200 W power. Argon was employed as the sputtering gas. Witness silicon wafers, which also hung perpendicular to the platen, were placed near the fibers to confirm the depositions. The deposition rate of silicon in laboratory sputter system, as measured at the tip of the fibers (closest to the target, 17 cm throw distance), and under the conditions mentioned herein, was 370 nm/h.

2.3.4 Hydroxylation of Silica Surface

Fibers with sputtered silicon coatings were treated in piranha solution[12-15] (7:3 conc. H_2SO_4 : conc. H_2O_2) at 85 °C for 45 min to increase the concentration of silanol groups on their surfaces. *Warning: while piranha solution, a mixture of concentrated* H_2SO_4 *and* H_2O_2*, is very extensively used for cleaning and treating silicon surfaces, it is dangerous and should be handled with great care, proper protective equipment, and only after appropriate training. It is similar in composition to other cleaning solutions that are widely used in the semiconductor industry. It should be disposed of in accord with safe chemical handling procedures and in accord with local, state, and* *federal regulations*. After hydroxylation, the fibers were rinsed with ultra-high purity water and dried under nitrogen. Freshly prepared piranha solution was used for each surface hydroxylation.

2.3.5 Silanization of Hydroxylated SPME Fibers

Octadecyl (C18) chains were bonded to sputtered, hydroxylated silica surfaces via vapor phase silanization[16] in a homemade oven with a base pressure of 0.5 Torr. A small amount of the C18 silane (0.1 mL of n-octadecyldimethylmonomethoxysilane) was injected into the evacuated oven through a septum. The oven temperature was 200 °C. The vapors of the silane were allowed to remain in the chamber for 20 min. The chamber was purged three times to remove the unreacted silane.

2.3.6 Attachment of Fibers to SPME Assemblies

Fibers were attached to the plunger needle of SUPELCO SPME assemblies using an epoxy glue: EPO-TEK 353ND-T (Epoxy Technologies, Billerica, MA). The final length of the exposed fibers in the assemblies was ca. 1.0 cm.

2.3.7 Test Mixture Preparation and GC-FID Conditions

An alcohol test mixture for headspace extraction contained 1 ppm (v/v) each of heptanol, octanol, nonanol, decanol, and dodecanol in water. This solution was prepared by dissolving 10 μL of each alcohol in 10 mL of ethanol. To prepare aqueous solutions for SPME, 10 μL of the stock solution was diluted with 10 mL of ultra-high purity water to obtain 1 ppm (v/v) concentrations of the alcohols. For SPME, 5 mL of this aqueous test solution was placed in a 20 mL SPME vial. In a similar fashion, aldehyde, amine, esters, and alkane test mixtures were prepared, with the exception that for the primary amines, the final concentration of each amine in water was 10 ppm, and for the alkanes, the final concentration of each alkane in water was 0.1 ppm. A fresh stock solution was prepared each time a series of fibers was compared. These concentrations are lower than at least some of those reported in the literature. For example, in their SPME work, Xu et al.[17] used a concentration of 0.2 ppm for their alkane solution (this was immersion, not headspace sampling of their sample), and Gholivand et al.[18] used a concentration of 50 ppm for their headspace extraction of BTEX compounds (benzene, toluene, ethylbenzene, and xylene).

2.3.8 Instrumentation/Testing

A Hewlett Packard 6890 series GC with a flame ionization detector (FID) was used to separate all of the analytes used/studied in this work, except those from the hops analysis. The GC system had a Gerstel (Mülheim an der Ruhr, Germany) multipurpose sampler with a robotic arm that performed the SPME extractions. An HP-5 GC column from Agilent Technologies (Santa Clara, CA, part number 19091J-413) composed of (5%-phenyl)-methylpolysiloxane was used. The column dimensions were 30.0 m x 0.32 mm I.D. x 0.25 µm film thickness. The temperature limits for this column were -60 °C to 325/350 °C. Prior to any extraction, SPME fibers were preconditioned in the injection port of the GC instrument for 3 h at 320 °C. GC desorption and separation conditions included: desorption time: 1 min, desorption temperature: 280 °C, initial column temperature: 70 °C, ramp rate/parameters: 20 °C/min to 200 °C followed by a ramp of 30 °C/min to 280 °C with a hold at this temperature for 0.50 min. The total run time for each analysis was 10.67 min.

Carryover effects were studied using mixtures of the same concentration to make comparisons between commercial and sputtered fibers: alkanes (0.1 ppm), alcohols (1 ppm), esters

(1 ppm), aldehydes (1 ppm), and amines (10 ppm). Carryover was not observed when a fiber was desorbed for 1 min immediately after it was used for a complete run, i.e., a head space extraction of 5 min and desorption of the fiber for 1 min in the GC.

Hop (*Humulus lupulus*) samples, grown in Tasmania, Australia, were added to 20 mL SPME vials from Sigma-Aldrich (0.25 g of dry hop flour, which filled ca. ¼ of the vial). The gas chromatography-mass spectrometry (GC-MS) analyses of the hops were carried out on a QP2010 Plus (Shimadzu, Kyoto, Japan) system equipped with an COMBI autosampler. Separations were performed on 30 m × 0.25 mm ID × 0.25 μm (film thickness) SLB-5ms column from Supelco (Bellefonte, PA). The GC conditions were as follows: injector, split/splitless: 230 °C; injection volume: 1.0 μL; carrier gas: He, at a linear velocity of 28.3 cm/s (constant), splitless; oven temperature program: 60 °C to 250 °C at 5°C/min, hold for 5 min. The MS conditions were set as follows: ion source temperature: 220 °C, interface temperature: 250 °C, and scan range: 40 – 400 *m/z*, with an acquisition frequency of 5 Hz. For MS identification, a library, FFNSC 2, 2011, was mainly used, along with FO, Parfum, and National Institute of Standards and Technology (NIST08) libraries. Identification was carried out with the GCMS solution software (Shimadzu, Kyoto, Japan), which allowed application of two filters: minimum similarity percentage (set at 90%) and LRI (linear retention index) range (set at ± 10 units). In order to determine LRI values, a *n*-alkane mixture ($C_8 – C_{20}$) was analysed under the same operational conditions as the sample.

Film thicknesses on planar substrates were measured at an incident angle of 75° with an M-2000 spectroscopic ellipsometer (J.A. Woollam, Co. Lincoln, NE), and the data were analyzed using the instrument software over a wavelength range of 300 – 1700 nm. A Scotch tape adhesion test was performed with standard, semi-transparent Scotch tape. After this test, wafers were sonicated in acetone to remove any residues that may have been left from the tape. Water contact angles (WCA) were measured with a Ramé-Hart (Netcong, NJ) Contact Angle Goniometer (Model 100-00) fitted with a manual syringe that was filled with high purity (18 MΩ) water. The drop sizes for measuring static water contact angles were ca. 10 µL. X-ray photoelectron spectroscopy (XPS) was performed with a Surface Science SSX-100 X-ray photoelectron spectrometer (serviced by Service Physics, Bend, OR) with a monochromatic Al K_α source, a hemispherical analyzer, and a take-off angle of 35°. Survey scans were recorded with a spot size of 800 µm x 800 µm and a resolution of 4 (nominal pass energy of 150 eV). Peaks were referenced to the C 1s hydrocarbon signal at 284.6 eV. An electron flood gun was employed for charge compensation. Scanning electron microscopy (SEM) was performed with a Helios NanoLab TM 600 instrument (FEI, Hillsboro, OR). Prior to SEM, samples were sputtered with 12 nm of gold to prevent charging.

2.4 Results and Discussion

2.4.1 Preparation of SPME Fibers

SPME coatings were prepared by sputtering silicon onto bare silica fiber substrates (Figure 2.1). The fibers were positioned above and perpendicular to the silicon target so that they would be coated in a radial fashion. Figure 2.2a - b shows SEM images of a 2.0 µm silicon coating. A cross-sectional image (Figure 2.2a) shows columnar features. A top view of the coating (Figure 2.2b) shows a cauliflower-like morphology. These images suggest a considerable degree of porosity in the films. Similar images were obtained for thinner coatings (Figure 2.3). As is typical in sputter depositions, the thicknesses of the coatings were proportional to the sputter time. Because of the fiber orientation, the coatings on the sputtered fibers were somewhat tapered. For example, the silica fiber with the 1.0 µm sputtered silicon coating employed in these studies was ca. 1.2 µm thick at its base (closest to the target) and 0.9 µm thick 1 cm further from the target.

Similarly, the 2.0 μm fiber employed for these studies was 2.2 μm thick at its base and 1.9 μm thick 1 cm above the point. This decrease in thickness (tapering) can be explained by the general $1/r^2$ type dependence expected for the target, i.e., the same flux spread over a larger surface area as it proceeds further and further from the target. Obviously, this dependence breaks down close to the target (it is not a point source), and it does not take into account the mean free paths of the sputtered particles (vide infra).

To demonstrate the importance of fiber orientation, silica fibers were also positioned parallel to the target and sputter coated. The resulting SEM images (see Figure 2.2c) showed a much more closed morphology that indicated greatly reduced porosity. The results from these parallel and perpendicular fiber positions (Figure 2.2) are reminiscent of Thornton's report on structure zone models in sputtering, which was illustrated with sputtering into a recessed feature.[19] The walls of the recess showed a highly voided coating (more similar to the structures on our fiber positioned perpendicular to the target, Figures 2.2a – b), while the flat bottom of his substrate showed a mirror-like surface (more similar to the structures on our fiber that lay parallel to the target, Figure 2.2c).

2.4.2 Mean Free Path Calculations

Calculations of the mean free path of Si atoms in Ar at 4 mTorr deposition pressure are consistent with loss of directionality of the flux and thus the formation of voided structures. As mentioned in the Introduction chapter (section 1.2.6), if sputtering occurs at high enough pressures that the mean free path of the impinging atoms is shorter than the target-substrate distance, the impinging atoms lose the directionality they had when they left the target, which results in the atoms approaching the substrate from multiple angles. The mean free path of Si atoms in an Ar background can be calculated by:

$$\lambda = 1/\sqrt{2}\rho\sigma \tag{2.1}$$

where σ is the collision cross section and ρ = N/V is the total gas density. Assuming ideal gas behavior, which is valid at the low pressure and relatively high temperature of the experimental conditions, we can use the ideal gas law to rewrite the expression for the mean free path as

$$\lambda = RT/\sqrt{2}N_A\rho\sigma \tag{2.2}$$

Because it is reasonable to assume that the amount of gas phase Si is small, i.e., almost all of the gas is Ar, the total pressure is given by the pressure of the Ar, p = 4 mTorr. The collision cross section is given by:

$$\sigma = \pi d^2 \tag{2.3}$$

where d is the average hard sphere collision diameter of Si and Ar given by

$d = \frac{1}{2}(d_{Ar} + d_{Si}) = 402\ pm.$ The diameters of Ar and Si were approximated from their Van der Waal radii, 210 pm for Si and 192 pm for Ar. Using these values at T = 298 K, the mean free path of Si in an Ar bath is 1.07 cm. Given that the throw distance between the target and the tip of our fibers (17 cm) is much greater than the mean free path, it is highly probable that silicon atoms will undergo multiple collisions and, therefore, lack directionality when they strike the fiber substrate, arriving at the substrate from a range of angles. This would certainly help explain both the porous (shadowed) morphology of the resultant films and the formation of structures oriented perpendicular to the substrates.

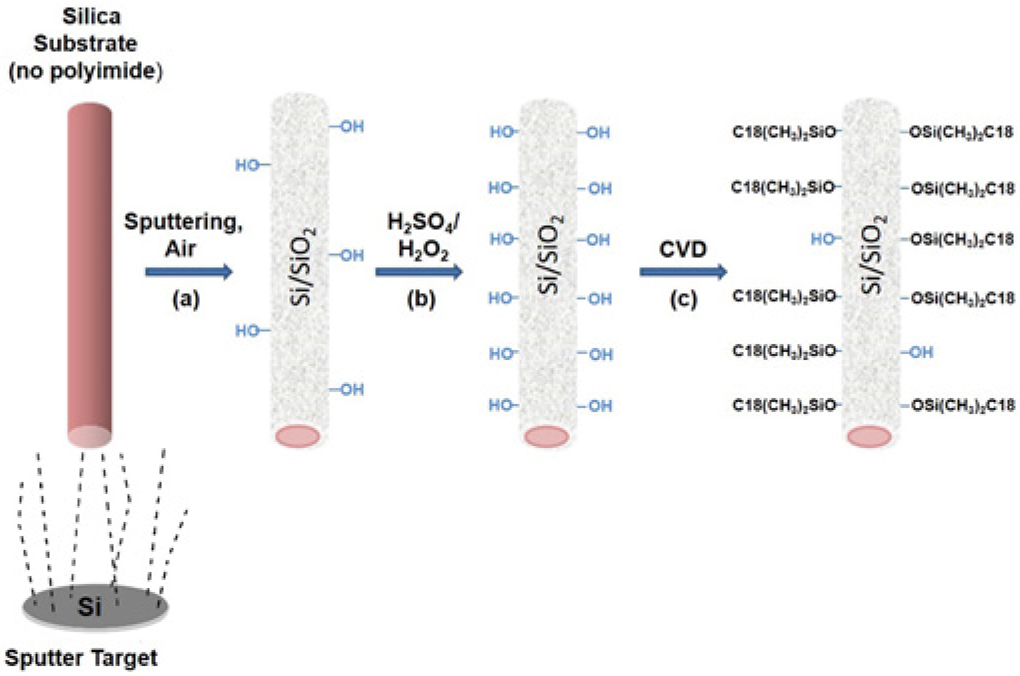

Figure 2.1 Process for preparing sputtered, silanized SPME fibers. (a) Sputtering of Si and exposure to air. (b) Treatment with piranha solution. (c) CVD of octadecyldimethylmethoxysilane.

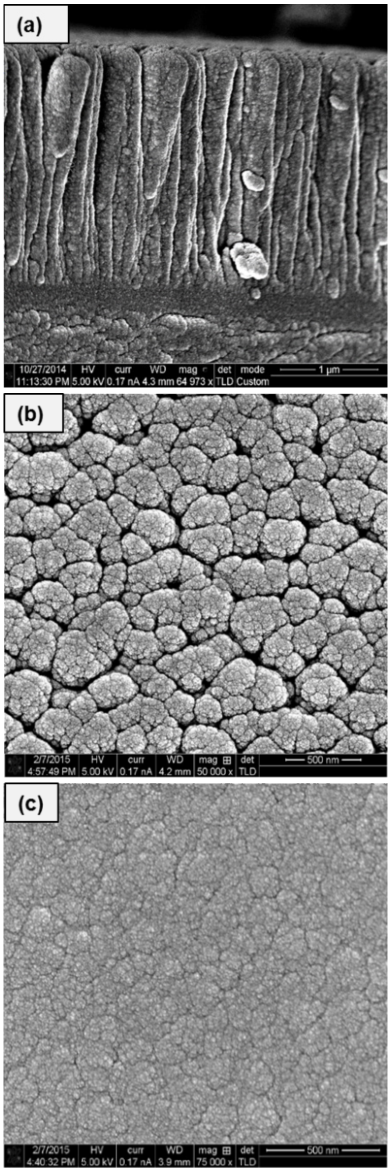

Figure 2.2 Profile (a), and top (b) SEM images of ca. 2 μm sputtered silicon coatings on silica fibers that had been positioned perpendicular to the target. (c) Top view of a silica fiber positioned horizontally to the target that was also sputtered with silicon.

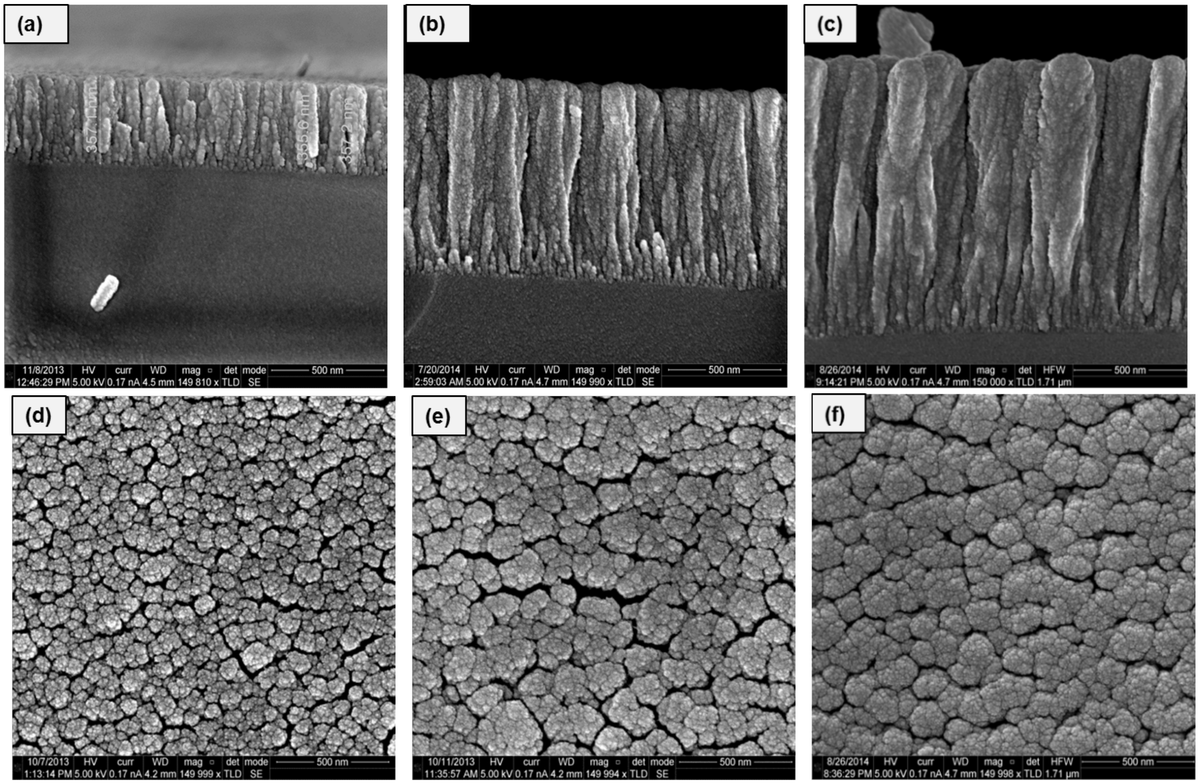

Figure 2.3 SEM profile and top views of silicon that was sputtered onto silica fibers for different times: (a) and (d) 1 h (measured at the thinner end of the fiber), (b) and (e) 2 h (measured at the thicker end of the fiber), and (c) and (f) 3 h (measured at the thicker end of the fiber).

To better study the surface chemistry of sputtered fibers, model, planar silicon wafers were positioned perpendicular to the target and sputtered with silicon. They were then characterized with multiple analytical techniques/methods.[20, 21] By SEM they showed the same morphology seen in Figure 2.2b for the fibers. That oxygen was present on these model surfaces was confirmed by X-ray photoelectron spectroscopy (XPS) – note the large O 1s signal in Figure 2.4a. As expected, this surface showed a very small amount of carbon by XPS – essentially all surfaces have a small amount of adventitious carbon. Also as expected, these model surfaces were wet by water after they were made, i.e., their advancing, receding, and static water contact angles were below 15° (Figure 2.5).

Vapor phase deposition of octadecyldimethylmethoxysilane, a monofunctional C18 silane, was performed on the planar, sputtered silicon wafers described in the previous paragraph, which then showed (i) a larger C 1s signal by XPS (see Figure 2.4b), and (ii) advancing and static water contact angles of 60 – 70° (Figure 2.5). These results are consistent with a moderate amount of a reaction occurring between the C18 silane and the surface. (After sputtering, the surface of the silicon was expected to react, to some degree, with water and oxygen in the air to produce some silanols.) However, these water contact angles are low compared to those expected from a densely packed monolayer of C18 groups on silica. Suspecting that a lack of surface silanols was limiting this reaction, prior to silanization the model surfaces were treated with piranha solution. After piranha treatment and silanization, these surfaces showed significantly more carbon by XPS (see Figure 2.4c), and advancing and static water contact angles of ca. 120° (Figure 2.5). That this value is greater than ca. 110°, which is the value expected for a complete monolayer of densely-packed alkyl groups,[22, 23] is attributed to surface roughness.[24] C 1s/Si 2p area ratios determined from XPS narrow scans (see caption to Figure 2.4) indicate that piranha treatment had increased the amount of carbon on these surfaces by about a factor of three. As expected, the carbon on the surfaces appeared to be primarily in a reduced state: C(0).[25] As an additional control to the C18 silanizations, each silane deposition onto each batch of silica fibers included a witness silicon wafer (air plasma cleaned, but otherwise untreated/unsputtered) that was monitored by spectroscopic ellipsometry (SE). For these wafers, the thicknesses of their native oxide layers were determined by SE before silanization, and the thickness of the native oxide and silane, all modeled as silicon dioxide,[26] were determined after silanization. For all of these silanizations, the increase in film thickness was 1.1 – 1.2 nm, and the advancing and receding water contact angles were 102° and 82°, respectively. These numbers compare very favorably to monolayers on silicon dioxide obtained from neat, heated octadecyldimethylchlorosilane, a very similar monofunctional adsorbate, which showed thicknesses of 1.0 nm, advancing and receding water contact angles of 100° and 86°, respectively, and XPS C 1s/Si 2p ratios of 1.18, where a C 1s/Si 2p ratio of 1.09 on piranha treated, sputtered silicon surfaces was obtained (see Figure 2.4).[27] Silanization was necessary for the performance of sputtered SPME fibers – unsilanized fibers showed no extraction capability. (Of course, 'C18' is the most commonly employed stationary phase in high performance liquid chromatography (HPLC). Finally, the robustness of the sputtered silicon films was investigated via the Scotch-tape adhesive test. This is a well-accepted test in surface analysis[28] that simply consists of pressing a piece of Scotch tape against a surface and then pulling it away. Thin films and materials that can withstand this test are regarded as well adhered to themselves and to their substrates. SEM micrographs of sputtered silicon coatings on silicon wafers before and after this test are indistinguishable (Figure 2.6).

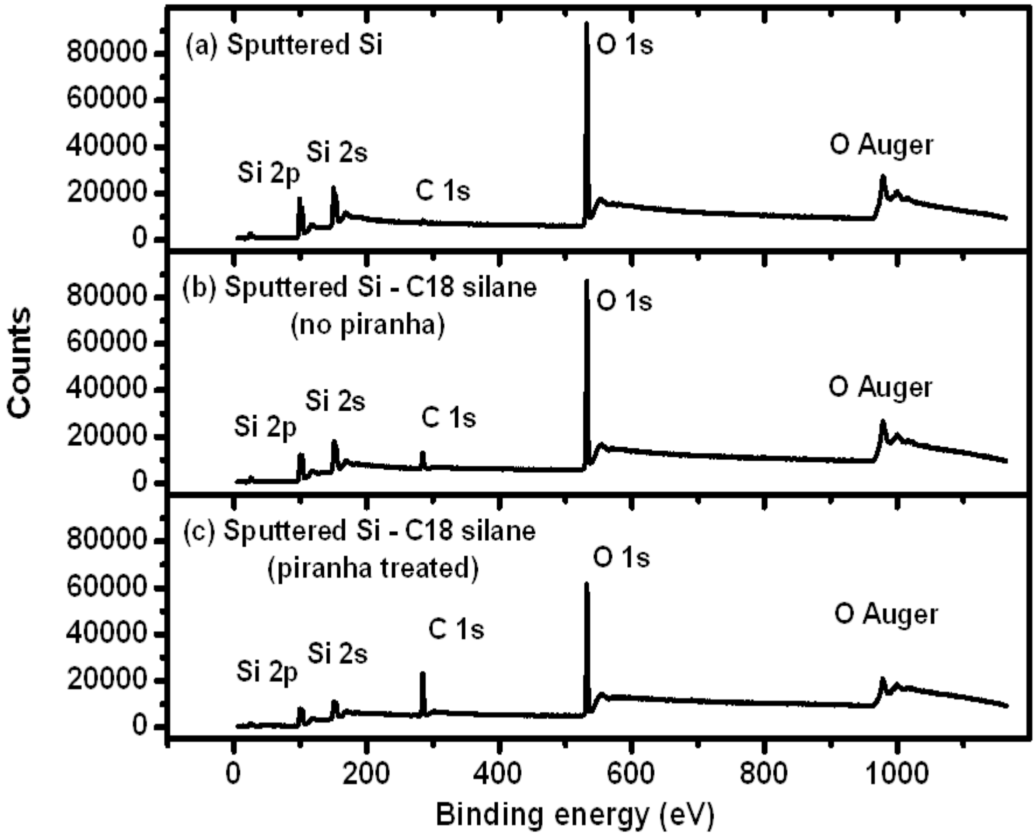

Figure 2.4 XPS survey spectra of silicon sputtered onto a planar surface that had been positioned perpendicular to the target (a) before silanization (C 1s/Si 2p ratio of 0.04), (b) with silanization but without piranha treatment (C 1s/Si 2p ratio of 0.30), and (c) with piranha treatment and silanization (C 1s/Si 2p ratio of 1.09).

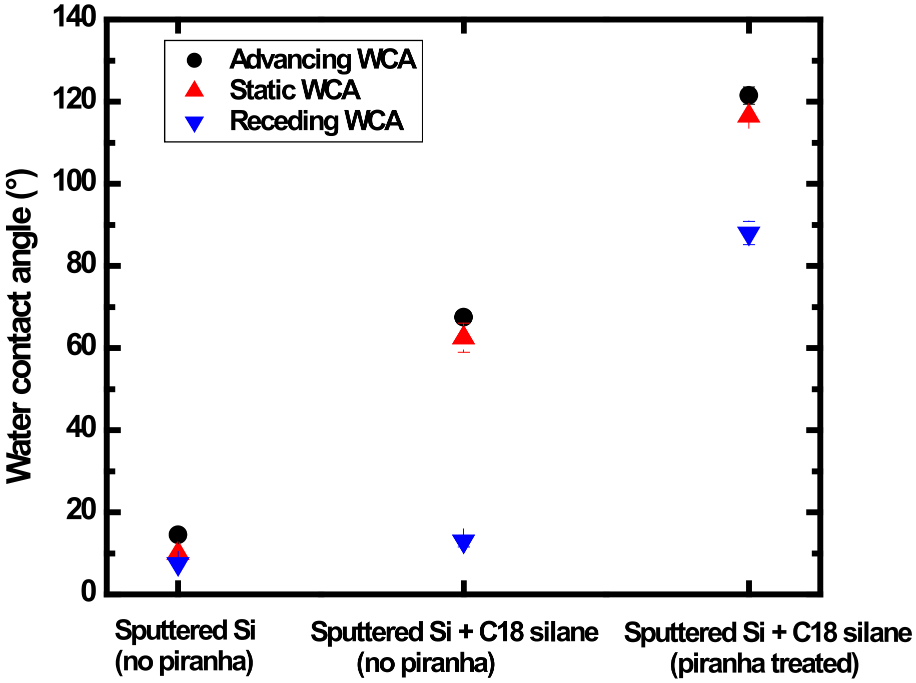

Figure 2.5 Advancing, static, and receding water contact angles of sputtered, planar silicon surfaces: initially (no piranha treatment), after silanization with the C-18 silane but without previous piranha treatment, and after piranha treatment and silanization.

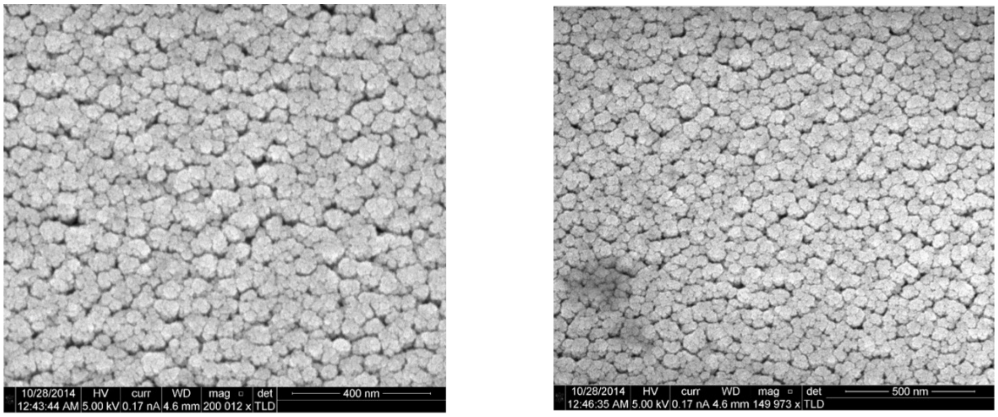

Before

After

Figure 2.6 SEM micrographs of sputtered silicon (1 h sputtering) on planar silicon shards before (400 nm scale bar) and after (500 nm scale bar) a Scotch tape adhesion test.

2.4.3 SPME

2.4.3.1 Fiber Preconditioning and Thermal Stability

Sputtered, silanized SPME fibers were preconditioned in the port of a GC instrument at 320 °C for 3 h. Preconditioning presumably removes unreacted C18 chains and/or other impurities. Preconditioning only needs to be performed once for a fiber. During preconditioning, the response of the fiber to a mixture of alkanes was monitored. At 3 h, this response became constant. To test the stability of the fibers, this thermal treatment was extended for up to 7 h, during which time no change in the fiber response took place (see Figure 2.7).

2.4.3.2 Extraction Time

Headspace extraction time profiles were determined for mixtures of alcohols and alkanes at 1, 3, 5, 7, 10, and 15 min using the 2.0 µm SPME fiber (see Figures 2.8a and 2.9a). Results from both sets of analytes suggest competitive displacement, i.e., an adsorptive not absorptive mechanism, as evidenced by increasing responses with time for the heavier analytes at the expense of the lighter ones. Based on these profiles, an extraction time of 5 min was selected for future experiments.

2.4.3.3 Extraction Temperature

A series of alcohols and alkanes were headspace extracted from 30 – 70 °C or 30 – 80 °C, respectively, to determine the optimal SPME extraction temperature for 2.0 µm sputtered fiber. Analyte adsorption onto the fibers is expected to be exothermic and to represent a decrease in entropy. Accordingly, lower temperatures should favor analyte adsorption, with the caveat that vapor pressures decrease with sample temperature. This trade off appears to be in place for analytes tested. The lighter analytes showed an immediate decrease in signal with increasing temperature, while the heavier analytes showed an initial increase in signal, followed by a decrease. These phenomena may be a result of competitive displacement. From the extraction temperature profiles of the alcohols and alkanes (see Figures 2.8b and 2.9b), 40 °C appeared to be the most suitable extraction temperature.

2.4.4 Comparison of 1.0 and 2.0 μm Sputtered, Silanized SPME Fibers to Commercial Fibers

The performance of 1.0 and 2.0 μm sputtered, silanized SPME coatings was evaluated with sample mixtures of alcohols, amines, aldehydes, esters, and alkanes. Results from these fibers were compared under the same analysis conditions to those obtained with a commercial 7 μm PDMS fiber, which is one of the most commonly used SPME fibers. Both the PDMS fiber and sputtered fibers are hydrophobic, which suggests that their selectivities may be somewhat similar. It is noteworthy that the PDMS fiber coating is 3.5 times thicker than that of 2.0 μm sputtered fiber.

Figure 2.10a shows a comparison of the extraction of a series of primary alcohols: 1-heptanol, 1-octanol, 1-nonanol, 1-decanol, and 1-dodecanol from water with the 1.0 and 2.0 μm sputtered fibers and with the 7 μm PDMS fiber. Here, the 2.0 μm sputtered fiber showed signals that were from ca. 3 – 9 times greater than those of the PDMS fiber, while the 1.0 μm sputtered fiber showed signals that were ca. 1.5 – 2.2 times greater. For the amine sample mixture, the 2.0 μm sputtered fiber yielded signals that were ca. 2.5 – 4.5 times greater than the PDMS fiber, while the 1.0 μm sputtered fiber gave signals that were ca. 1.5 – 2.0 times greater. Heptanol was also present in the alcohol sample mixture, but it was only detected with the 2.0 μm sputtered fiber. Similarly, heptylamine was included in the amine analyte mixture, but it was only detected with the two sputtered fibers. For the series of aldehydes (Figure 2.10b): heptanal, octanal, nonanal, and decanal, the 2.0 μm sputtered fiber gave signals that were ca. 3.0 – 5.0 times greater than those from the 7 µm PDMS fiber, while the 1.0 µm sputtered fiber gave signals that were ca. 1.1 – 1.7 times greater. For the series of esters: propyl propionate, butyl propionate, pentyl propionate, and ethyl octanoate (Figure 2.10c), the signal from the 2.0 µm sputtered fiber was ca. 1.5 – 2.0 times greater than that of the 7 µm PDMS fiber, while the signal from the 1.0 µm sputtered fiber was ca. 0.6 – 0.8 of that from the 7 µm PDMS fiber. Finally, Figure 2.10d shows the results from the extractions of a series of *n*-alkanes: decane, undecane, dodecane, tridecane, tetradecane, pentadecane, and hexadecane. For the 2.0 µm sputtered fiber, the signals from decane and undecane are ca. 0.7 and 0.9 of the signal from the PDMS fiber, while all of the signals of the higher molecular weight analytes exceed those of the 7 µm PDMS fiber by factors of ca. 1.2 – 1.6. The signals from all of the alkanes on the 1.0 µm sputtered fiber were less than those of the 7 µm PDMS fiber, where these signals increase with analyte molecular weight, becoming nearly equal to the signal from the PDMS fiber at the heaviest analyte (hexadecane). Repeatabilities (n = 3, RSD%) for the alcohols, amines, aldehydes, esters, and alkanes were measured for each compound in each analyte mixture on 2 µm sputtered fibers and also the commercial 7 µm PDMS fiber. The resulting RSD% values for our fiber were generally 5 – 10 %. The between-fiber reproducibility (n = 3) of sputtered fiber was also evaluated, with values ranging from 0 – 15 %, and in general from 5 – 10 %.

The results in Figure 2.10 suggest an explanation for the selectivity of sputtered fibers. Both 1.0 and 2.0 µm fibers perform better than PDMS for the alcohols, amines, and aldehydes. For both the esters and the alkanes, 1.0 µm fiber gave lower signals than the PDMS, while 2.0 µm fiber outperforms the PDMS fiber (for both the esters and the higher molecular weight alkanes). These results suggest that hydrogen bonding interactions, in addition to hydrophobic interactions from the C18 chains, play a key role in analyte binding. Thus, the fibers show the greatest extraction efficiency for primary alcohols, primary amines, and aldehydes, all of which have exposed functional groups that are capable of hydrogen bonding, presumably with surface silanols. The presence of such silanols seems reasonable – the surfaces were treated with piranha solution, and it is not possible to completely silanize a fully hydrated surface of silanol groups on silica.[29] The extraction performance of the sputtered fibers decreases for the esters, which contain a polar functional group that is sandwiched by alkyl groups (sterically limited), and then even more for the alkanes, which obviously contain no polar functionality. Finally, I note the substantially improved performance of the 2.0 μm fiber compared to the 1.0 μm fiber. It may be that with additional sputtering, the channels in the 2.0 μm fibers become narrower, which may then better hold (trap) analytes. In addition, the thicker coating should provide a thicker diffusion barrier for analytes to escape from, and therefore better trap analytes. There is some suggestion of a change in surface morphology with sputtering time (see Figure 2.3). These possibilities will be explored in future work.

Finally, we compared 2 μm fiber to a commercial CAR-PDMS fiber that was specifically designed for extraction of low molecular weight molecules. This fiber had a coating thickness of 75 μm. As expected, 2 μm fiber outperformed the commercial fiber for the higher molecular weight analytes, but was less effective for the lower molecular weight species (Figure 2.11).

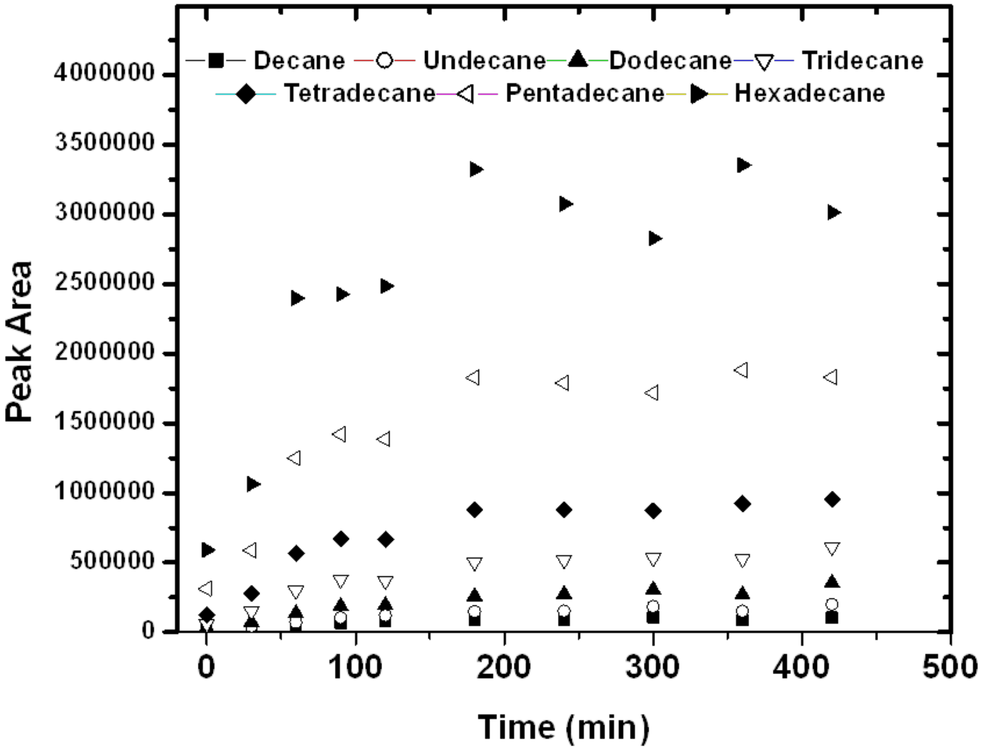

Figure 2.7 Signals (peak areas) with a 2.0 μm fiber from a mixture of alkanes after preconditioning at 320° C for different periods of time. The percent relative standard deviation (RSD %) for hexadecane was 7.0 % for the data points obtained after 180 min.

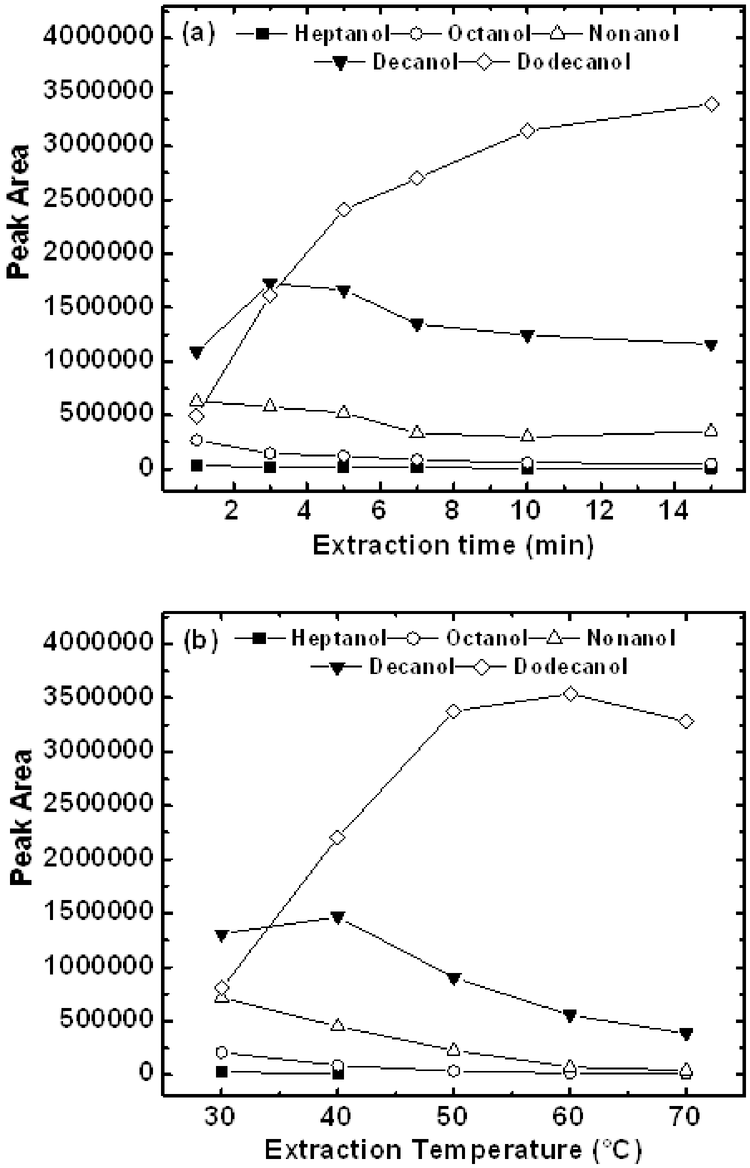

Figure 2.8 (a) Headspace extraction time profile of the 2.0 µm sputtered, silanized fiber for a mixture of alcohols at an extraction temperature of 40 °C. (b) Headspace extraction temperature profile of the 2.0 µm sputtered, silanized fiber for a mixture of alcohols at an extraction time of 5 min. Extraction conditions in both experiments were: incubation time: 15 min, incubation agitation speed: 500 rpm, desorption temperature: 280 °C, desorption time: 1 min, sample volume: 5 mL.

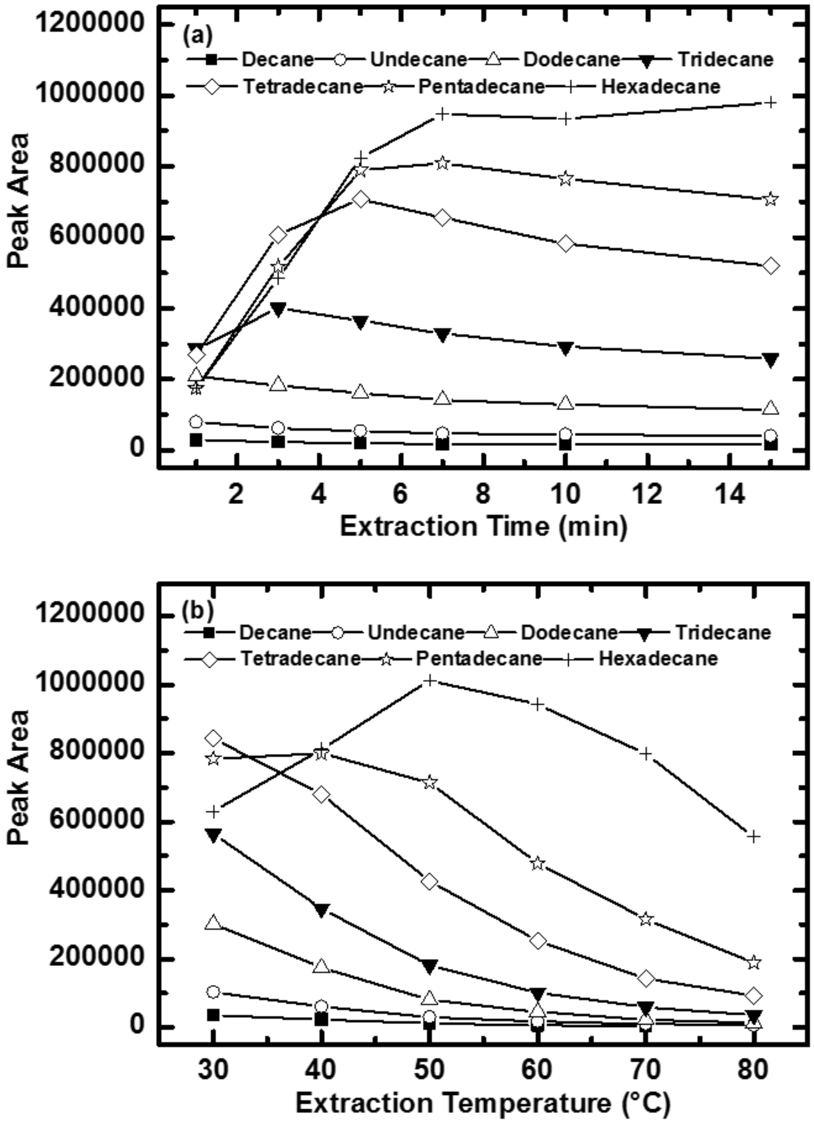

Figure 2.9 (a) Headspace extraction time profile of the 2.0 µm sputtered, silanized fiber for a mixture of alkanes at an extraction temperature of 40 °C. (b) Headspace extraction temperature profile of the 2.0 µm sputtered, silanized fiber for a mixture of alkanes at an extraction time of 5 min. Extraction conditions in both experiments were: incubation time: 15 min, incubation agitation speed: 500 rpm, desorption temperature: 280 °C, desorption time: 1 min, sample volume: 5 mL.

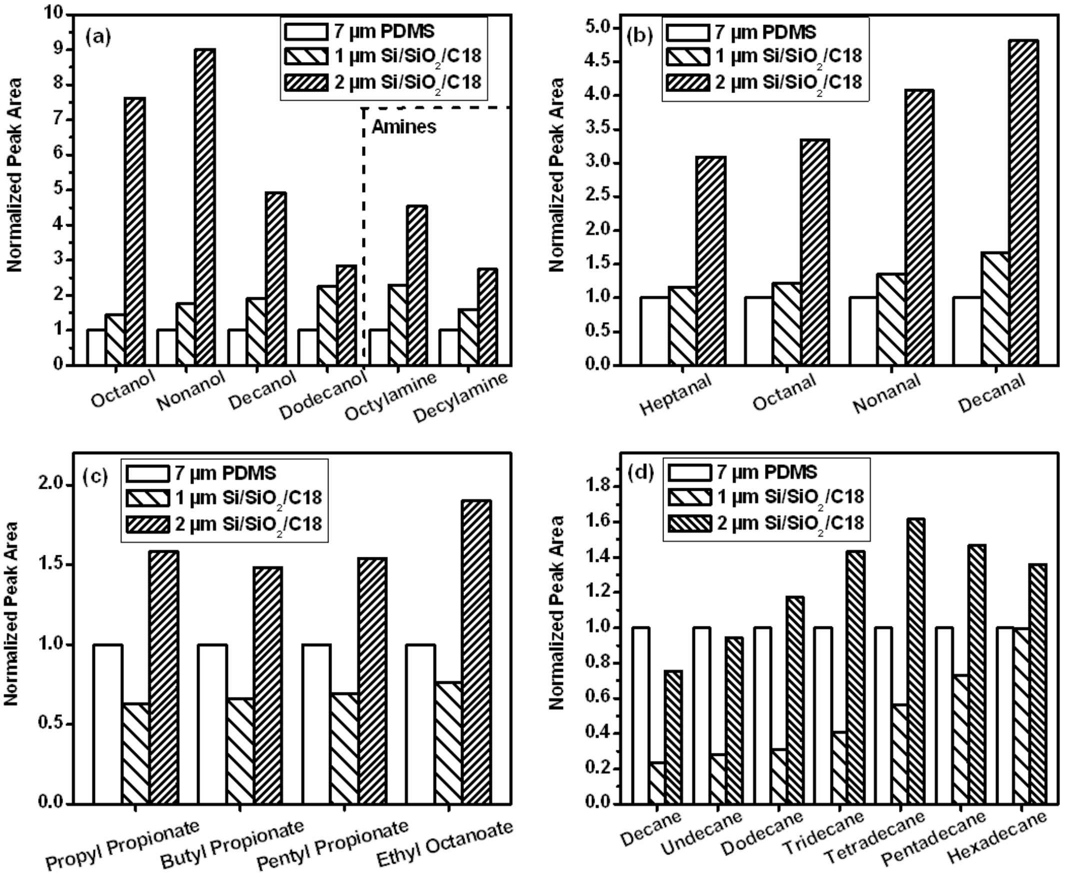

Figure 2.10 Comparison of the signals from 1.0 µm $Si/SiO_2/C18$, and 2.0 µm $Si/SiO_2/C18$ sputtered fibers normalized to those from a commercial 7 µm PDMS fiber (a) 1 ppm (each analyte) mixture of alcohols and 10 ppm (each analyte) mixture of amines. (b) 1 ppm (each analyte) mixture of aldehydes, (c) 0.1 ppm (each analyte) mixture of alkanes, (d) 1 ppm (each analyte) mixture of esters. Peak areas were normalized with respect to the respective signals from the commercial, 7 µm PDMS fibers. Extraction conditions were: incubation time: 15 min at 40 °C, incubation agitation speed: 500 rpm, extraction time: 5 min, extraction temperature: 40 °C, desorption temperature: 280 °C, desorption time: 1 min, sample volume: 5 mL.

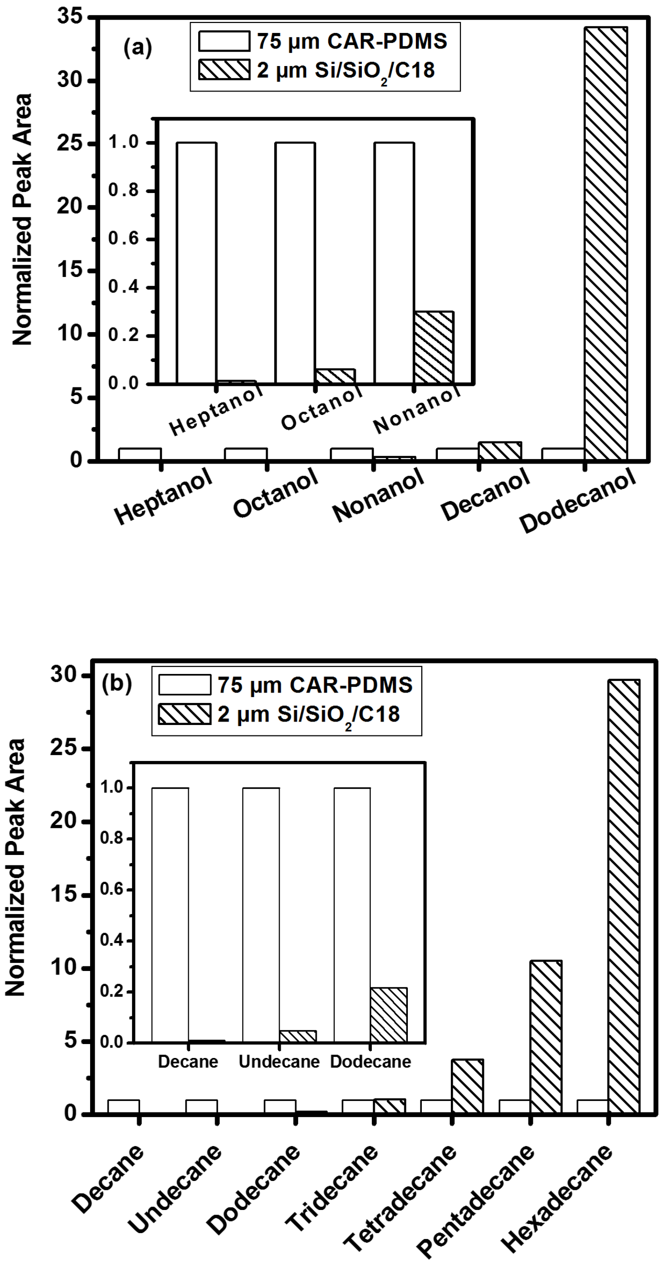

Figure 2.11 Comparison of the signals from 2.0 µm Si/SiO$_2$/C18 sputtered fibers normalized to those from a commercial 75µm CAR-PDMS fiber. (a) 1 ppm (each analyte) mixture of alcohols, and (b) 0.1 ppm (each analyte) mixture of alkanes. Extraction conditions were: incubation time: 15 min at 40 °C, incubation agitation speed: 500 rpm, extraction time: 5 min, extraction temperature: 40 °C, desorption temperature: 280 °C, desorption time: 1 min, sample volume: 5 mL.

2.4.5 *Linearity, Limits of Detection, Limits of Quantitation, and Carryover Effects*

The linear range previously reported for decanal using a 3-5 µm ZnO SPME fiber is 50-5000 (µg/L).[30] A commercial fiber, 85 µm CAR-PDMS, gave a linear range from 100-5000 (µg/L) for this same compound.[30] The linear range for decanal with 2 µm sputtered fiber, which has a much thinner coating, is 40 – 1000 (µg/L) (see Table 2.1). The linear range for hexadecane is very similar. Limits of detection (LOD) and quantitation (LOQ) for these compounds were also determined (Table 2.1). With regards to their lifetimes, fibers appear to be reusable at least 300 times without loss of performance. I did not see carryover between runs with sputtered fibers (Figure 2.12).

2.4.6 *Analysis of a Real World Sample*

To help determine sputtered fiber's ability to analyze a real world sample, headspace extractions of hops, a flavoring agent for beer, were performed.[31] Making beer involves multiple steps, one of which includes boiling a precursor liquid (the 'wort') in the presence of hops. Headspace extractions of hops with sputtered fiber were performed at 40, 60, 80, 100, 120, and 140 °C. Based on the mass spectra of the peaks and their retention indices, more than 50 compounds were identified in the 100 °C chromatogram (Table 2.2). This temperature seemed appropriate because of the boiling of wort/hops just mentioned, and also because the essential oil of hops can be obtained by steam distillation.

Table 2.1 Linear range, and limits of detection and quantitation for decanal and hexadecane using a 2.0 µm Si/SiO_2/C18 sputtered fiber.

Compounds	Linear range (µg/L)	Correlation coefficients (R^2)	LOD (µg/L)	LOQ (µg/L)
Decanal	40-1000	0.995	0.29	0.98
Hexadecane	50-1000	0.996	5.81	19.35

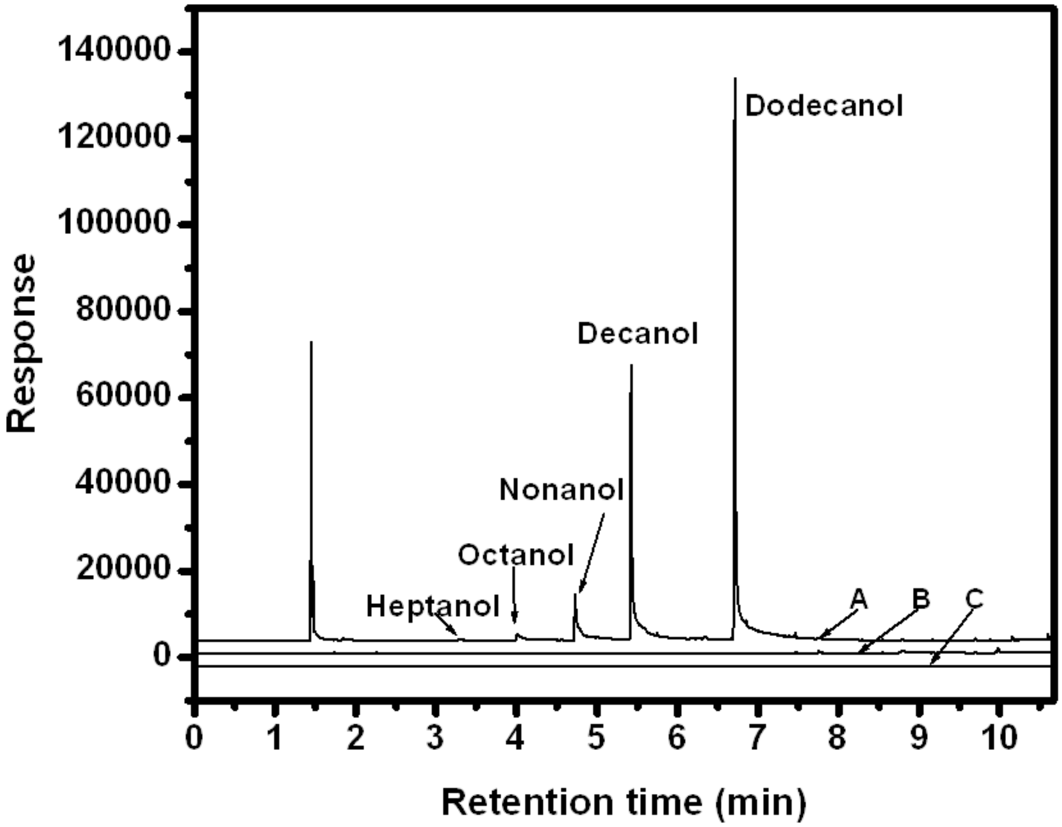

Figure 2.12 (A) Chromatogram showing headspace extraction of a mixture of alcohols (0.1 ppm) using a 2.0 µm sputtered, silanized fiber. The extraction conditions were: incubation time: 15 min, incubation agitation speed: 500 rpm, extraction time: 5 min, extraction temperature: 40 °C, desorption temperature: 280 °C, desorption time: 1 min, sample volume: 5 mL. Chromatogram (B) was obtained by desorption of the fiber for 1 min immediately after the extraction/analysis of the alcohol mixture (0.1 ppm). Chromatogram (C) is the response from the instrument with no injection with the fiber.

Table 2.2 Compounds identified in the SPME-GC-MS chromatogram of hops, including their names, retention times, peak areas, area %, and % similarities.

Compound Name	Retention Time	Peak Area	Area %	Similarity (%)
Isobutyl isobutyrate	6.10	2762794	0.87	94
β-pinene	7.75	4078253	1.29	95
Myrcene	7.97	80998734	25.64	95
butyl 2-methyl butyrate	8.22	495534	0.16	92
Isopentyl isobutyrate	8.46	1233155	0.39	92
Isopentyl butyrate	8.55	9945904	3.15	89
Methyl heptanoate	8.78	1637642	0.52	94
β-Citronellene	8.89	3027269	0.96	83
Limonene	9.04	952063	0.3	96
Pentyl butyrate	9.45	650182	0.21	95
4-methyl dec-3-en-5-ol	9.77	948308	0.3	85
Methyl octanoate	10.50	1958902	0.62	90
Linalool	10.95	5289347	1.67	92
Methyl nonanoate	11.54	1410553	0.45	92
Hexyl butyrate	12.18	1340732	0.42	94
Methyl octyl ketone	12.47	658322	0.21	93
Methyl decanoate	13.34	1801226	0.57	89
Decyl methyl ketone	13.48	1221075	0.39	91
Pinacol	14.53	2522074	0.8	89
Heptyl butyrate	14.93	638290	0.2	94
Undecan-2-one	15.28	893473	0.28	92
trans-acetate non-2-en-1-yl	15.84	972792	0.31	88
Methyl tetradecanoate	16.09	630568	0.2	89
2-Undecanone	16.28	4709221	1.49	94
Methyl non-3-enoate	16.68	7255931	2.3	88
Ipsdienol	16.82	3505101	1.11	81
Methyl ester geranic acid	17.07	806751	0.26	95
Decyl methyl ketone	17.99	636875	0.2	94
Ylangene	18.49	1214612	0.38	92
α-Cubebene	18.66	3701754	1.17	94
Isocaryophyllene	19.88	25308285	8.01	95
β-Cubebene	20.09	2847727	0.9	96
9-epi-(E)-caryophyllene	20.34	835917	0.26	94
Copaborneol	20.64	1321800	0.42	89
α-Humulene	20.84	52515838	16.63	96
γ-Muurolene	21.20	8200563	2.6	96
α-Muurolene	21.31	1002135	0.32	92

α-cis-bergamotene	21.40	929479	0.29	90
2-Tridecanone	21.52	3135114	0.99	94
α-Guaiene	21.61	5136774	1.63	92
α-Amorphene	21.78	6930774	2.19	91
Santolinatriene	21.90	1176046	0.37	87
γ-Cadinene	22.16	6130762	1.94	95
δ-Cadinene	22.26	7894026	2.5	96
trans-calamenene	22.36	2976736	0.94	95
Naphthalene	22.62	755741	0.24	95
α-Cadinene	22.72	2425419	0.77	96
Selina-3,7(11)-diene	22.89	1707510	0.54	93
Tetradec-(9E)-en-1-yl acetate	23.34	754325	0.24	89
2-pentyl-cyclopent-2-en-1-one	23.70	750359	0.24	83
Caryophyllene oxide	23.92	3327829	1.05	93
Camphene	24.30	2984147	0.94	89
cis-limonene oxide	24.58	10108877	3.2	84
cis-para-mentha-1(7),8-dien-2-ol	25.10	6023416	1.91	89
1,2,3,4,4a,7,8,8a-octahydro-, 4-isopropyl-, 1,6-dimethyl-naphth-1-ol	25.23	1611854	0.51	91
Tetradeca-(9Z,11E)-dienyl acetate	25.43	3764928	1.19	87
Methyl linolenate	25.55	1059178	0.34	88
Hexadec-(11Z)-en-1-yl acetate	25.64	4029984	1.28	90
Phytone	26.22	1787007	0.57	89

2.5 Conclusions

I have described a novel method for preparing nanoporous SPME coatings via the sputtering of silicon. The thickness of the coatings was controlled by varying the sputtering time. Sputtered silicon atoms have relatively short mean free paths under deposition conditions, and porous, columnar structures are obtained. Sputtered silicon structures on silica fibers were treated with piranha solution to introduce silanol groups onto their surfaces. The resulting surfaces were silanized with a C18 silane. The attachment of the C18 silane was confirmed by XPS and wetting on model, planar surfaces. The sputtered silicon coatings passed the Scotch tape adhesion test. Extraction time and temperature profiles were determined. The 2.0 µm sputtered, silanized fiber outperformed a commercial PDMS fiber for almost all of the compounds tested. This approach appears to overcome the drawbacks associated with many fibers that are listed above. That is, groups of fibers could be simultaneously sputtered, which should reduce cost. The coating is shown to be robust. It survives rather high temperatures, and inorganic materials, e.g., Si or SiO_2, do not swell in organic solvents. The fiber extracts a wide range of compounds. There is no carryover between runs. The coating is not lost during use – it has a rather long lifetime. Analysis of a real world sample suggests that a large number of compounds can be extracted and analyzed with these fibers.

2.6 References

1. Arthur, C. L.; Pawliszyn, J., *Anal. Chem.* **1990**, 62 (19), 2145-2148.
2. Pawliszyn, J. *J. Chromatogr. Sci.* **2000,** *38* (7), 270-278.
3. J. Pawliszyn., *Solid Phase Microextraction. Theory and Practice*; Wiley: New York, 1997.
4. Górecki, T.; Yu, X.; Pawliszyn, J. *Analyst* **1999,** *124* (5), 643-649.

5. Azenha, M. A.; Nogueira, P. J.; Silva, A. F., *Anal. Chem.* **2006**, 78 (6), 2071-2074.

6. Zhang, Z. M.; Wang, Q. T.; Li, G. K., *Anal. Chim. Acta.* **2012,** 727, 13-19.

7. Ji, L.; Li, H. X.; Zhao, F.; Chen, J. M.; Zhou, H. D. *Key Eng. Mater.* **2003,** *373-374*, 151-154.

8. Liu, H.; Ji, L.; Li, J.; Liu, S.; Liu, X.; Jiang, S. *J. Chromatogr. A* **2011,** *1218* (20), 2835-2840.

9. Harris, K. D.; Brett, M. J.; Smy, T. J.; Backhouse, C. *J. Electrochem. Soc.* **2000,** *147* (5), 2002-2006.

10. Wu, A. T.; Brett, M. J. *Sensor Mater.* **2001,** *13* (7), 399-431.

11. Setkova, L.; Risticevic, S.; Pawliszyn, J., *J. Chromatogr. A* **2007**, 1147 (2), 224-240.

12. Saini, G.; Jensen, D. S.; Wiest, L. A.; Vail, M. A.; Dadson, A.; Lee, M. L.; Shutthanandan, V.; Linford, M. R., *Anal. Chem.* **2010**, 82 (11), 4448-4456.

13. Saini, G.; Yang, L.; Lee, M. L.; Dadson, A.; Vail, M. A.; Linford, M. R., *Anal. Chem.* **2008**, 80 (16), 6253-6259.

14. Jenkins, A.; Hu, J.; Wang, Y.; Schiller, S.; Foerch, R.; Knoll, W. *Langmuir* **2000**, 16 (16), 6381-6384 (2000).

15. Bertin, A.; Schlaad, H. *Chem. Mater.* 2009, 21 (24), 5698-5700.

16. Gupta, V.; Madaan, N.; Jensen, D. S.; Kunzler, S. C.; Linford, M. R. *Langmuir* **2013,** *29* (11), 3604-3609.

17. Xu, L.; Feng, J.; Liang, X.; Li, J.; Jiang, S. *J. Sep. Sci.* **2012**, 35 (12), 1531-1537.

18. Gholivand, M. B.; Shamsipur, M.; Shamizadeh, M.; Moradian, R.; Astinchap, B. *Anal. Chim. Acta* **2014**, 822, 30-36.

19. Thornton, J. A. *J. Vac. Sci. Technol. A* **1986**, 4 (6), 3059-3065.

20. Jensen, D. S.; Kanyal, S. S.; Madaan, N.; Hancock, J. M.; Dadson, A. E.; Vail, M. A.; Vanfleet, R. ; Shutthanandan, V.; Zhu, Z.; Engelhard, M. H.; Linford, M. R. *Surf. Interface Anal.* **2013**, 45 (8), 1273-1282.

21. Jiang, G.; Rivera, F.; Kanyal, S. S.; Davis, R. C.; Vanfleet, R.; Lunt, B. M.; Shutthanandan, V.; Linford, M. R. *Optical Engineering* **2011**, 50 (1), 015201-015210.

22. Wasserman, S. R.; Tao, Y. T.; Whitesides, G. M. *Langmuir* **1989***,* 5 (4), 1074-1087.

23. Linford, M. R.; Fenter, P.; Eisenberger, P. M.; Chidsey, C. E. *J. Am. Chem. Soc.* **1995**, 117 (11), 3145-3155.

24. Li, X.-M.; Reinhoudt, D.; Crego-Calama, M. *Chem. Soc. Rev.* **2007**, 36 (8), 1350-1368.

25. Gupta, V.; Ganegoda, H.; Engelhard, M. H.; Terry, J.; Linford, M. R. *J. Chem. Educ.* **2013**, 91 (2), 232-238.

26. Jensen, D. S.; Kanyal, S. S.; Madaan, N.; Vail, M. A.; Dadson, A. E.; Engelhard, M. H.; Linford, M. R. *Surf. Sci. Spectra* **2013,** *20* (1), 36-42.

27. Husseini, G. A.; Peacock, J.; Sathyapalan, A.; Zilch, L. W.; Asplund, M. C.; Sevy, E. T.; Linford, M. R. *Langmuir* **2003,** *19* (12), 5169-5171.

28. Quast, A. D.; Zhang, F.; Linford, M. R.; Patterson, J. E. *Appl. Spectrosc.* **2011**, 65 (6), 634-641.

29. Buszewski, B.; Nondek, L.; Jurášek, A.; Berek, D. *Chromatographia* **1987**, 23 (6), 442-446.

30. Ji, J.; Liu, H.; Chen, J.; Zeng, J.; Huang, J.; Gao, L.; Wang, Y.; Chen, X. *J. Chromatogr. A* **2012,** *1246*, 22-27.

31. Eri, S.; Khoo, B. K.; Lech, J.; Hartman, T. G. *J. Agric. Food. Chem.* **2000,** 48 (4), 1140-1149.

Chapter 3 Superhydrophobic Surfaces with Very Low Hysteresis Prepared by Aggregation of Silica Nanoparticles During In Situ Urea-Formaldehyde Polymerization*

3.1 Abstract

I present a new method for the preparation of superhydrophobic materials by in situ aggregation of silica nanoparticles on a surface during a urea-formaldehyde (UF) polymerization. This is a one-step process in which a two-tier topography is obtained. The polymerization is carried out for 30, 60, 120, 180, and 240 min on silicon shards. Silicon surfaces are sintered to remove the polymer. SEM and AFM show both an increase in the area covered by the nanoparticles and their aggregation with increasing polymerization time. Chemical vapor deposition of a fluorinated silane in the presence of a basic catalyst gives these surfaces hydrophobicity. Deposition of this low surface energy silane is confirmed by the F 1s signal in XPS. The surfaces show advancing water contact angles in excess of 160° with very low hysteresis (<7°) after 120 min and 60 min polymerization times for 7 nm and 14 nm silica, respectively. Depositions are successfully demonstrated on glass substrates after they are primed with a UF polymer layer. Superhydrophobic surfaces can also be prepared on unsintered substrates.

3.2 Introduction

Nature provides numerous examples of superhydrophobic surfaces (SHS) including the lotus leaf,[1-14] duck feathers,[4] butterfly wings,[1, 4] rice leaves,[2] and the legs of water striders.[3, 9] These surfaces/materials have water contact angle greater than 150° and very low sliding angles –

---

*This chapter has been reproduced with permission from (Anubhav Diwan, David S. Jensen, Vipul Gupta, Brian I. Johnson, Delwyn Evans, Clive Telford, and Matthew R. Linford), *J. Nanosci. Nanotechnol.* **2015**, 15(12), 10022-10036. Copyright 2015 American Scientific Publishers the angle at which a droplet of water of a given mass slides down an inclined surface.[15] The combination of a two-tier topography and a hydrophobic coating results in the Lotus effect.[1-7] Accordingly, the main requirements for an SHS material are surface roughness and a low surface energy.[1-4, 7, 9-11, 13, 16-17] Preparations of SHS have been broadly classified as (i) preparation of a rough surface followed by deposition of a low surface energy material and (ii) the use of a low surface energy material that is roughened.[1-2, 4, 10, 16] In this work I take the first of these two approaches. SHS have been employed in numerous applications such as self-cleaning surfaces,[1-4, 8, 10, 16-17] antibiofouling paints,[3-4] anti-icing coatings on windows and antennas,[2-3, 7] waterproof clothes,[1, 3-4, 13] anti-reflective coatings for optical windows,[4] for fluidic drag reduction,[4] and for separation of oil and water.[2, 4]

Herein I demonstrate for the first time the formation of SHS via the polymerization of urea and formaldehyde in the presence of nanosilica and a planar substrate. This work differs in a fundamental way from most of the studies in this area that have used silicon nanoparticles in that these studies tend to use either a standard or a modified Stöber process to prepare their superhydrophobic surfaces. The preparation reported herein results in the aggregation of silica nanoparticles and a textured surface, where this aggregation and surface roughness increase with increasing polymerization time. After hydrophobization with a silane adsorbate, the resulting surfaces show extremely high advancing and receding water contact angles and very low hysteresis. Chemical vapor deposition of silanes,[18-20] which is employed here, as opposed to their liquid phase deposition, which is more common,[21-23] is an important and reproducible approach for depositing these useful reagents.

3.3 Experimental

3.3.1 Reagents and Materials

Materials: Glass microscope slides (VWR, CA), and silicon wafers (Montco Silicon). Reagents: urea (prilled, ACS, EMD chemicals), nitric acid (Macron chemicals), formaldehyde (ACS, Fisher scientific), ammonium hydroxide (ACS, EMD chemicals), (tridecafluoro-1,1,2,2-tetrahydrooctyl)-trimethoxysilane (F-13 silane) (Gelest, Morrisville, PA), and high purity water (18 MΩ resistance from a Milli-Q Water System, Millipore, Billerica, MA). The 7 nm and 14 nm fumed silica powders were obtained from Sigma-Aldrich (St. Louis, MO).

3.3.2 Preparation of Rough Surfaces on Native Oxide-Terminated Silicon

Slurries of 7 nm and 14 nm silica powder were prepared as 5 wt. % solutions in high purity water by dissolving 1 g of nanosilica in 19 g of water in a round bottom flask. The mixtures were sonicated for 120 s, resulting in clear solutions. 15 g of this solution was removed, added to 20 g of water, and stirred for 10 min. Next, urea (0.2169 g) was dissolved in 10 g of water and added to the above nanosilica solution. Nitric acid (0.2875 g) was then added, and after 60 s polymerization was initiated by the addition of formaldehyde (0.381 g). The urea, formaldehyde, and nitric acid were added in a mole ratio of 1:1.32:1.75.[24] The final urea-formaldehyde-silica slurry was divided into five volumes of equal weight and poured over silicon shards lying at the bottom of petri dishes. Prior to any deposition, the silicon shards (ca. 1.5 x 1.5 cm) were cleaned with an air plasma for 60 s in a Harrick plasma cleaner (PDC-32 G, Harrick Plasma, Ithaca, NY). Incubations in these solutions were for 30, 60, 120, 180, and 240 min, after which individual shards were rinsed with water to remove unbound polymer and silica. The surfaces were then dried at room temperature or heated at 600 °C for 3 h or at 900 °C for 1 h.

3.3.3 Coating Glass Substrates

Glass, of course, is a complex, multicomponent mixture. To coat glass substrates with a superhydrophobic layer, a sticking layer of UF polymer was first deposited for 30, 60, 120, 180, or 240 min. This polymer layer was created in the same way as the UF-nanosilica layer, except that no nanosilica was present. After deposition of the polymer film, the surfaces were rinsed with high purity water. A UF-nanosilica layer was then deposited as described above with an incubation time of either 120 or 180 min. These surfaces were coated directly with the fluoro silane without sintering.

3.3.4 Chemical Vapor Deposition of the Fluorosilane

A home-built chemical vapor deposition (CVD) oven (see Figure 3.1) was used for the base-catalyzed deposition of the hydrophobic silane (F-13). Substrates were placed in this oven, the pressure was reduced to 1 Torr, and the temperature was raised to 85°C. The valve to the pump was then closed before injection of 0.3 mL of concentrated, aqueous ammonium hydroxide (NH_4OH). The resulting vapors of ammonia were allowed to remain in the chamber for 10 min. Without evacuating the chamber to remove the ammonium hydroxide, 0.25 mL of the F-13 silane was then injected and silanization was allowed to proceed for 10 min. Finally, the chamber was evacuated and purged four times with dry nitrogen to remove unreacted reagents.

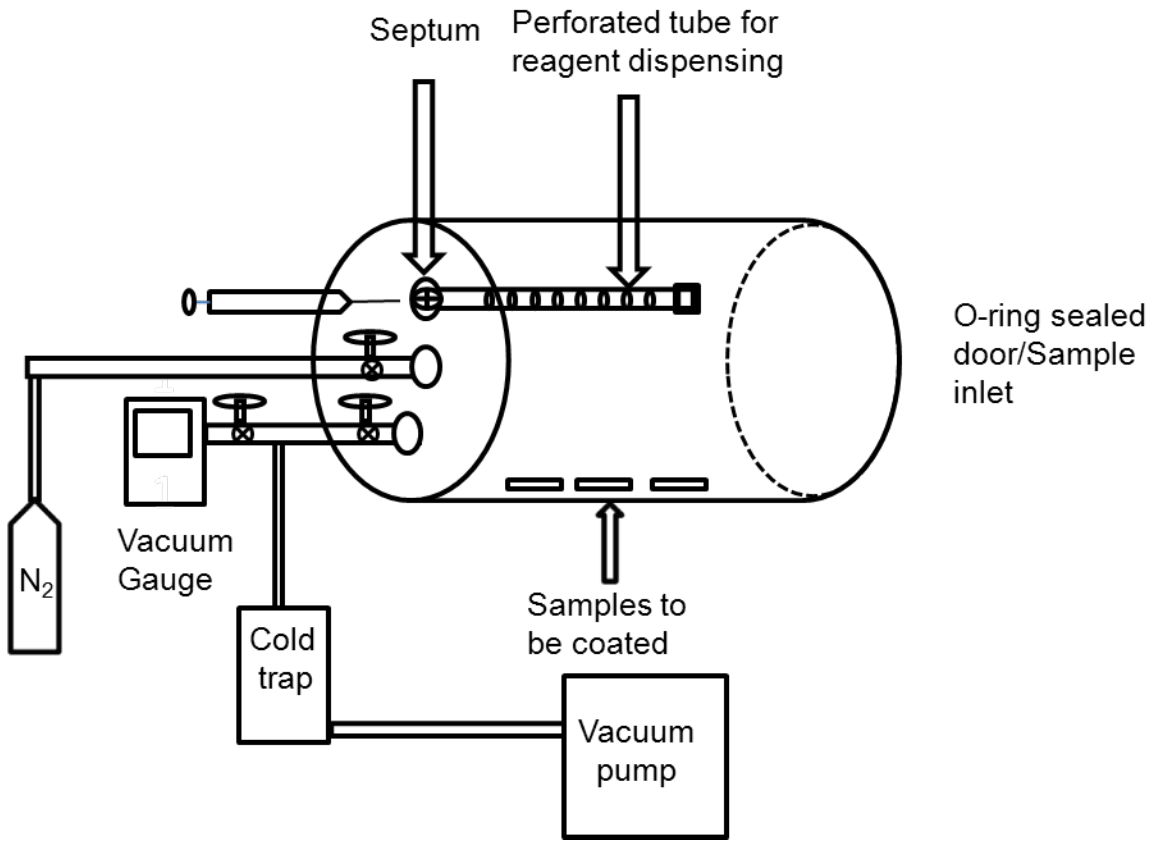

Figure 3.1 Schematic of a cylindrical (6” inner diameter x 11” length), home-built chemical vapor deposition system.

3.3.5 Surface Characterization

Water contact angles were measured with a Ramé-Hart Contact Angle Goniometer (Model 100-00, Netcong, NJ)) fitted with a manual syringe filled with Millipore water. The drop sizes for measuring static water contact angles were ca. 10 µL. X-ray photoelectron spectroscopy (XPS) measurements were performed using a Surface Science SSX-100 X-ray photoelectron spectrometer (serviced by Service Physics, Bend, OR) with a monochromatic Al K_α source, a hemispherical analyzer, and a take-off angle of 35°. Survey and narrow scans were recorded with a spot size of 800 µm x 800 µm and a resolution of 4. Peaks were referenced to the C 1s hydrocarbon signal at 284.6 eV. Atomic force microscopy (AFM) was performed in tapping mode with a Dimension 3100 AFM (Veeco, Plainview, NY) using a tip with an Al reflective coating (OTESPA, 42 N/m, 300kHz, Bruker, Madison, WI) over a 20 µm x 20 µm area. Scanning electron microscopy (SEM) was performed using a Helios NanoLab TM 600 instrument (FEI, Hillaboro, OR). Profile views of the surfaces were taken at 87° for the surfaces prepared with 7 nm silica and at 85° for the surfaces prepared with 14 nm silica. ImageJ software analysis ("Image Processing and Analysis in Java" version 1.46r obtained from nih.gov) was performed on the top-view SEM images of surfaces prepared with both sizes of silica nanoparticles.

3.4 Results and Discussion

3.4.1 Overview

In situ urea-formaldehyde polymerization in the presence of silica nanoparticles resulted in aggregation of the particles, which produced textured surfaces on planar silicon and glass substrates. The surfaces were sintered, which resulted in loss of the polymer binder. All surfaces were coated with a hydrophobic (fluorinated) silane to yield superhydrophobic materials. This general procedure resulted in SHS with water contact angles greater than 160°. Results below are for silicon substrates unless stated otherwise.

3.4.2 SEM Characterization

SEM images showed aggregates of silica particles on silicon substrates that increased in size with increasing polymerization time. The top and profile views of the surfaces prepared from the 7 nm silica (Figure 3.2) showed that after 30 and 60 min of polymerization, there were (i) relatively few papillae and (ii) the nanocarpet coverage was fairly limited, but that both increased with polymerization time. ('Papilla' means 'nipple' or 'protrusion' in Latin. Its plural is 'papillae'.) The top and profile views of the surfaces prepared with 14 nm silica are quite similar to the surfaces prepared with 7 nm silica, although the 14 nm substrates generally show greater nanocarpet coverage at a given polymerization time. A more precise comparison of the fractional area covered on these surfaces was performed via a software analysis of the images in Figure 3.2 (other images are not shown). This analysis shows an increase in the area covered on the surfaces with increasing polymerization time, where the corresponding areal coverages for the surfaces prepared with the 14 nm silica are consistently higher than those made with the 7 nm silica (see Figure 3.3a). These results help explain the faster formation of superhydrophobic surfaces from the 14 nm silica.

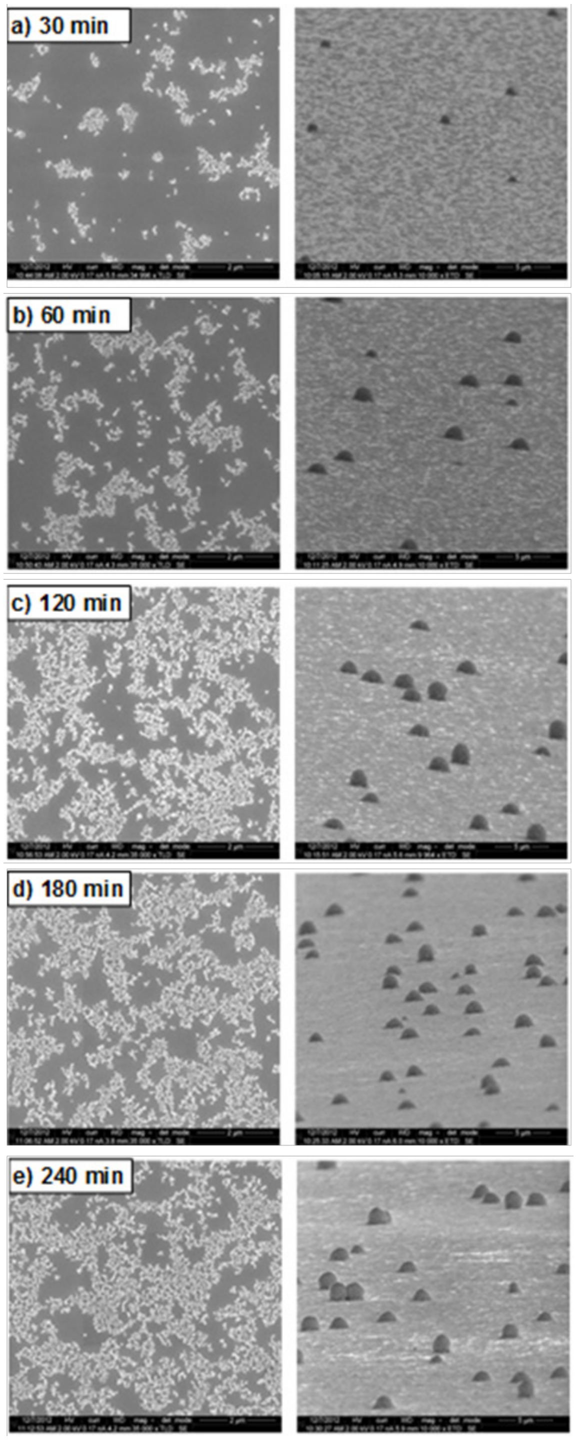

Figure 3.2 SEM top view images (left) and profile view images (right) of silicon surfaces after UF polymerization with 7 nm silicon for (a) 30, (b) 60, (c) 120, (d) 180, and (e) 240 min.

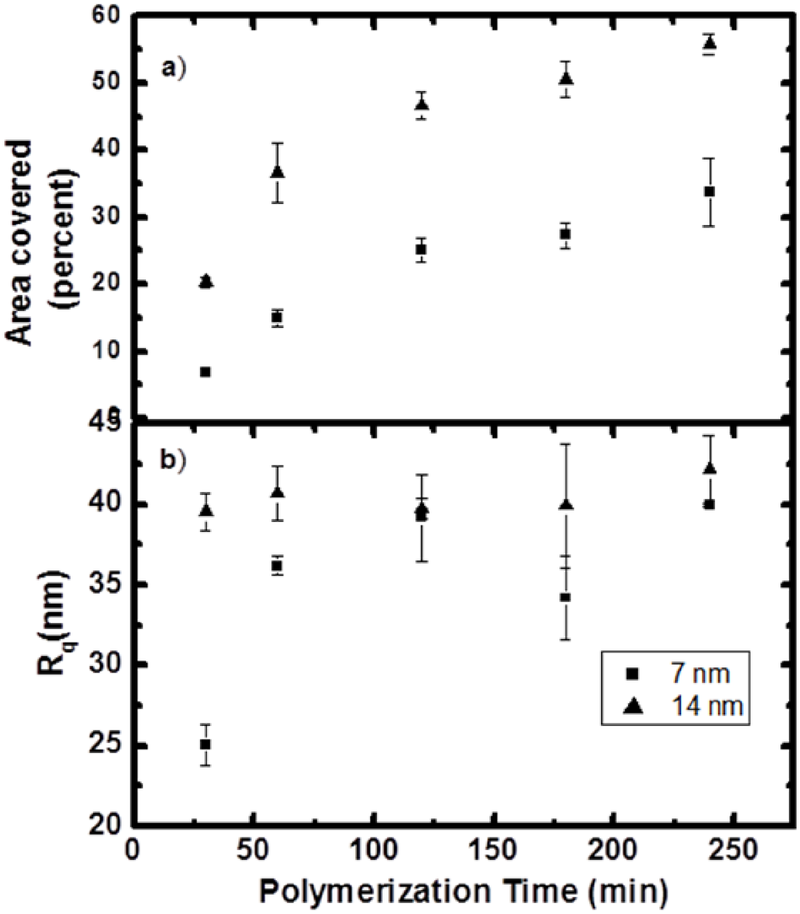

Figure 3.3 (a) Percentage of area covered vs. polymerization time from SEM top view images of surfaces prepared with 7 and 14 nm silica. (b) Roughness factor (Rq) as a function of polymerization time for surfaces prepared with 7 and 14 nm silica.

3.4.3 AFM Characterization

For AFM imaging, papillae were deliberately avoided to be able to directly compare the roughnesses of the nanocarpets of surfaces prepared at different polymerization times using different sized silica nanoparticles. For the 14 nm silica, the roughness factor R_q remains nearly constant and at a relatively high level for the 30 – 240 min polymerization times, while for the 7 nm silica the surface roughness starts at a lower level but after ca. 120 min approaches that of the 14 nm silica (see Figure 3.3b).

3.4.4 XPS Characterization of UF-Coated Silica and F-13 Coated SHS

Figure 3.4 shows XPS N 1s narrow scans at different polymerization times for silicon wafers coated only with the urea-formaldehyde polymer (no nanosilica). The N 1s signal from nitrogen is quite weak after 30 min of polymerization (not far out of the noise), but at 60 and 180 min the signal is prominent. Interestingly, I was unable to obtain any nitrogen signal by XPS from surfaces modified with urea-formaldehyde polymerizations performed in the presence of nanosilica. This suggests that nanosilica terminates the assemblies. However, the presence of the UF polymer is critical for the formation of both a silica nanocarpet and papillae as control experiments show that they *do not* form in the absence of UF polymerization.

XPS survey spectra were obtained of a UF polymer-silica composite surface before and after sintering, and also after sintering and silanization with the F-13 silane. There is a decrease in the carbon content of the sample after sintering although the C 1s signal was very small to begin with. This small carbon signal that was initially found is consistent with the absence of an N 1s signal that was observed after preparation of the superhydrophobic surfaces. After sintering, the Si 2p oxide signal at 103 eV increases in intensity. This difference does not appear to be due to a change in the coating but in the substrate. A control shard of silicon exposed to the sintering conditions of the UF polymer-silica assemblies showed an increase in oxide thickness of ca. 1.4 nm by spectroscopic ellipsometry and a substantial increase in its Si 2p oxide peak by XPS. The gas phase deposition of the F-13 silane is well confirmed by XPS, which showed a substantial F 1s and corresponding fluorine Auger signal.

3.4.5 Water contact angle measurements

Here, SEM and AFM are used to confirm the two-tier surface roughness needed for superhydrophobicity, and XPS shows that a fluorosilane can be deposited onto textured silica nanostructures. The final test for superhydrophobicity is the wetting properties of these new materials.

Figure 3.5 shows water contact angles as a function of polymerization time for SHS formation from 7 and 14 nm silica. After 120 min the surface prepared with the 7 nm silica shows superhydrophobicity. As expected from the SEM results, SHS formation proceeds even more quickly with the larger silica nanoparticles. Indeed, with the 14 nm silica, the surfaces exhibit superhydrophobicity after only 60 min of polymerization. The hysteresis (difference between the advancing and receding water contact angles) for the superhydrophobic surfaces prepared using both 7 and 14 nm silica particles is less than 7°, which is very low.

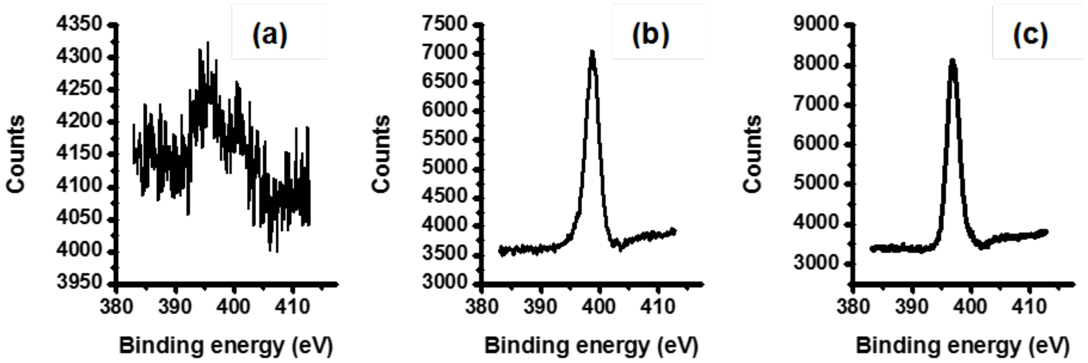

Figure 3.4 XPS N 1s narrow scans of a silicon shard exposed to a UF polymerization in the absence of nanosilica after (a) 30 min, (b) 60 min, and (c) 180 min.

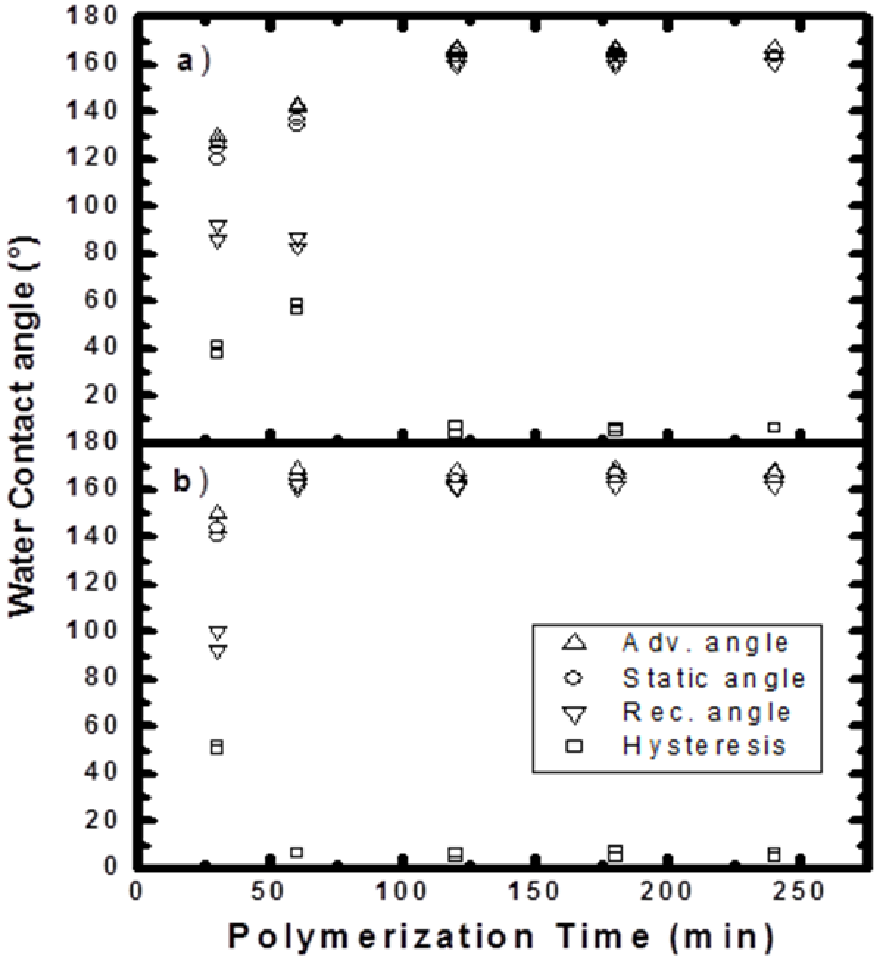

Figure 3.5 Advancing, receding, and static water contact angles, and hysteresis for sintered, silanized UF polymer-nanosilica assemblies as a function of polymerization time for (a) 7 nm silica, and (b) 14 nm silica.

3.4.6 Coating Glass Slides

Attempts were also made to deposit UF – nanosilica coatings on glass microscope slides. Unfortunately, and somewhat surprisingly, these attempts were unsuccessful. Clearly Si/SiO_2 and glass substrates have different surface chemistries, which appears to affect depositions on them. Nevertheless, deposition of a superhydrophobic layer on glass from a UF-nanosilica solution *was* possible if the substrate was first immersed for 60 – 240 min in a UF polymer solution that did not contain nanosilica – these solutions had the same compositions as for the UF-nanosilica depositions, but without the nanosilica. Superhydrophobicity was not obtained in the case of a 30 min UF polymer immersion. Similar depositions and uses of organic surface modifiers have been reported in the literature.[24] Because of the fairly low melting point of the glass slides, their UF-nanosilica coatings were not sintered. Nevertheless, these assemblies could still be coated with the F-13 silane and they became superhydrophobic after this deposition. Table 3.1 shows (i) that very high advancing and receding water contact angles could be obtained for the superhydrophobic coating on glass, as was the case for the sintered UF-nanosilica coatings on silicon, and (ii) that these coatings could be prepared from both 7 nm and 14 nm silica at both 120 min and 180 min deposition times. These results suggest that this method can be used to coat heat sensitive materials. Unsintered nanosilica assemblies on silicon also showed the same levels of superhydrophobicity after treatment with the fluorinated silane. Finally, the coatings on glass were not completely transparent – while objects could be clearly seen through them, they showed some haziness. This haziness was probably exacerbated by the fact that the substrates were coated on both sides.

Table 3.1 Formation of superhydrophobic surfaces on glass substrates that were pre-coated with a UF polymer. This coating was followed by UF – nanosilica (7 nm and 14 nm) deposition for 120 or 180 min.

Dep. time of UF pre-coating (min)	**UF – 7 nm silica (120 min)**				**UF – 7 nm silica (180 min)**				**UF – 14 nm silica (120 min)**				**UF – 14 nm silica (180 min)**			
	SHS	WCA (°)			SHS	WCA (°)			SHS	WCA (°)			SHS	WCA (°)		
		Adv.	Static	Rec.		Adv.	Static	Rec.		Adv.	Static	Rec.		Adv.	Static	Rec.
30	×	118	115	89	×	122	117	92	×	116	112	92	×	119	116	88
60	✓	168	166	164	✓	167	164	162	✓	169	166	162	✓	168	164	162
120	✓	166	164	163	✓	167	165	163	✓	166	164	163	✓	168	165	162
180	✓	167	164	162	✓	168	165	163	✓	168	165	164	✓	166	163	161
240	✓	167	165	164	✓	170	168	164	✓	168	166	164	✓	168	165	163

3.4.7 *Testing of Surfaces*

Unsintered and sintered surfaces were evaluated using the Scotch tape test, which is a stringent test that consists of pressing a fresh piece of Scotch tape onto a surface and manually removing it. The surfaces were not able to withstand this test. However, the surface sintered at 900 °C showed better resistance to this test in comparison to either a unsintered material or a surface sintered at 600 °C, both of which had similar properties. Obviously, one would expect greater robustness at even higher sintering temperatures.

3.5 Conclusions

I have demonstrated a new approach for the preparation of superhydrophobic coatings on silicon and glass via urea-formaldehyde polymerization in the presence of nanosilica followed by chemical vapor deposition of an F-13 silane. Water contact angles greater than 160° and with very low hysteresis are obtained. Increasing polymerization times results in silica aggregates that show a two-tier topography. The surfaces showed increased mechanical robustness with sintering. Unsintered, silanized surfaces also exhibited high levels of superhydrophobicity.

3.6 References

1. Ma, M.; Hill, R. M. *Curr. Opin. Colloid Interface Sci.* **2006,** *11* (4), 193-202.
2. Feng, L.; Li, S.; Li, Y.; Li, H.; Zhang, L.; Zhai, J.; Song, Y.; Liu, B.; Jiang, L.; Zhu, D. *Adv. Mater.* **2002,** *14* (24), 1857-1860.
3. Li, X.-M.; Reinhoudt, D.; Crego-Calama, M. *Chem. Soc. Rev.* **2007,** *36* (8), 1350-1368.
4. Zhang, X.; Shi, F.; Niu, J.; Jiang, Y.; Wang, Z. *J. Mater. Chem.* **2008,** *18* (6), 621-633.
5. Gao, L.; McCarthy, T. J. *Langmuir* **2006,** *22* (7), 2966-2967.
6. Barthlott, W.; Neinhuis, C. *Planta* **1997,** *202* (1), 1-8.

7. Roach, P.; Shirtcliffe, N. J.; Newton, M. I. *Soft Matter* **2007,** *4* (2), 224-240.

8. Wang, S.; Jiang, L. *Adv. Mater.* **2007,** *19* (21), 3423-3424.

9. Ling, X. Y.; Phang, I. Y.; Vancso, G. J.; Huskens, J.; Reinhoudt, D. N. *Langmuir* **2009,** *25* (5), 3260-3263.

10. Bravo, J.; Zhai, L.; Wu, Z.; Cohen, R. E.; Rubner, M. F. *Langmuir* **2007,** *23* (13), 7293-7298.

11. Soeno, T.; Inokuchi, K.; Shiratori, S. *Appl. Surf. Sci.* **2004,** *237* (1), 539-543.

12. Hsieh, C.-T.; Wu, F.-L.; Yang, S.-Y. *Surf. Coat. Technol.* **2008,** *202* (24), 6103-6108.

13. Xue, C.-H.; Jia, S.-T.; Zhang, J.; Tian, L.-Q. *Thin Solid Films* **2009,** *517* (16), 4593-4598.

14. Xiu, Y.; Zhu, L.; Hess, D. W.; Wong, C. *Langmuir* **2006,** *22* (23), 9676-9681.

15. Miwa, M.; Nakajima, A.; Fujishima, A.; Hashimoto, K.; Watanabe, T. *Langmuir* **2000,** *16* (13), 5754-5760.

16. Zhai, L.; Cebeci, F. C.; Cohen, R. E.; Rubner, M. F. *Nano Lett.* **2004,** *4* (7), 1349-1353.

17. Shang, H.; Wang, Y.; Limmer, S.; Chou, T.; Takahashi, K.; Cao, G. *Thin Solid Films* **2005,** *472* (1), 37-43.

18. Gupta, V.; Madaan, N.; Jensen, D. S.; Kunzler, S. C.; Linford, M. R. *Langmuir* **2013,** *29* (11), 3604-3609.

19. Saini, G.; Sautter, K.; Hild, F. E.; Pauley, J.; Linford, M. R. *J. Vac. Sci. Technol., A* **2008,** *26* (5), 1224-1234.

20. Zhang, F.; Sautter, K.; Larsen, A. M.; Findley, D. A.; Davis, R. C.; Samha, H.; Linford, M. R. *Langmuir* **2010,** *26* (18), 14648-14654.

21. Balachander, N.; Sukenik, C. N. *Langmuir* **1990,** *6* (11), 1621-1627.

22. Husseini, G. A.; Peacock, J.; Sathyapalan, A.; Zilch, L. W.; Asplund, M. C.; Sevy, E. T.; Linford, M. R. *Langmuir* **2003,** *19* (12), 5169-5171.

23. Maoz, R.; Sagiv, J. *J. Colloid Interface Sci.* **1984,** *100* (2), 465-496.

24. Chen, W.; Wei, T.-c., Superficially Porous Particles And Methods Of Making And Using Same. US Patent 20,100,206,797, August 19, 2010.

Chapter 4 Layer-By–Layer Deposition of Nitrilotris(methylene)triphosphonic acid and Zr(IV). An XPS, ToF-SIMS, Ellipsometry, and AFM study*

4.1 Abstract

Layer-by-layer assemblies consisting of alternating layers of nitrilotris(methylene)triphosphonic acid (NTMP), a polyfunctional corrosion inhibitor, and zirconium(IV) were prepared on alumina. In particular, a nine layer (NTMP/Zr(IV))$_4$NTMP assembly could be constructed at room temperature, which showed a steady increase in film thickness throughout its growth by spectroscopic ellipsometry (SE) up to a final thickness of 1.79 ± 0.04 nm. At higher temperature (70 °C) even a two layer NTMP/Zr(IV) assembly could not be prepared because of etching of the alumina substrate by the heated Zr(IV) solution. XPS characterization of the LBL assembly exhibited small saw tooth patterns in the nitrogen, phosphorus, and zirconium signals, where the modest increases and decreases in these signals corresponded to the expected deposition and perhaps removal of NTMP and Zr(IV). ToF-SIMS confirmed the attachment of the NTMP molecule to the surface through PO^-, PO_2^-, PO_3^-, and CN^- signals. Increasing attenuation of the Al signal from the substrate after deposition of each layer was observed by both XPS and ToF-SIMS. Essentially complete etching of the alumina by the heated Zr(IV) solution was confirmed by SE, XPS, and ToF-SIMS. AFM revealed that all the films were smooth with R_q roughness of less than 0.5 nm.

---

*This chapter has been reproduced with permission from (Anubhav Diwan, Bhupinder Singh, Christopher J. Hurley, and Matthew R. Linford), *Surf. Interface Anal.* **2016**, 48, 105-110. Copyright 2015 John Wiley and Sons, Ltd.

4.2 Introduction

Some of the most studied self-assembled monolayers (SAM) components include the silanes, which effectively bind to silica surfaces,[1-2] the alkanethiols, which form monolayers on gold,[3-5] alkanes and alkenes, which bind to hydrogen-terminated and scribed (bare) silicon,[6-10] and the phosphonic acids (PAs), which adhere well to metal oxides,[5] including alumina,[4-5, 11-17] iron oxide,[16, 18] tantalum oxide,[3, 17] silicon oxide,[19-20] copper oxide,[16] titania,[17, 19, 21-23] zirconia,[17, 19] niobium oxide,[17] and indium tin oxide.[24] In 1987, Mallouk and co-workers[25-26] demonstrated a sequential layer-by-layer (LBL) deposition of a biphosphonic acid with a long hydrocarbon chain and zirconium on silicon and gold. The thickness increase after deposition of a single bilayer (the bisphosphonate followed by zirconium) was 17 Å.[25-26] Subsequently, a series of studies have reported the LBL preparation of multi-layer films from various long chain phosphonates and zirconium.[27-28]

Amino phosphonates have been employed for years in various industries as corrosion inhibitors,[11] where nitrilotris(methylene)triphosphonic acid (NTMP) is an important example of one of these species. In particular, NTMP has been used as a corrosion inhibitor in water plants,[12, 29] to prevent staining of painted or treated wood surfaces by tannins,[30] to improve the durability of adhesively bonded aluminum structures,[14] and as a cement hydration inhibitor.[31] It has also limited the corrosion of alumina/aluminum optical devices without affecting the optical properties of these devices.[13]

Herein, I describe the preparation of LBL[32-35] films of NTMP and zirconium at two different temperatures (room temperature and 70°C) on e-beam deposited alumina (ca. 22 nm) on Si/SiO_2 substrates.[36-37] The films were characterized after deposition of each layer by a suite of techniques,[38-39] including ellipsometry, X-ray photoelectron spectroscopy (XPS), time-of-flight secondary ion mass spectrometry (TOF-SIMS) and atomic force microscopy (AFM).

4.3 Experimental

4.3.1 Materials

NTMP (50 wt. % in water) and zirconium(IV) oxychloride octahydrate were obtained from Sigma-Aldrich (St. Louis, MO). High purity water (18 MΩ resistance from a Milli-Q Water System, Millipore, Billerica, MA) was used to prepare these solutions.

4.3.2 Procedure

Alumina was deposited by e-beam evaporation in a system from Denton (Moorestown, NJ) onto silicon shards. Prior to any deposition, alumina substrates were cleaned by air plasma for 60 s in a commercial plasma cleaner (PDC-32 G, Harrick Plasma, Ithaca, NY). For the multi-layer coatings, two different solutions were prepared. The NTMP solution was made by dissolving 0.165 mL of the NTMP solution in 500 mL of high purity water. The Zr(IV) solution consisted of 241.5 mg of $ZrOCl_4$ in 150 mL of high purity water.

a) Room temperature deposition

Substrates were dipped in the NTMP solution at room temperature for 10 min, rinsed with water, dried with a jet of nitrogen, and then dipped in the Zr(IV) solution for 10 min, rinsed with water, and dried with a jet of nitrogen. This process was repeated multiple times to get the desired number of depositions. The number of layers deposited at room temperature varied from 1 – 9.

b) Higher temperature deposition

The same process as that at room temperature was performed, with the exception that the NTMP and Zr(IV) solutions were at 70 °C.

4.3.3 Instrumentation

XPS was performed with an SSX-100 instrument (Surface Science, serviced by Service Physics, Bend, OR). Monochromatic Al Ka X-rays were the excitation source, the take off angle was 35°, a hemispherical analyzer was used, and the C1s signal at 284.6 eV from adventitious carbon was the internal reference. Sample charging was controlled with an electron flood gun. Survey scans were recorded with spot size: 800 x 800 μm^2, resolution: 4 (nominal pass energy 150 eV), number of scans: 20, and step size: 1 eV. For high resolution scanning, the following parameters were used: window width: 30 eV, eV/step: 0.065 eV, resolution: 4 (nominal pass energy: 150 eV), number of scans: 80, and spot size: 800 x 800 μm^2. Surface morphologies were probed via tapping mode AFM (Dimension 3100, Digital Instruments, Tonawanda, NY). Tips (Bruker, MA, USA) were tetrahedral, made of silicon, and contained an aluminum reflective coating. SE was performed with a variable angle spectroscopic ellipsometer (M-2000D, J. A. Woollam, Lincoln, NE). Data were acquired at 75° and were fitted using the instrument software (WVASE 32, Version 3.632). The optical constants for the alumina were modeled using the Cauchy dispersion relationship from 300 – 1000 nm. The optical constants for the native oxide on the silicon wafer were taken from the 'SiO_2_jaw' file in the J.A. Woollam instrument software. Static time-of-flight secondary ion mass spectrometry (ToF-SIMS) was performed with a TOF-SIMS IV instrument (ION-TOF GmbH, Münster, Germany) with a Cs^+ source over a 500 x 500 μm^2 sample area. An electron flood gun was used for charge compensation. For each sample, both positive ion and negative ion spectra were collected.

4.4 Results and Discussion

4.4.1 Room temperature deposition of NTMP and Zr(IV)

4.4.1.1 Ellipsometry

Thin films of alumina were deposited onto Si/SiO_2 substrates. The optical constants of these alumina layers from 300 – 1000 nm were well modeled using the Cauchy dispersion relationship.[40] The resulting values for the index of refraction for alumina, e.g., $n = 1.59$ at $\lambda = 500$ nm, were lower than the values of a reference sample of alumina, e.g., $n = 1.77$ at $\lambda = 500$ nm.[41] It can be concluded from this analysis that these films are under dense.

The thicknesses of the NTMP/Zr(IV) coatings after each step in the LBL deposition were also monitored by SE. The first layer of NTMP on alumina was 0.2 nm thick. The subsequent depositions of Zr(IV) and NTMP for a total of 9 layers showed a steady increase in the film thickness (Figure 4.1). The total thickness of the NTMP/Zr(IV) film after deposition of 5 layers of NTMP and 4 layers of zirconium was 1.79 ± 0.04 nm. The ability to control the thickness of an ultrathin coating at this level could be useful for depositing a corrosion resistant layer on an optical device, such as a polarizer, where an ultrathin coating should only interfere minimally with the performance of the device.[13]

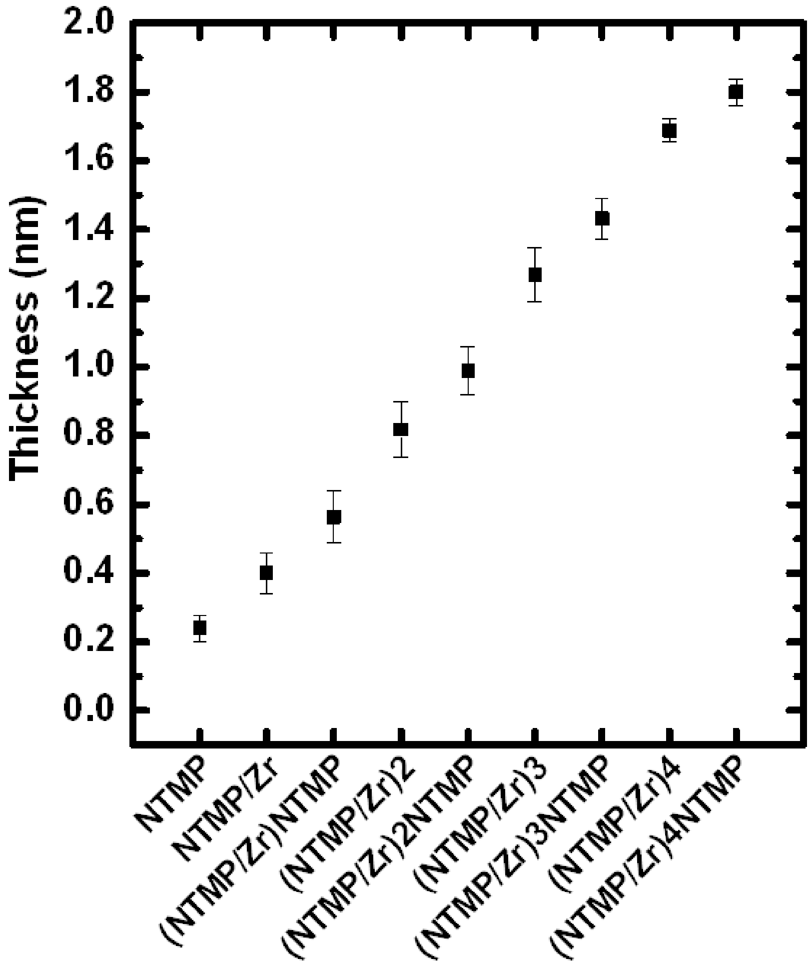

Figure 4.1 Film thicknesses after sequential LBL deposition of NTMP and Zr(IV), as measured by SE.

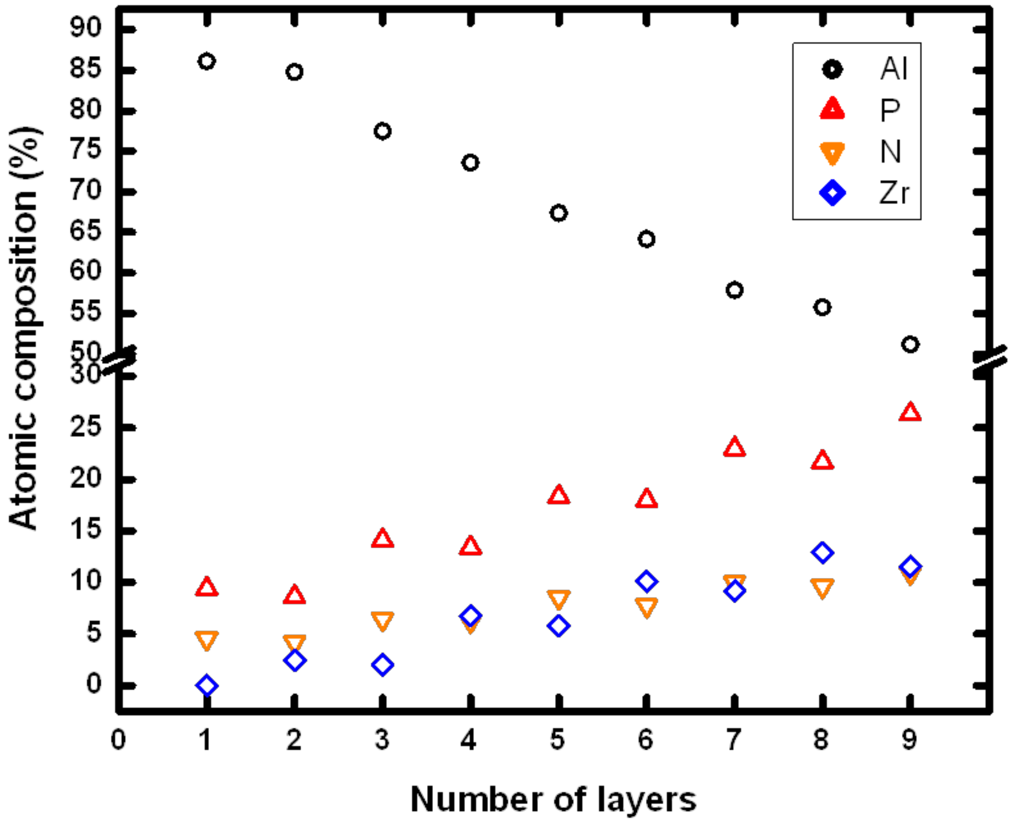

Figure 4.2 Atomic percentages as determined by XPS after sequential LBL deposition of NTMP and Zr(IV). NTMP was the last material deposited in layers 1, 3, 5, 7, and 9, and Zr(IV) was the last material deposited in layers 2, 4, 6, and 8.

4.4.1.2 X-ray photoelectron spectroscopy

SE showed an increase in thickness of the NTMP/Zr(IV) films after each deposition. Accordingly, these increasingly thick films were expected to show changes to their Al (substrate), N, P, and Zr XPS signals. XPS of the bare alumina substrate revealed aluminum, oxygen, carbon, and a small amount of nitrogen. These latter two signals were attributed to surface contamination. With the deposition of the initial layer of NTMP, phosphorus and nitrogen were detected, which are present in the NTMP molecule, and which confirms its deposition (vide infra). No zirconium was detected in the first layer. However, upon exposure of the surface to Zr(IV), slight decreases in the P 2p and N 1s signals were observed, and a Zr $3p_{3/2}$ peak is observed confirming its attachment. Similar behavior is observed for this system in the deposition of each subsequent NTMP and Zr layer (see Figure 4.2). In particular, each deposition of NTMP results in increases in the P 2p and N 1s signals and a small decrease in the Zr $3p_{3/2}$ peak, and each deposition of Zr(IV) results in an increase in the Zr $3p_{3/2}$ signal and concomitantly small decreases in the P 2p and N 1s signals. All of these signals show, to a small degree, saw tooth like behavior. The decrease in the Zr signal with deposition of NTMP and the decrease in the P 2p and N 1s signals with Zr deposition are consistent with (i) attenuation of photoelectrons from underlying atoms by those at the outermost surface/layers of the assembly (Figure 4.1 shows that the films become progressive thicker), and (ii) removal of the opposite adsorbate from the assembly during a deposition. This latter process has been observed in other LBL systems,[33] and would be expected to be operable to some degree in these depositions. XPS probes on the order of 10 nm into materials so it is reasonable that a substrate (Al 2p) peak is detected. This signal (the atomic percent Al detected) decreases steadily with increasing film thickness.

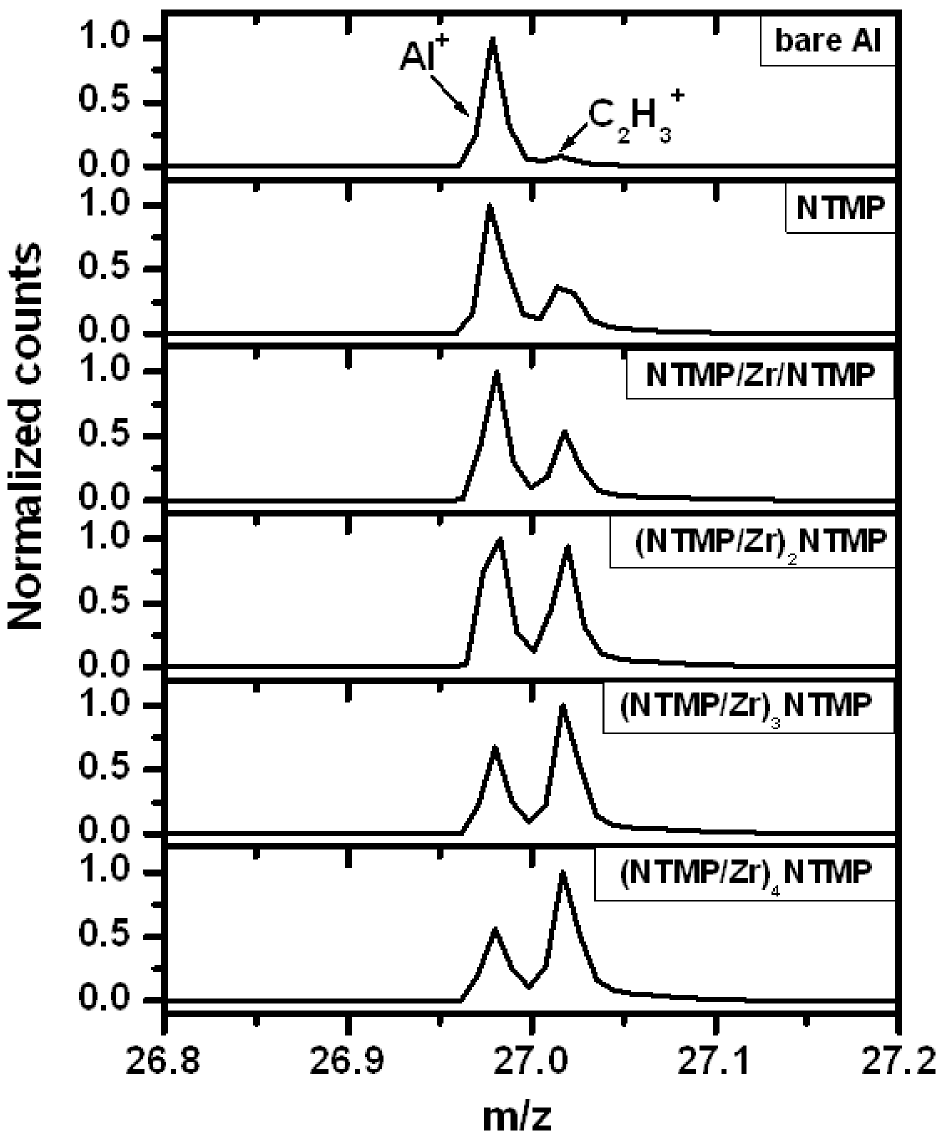

Figure 4.3 Effect of the increasing thickness via sequential deposition of NTMP and Zr(IV) layers on the Al^+ positive ion signal in ToF-SIMS.

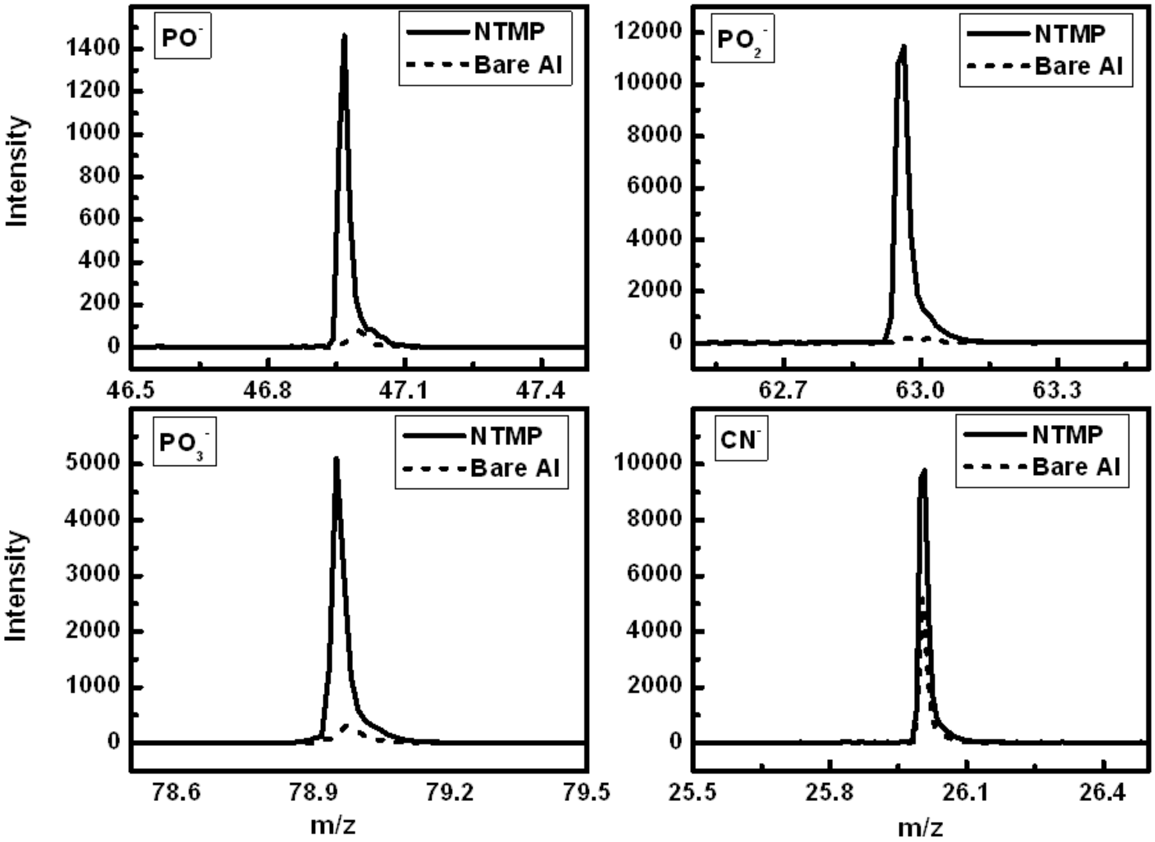

Figure 4.4 Comparison of negative ion signal obtained using Cs$^+$ for a bare aluminum and a NTMP coated substrate.

4.4.1.3 Time-of-flight secondary ion mass spectrometry (ToF-SIMS)

After each deposition, the surfaces were also probed with ToF-SIMS using Cs^+ primary ions. The positive ion spectrum of the bare alumina substrate showed a large Al^+ peak, along with a series of hydrocarbon fragments – virtually all surfaces show at least some adventitious carbon, and adventitious carbon would certainly be expected on the rather high free energy surfaces that should result from the deposition of NTMP and Zr^+. As the film increased in thickness, this Al^+ signal appeared to be attenuated. Figure 4.3 shows the m/z 27 region from the ToF-SIMS spectra of aluminum coated with progressively thicker films of NTMP and Zr(IV). This region shows two signals with the same nominal mass. The inorganic Al^+ signal shows the expected mass deficit (it appears just below the nearest integer m/z value) and the organic $C_2H_3^+$ fragment shows the expected mass excess (it appears just above the nearest integer m/z value). The decrease in the Al^+ signal relative to the $C_2H_3^+$ peak is again consistent with the deposition of an increasingly thick layer over the substrate. A relatively small Zr^+ peak was observed in the spectra after deposition of Zr(IV), which is consistent with the observation of zirconium in the films by XPS. The negative ion spectrum of NTMP coated alumina showed the expected CN^-, PO^-, PO_2^-, and PO_3^- peaks, which confirms the attachment of the NTMP molecule (see Figure 4.4).[42-43] The bare alumina also yielded a CN^- peak, confirming surface contamination of the substrate with nitrogen, which was also observed by XPS.

4.4.1.4 Atomic force microscopy (AFM)

AFM was used to evaluate the roughness of the NTMP/Zr(IV) coatings after each deposition. Even after deposition of 5 layers of NTMP and 4 layers of Zr, the resulting films are extremely flat with rms roughness values below 0.5 nm (Figure 4.5).

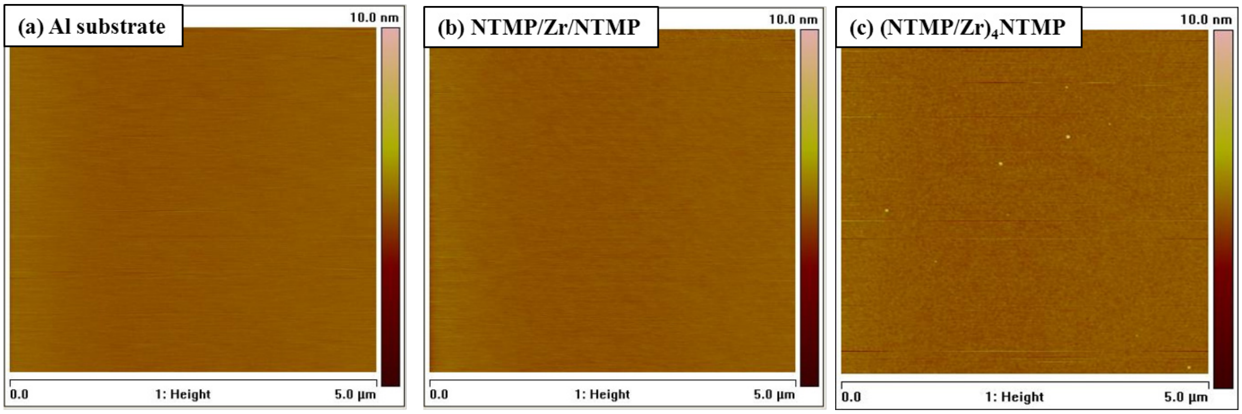

Figure 4.5 AFM images of (a) bare aluminum, and after deposition of (b) NTMP/Zr(IV)/NTMP, and (c) (NTMP/Zr(IV))$_4$NTMP.

4.4.2 Elevated temperature deposition of NTMP and Zr(IV)

4.4.2.1 Ellipsometry thickness

Deposition of NTMP at 70 °C resulted in an increase in film thickness of 0.02 ± 0.08 nm by SE. However, the following deposition of Zr(IV) at 70°C completely etched the surface, removing the alumina substrate, as evidenced by an overall decrease in film thickness from ca. 22 nm to 1.7 nm, which is essentially the thickness of the native oxide layer on the silicon wafer. This removal of alumina appears to be a result of etching in a low pH and high temperature environment – the pH of the Zr(IV) solution is 2.5.

4.4.2.2 X-ray photoelectron spectroscopy

XPS confirmed the attachment of NTMP at elevated temperature via nitrogen and phosphorus signals. Here, the atomic percentages of both nitrogen and phosphorus were higher in comparison to the results from NTMP deposited at room temperature. In particular, the atomic percentages of nitrogen and phosphorus were 5.3 % and 15.4 %, respectively, for NTMP deposited at 70 °C, compared to 4.5 % and 9.4 %, respectively, for deposition at room temperature. The NTMP molecule consists of three P atoms and one N atom: hence, the P/N ratio is expected to be 3. The P/N ratio for the higher temperature deposition was 2.9, which is very close to 3, but the deposition at room temperature gave a lower P/N ratio of 2.1. A possible explanation here could be nitrogen contamination of the alumina substrate, which was observed by both XPS and ToF-SIMS. At higher temperature, the nitrogen contamination may be removed/replaced during NTMP deposition, which may not occur, or occur to a lesser extent, at lower temperature. This possibility was supported by the following analysis. If the nitrogen signal from the 'bare' aluminum substrate was subtracted from the nitrogen signal obtained after NTMP deposition at room temperature, the P/N ratio became 2.7, which is closer to the theoretical value. I also noted that the percent aluminum (79.3 %) found after the higher temperature NTMP deposition on aluminum is lower than the amount (86.1%) observed after the lower temperature deposition, which again suggests greater NTMP surface coverage in the higher temperature deposition. The complete etching of the alumina layer after the surface was exposed to the Zr(IV) solution at high temperature, which was suggested by SE, was validated by XPS. Here, XPS showed no aluminum signal at 73 eV (see Figure 4.6). The same XPS analysis showed a Zr peak and a very small phosphorus signal.

4.4.2.3 Time-of-flight secondary ion mass spectrometry (ToF-SIMS)

The positive and negative ion mass spectra of the NTMP deposited at 70 °C were similar to the spectra obtained after deposition of NTMP at room temperature. The etching of the alumina surface after 'deposition' of zirconium at 70 °C was further validated by the positive ion ToF-SIMS spectrum, which showed no Al^+ signal (see Figure 4.6).

4.4.2.4 AFM

Higher temperature deposition of NTMP does not affect surface topography. The surface remained smooth with a 0.3 nm rms roughness; although the deposition of zirconium at 70 °C completely etched the alumina, the surface roughness remained minimal.

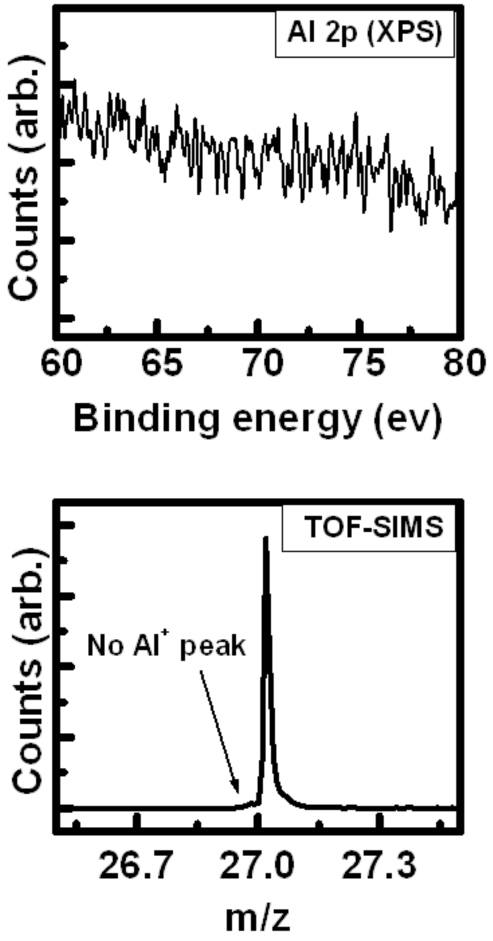

Figure 4.6 XPS and TOF-SIMS of a sample coated/exposed to NTMP and Zr(IV) at 70 °C.

4.5 Conclusions

A nine layer LBL assembly with a corrosion inhibitor, nitrilotris(methylene)triphosphonic acid, and Zr(IV) was prepared on alumina at room temperature. Its ellipsometric thickness increased in a linear fashion. XPS showed an increase in the nitrogen and phosphorus signals with deposition of each layer of NTMP, and a small decrease in the zirconium signal. An opposite pattern was observed upon deposition of zirconium. Negative ion ToF-SIMS showed PO^-, PO_2^-, PO_3^-, and CN^- peaks, confirming the adsorption of NTMP. Both XPS and ToF-SIMS showed a decrease in the aluminum signal with an increase in the number of layers deposited. The LBL assembly could not be constructed at 70 °C. The deposition of NTMP occurred at this temperature, as confirmed by XPS and ToF-SIMS, but the Zr(IV) solution etched the alumina surface. Evidence for the essentially complete removal of this layer was provided by SE, XPS, and ToF-SIMS. AFM showed that all films were extremely smooth with rms roughnesses below 0.5 nm.

4.6 References

1. Sagiv, J. *J. Am. Chem. Soc.* **1980,** *102* (1), 92-98.
2. Wasserman, S. R.; Tao, Y. T.; Whitesides, G. M. *Langmuir* **1989,** *5* (4), 1074-1087.
3. Textor, M.; Ruiz, L.; Hofer, R.; Rossi, A.; Feldman, K.; Hähner, G.; Spencer, N. D. *Langmuir* **2000,** *16* (7), 3257-3271.
4. Attavar, S.; Diwekar, M.; Linford, M. R.; Davis, M. A.; Blair, S. *Appl. Surf. Sci.* **2010,** *256* (23), 7146-7150.
5. Hoque, E.; DeRose, J.; Hoffmann, P.; Bhushan, B.; Mathieu, H. *J. Phys. Chem. C* **2007,** *111* (10), 3956-3962.
6. Linford, M. R.; Fenter, P.; Eisenberger, P. M.; Chidsey, C. E. *J. Am. Chem. Soc.* **1995,** *117* (11), 3145-3155.

7. Niederhauser, T. L.; Jiang, G.; Lua, Y.-Y.; Dorff, M. J.; Woolley, A. T.; Asplund, M. C.; Berges, D. A.; Linford, M. R. *Langmuir* **2001,** *17* (19), 5889-5900.

8. Lee, M. V.; Guo, D.; Linford, M. R.; Zuilhof, H. *Langmuir* **2004,** *20* (21), 9108-9113.

9. Shirahata, N.; Linford, M. R.; Furumi, S.; Pei, L.; Sakka, Y.; Gates, R. J.; Asplund, M. C. *Chem. Commun.* **2009,** (31), 4684-4686.

10. Cannon, B. R.; Lillian, T. D.; Magleby, S. P.; Howell, L. L.; Linford, M. R. *Precision engineering* **2005,** *29* (1), 86-94.

11. Ramsier, R.; Henriksen, P.; Gent, A. *Surf. Sci.* **1988,** *203* (1), 72-88.

12. Zanzucchi, P.; Thomas, J. *J. Electrochem. Soc.* **1988,** *135* (6), 1370-1376.

13. Lines, M.; Perkins, R. T., Corrosion resistant wire-grid polarizer and method of fabrication. US patent 20,030,227,678, December 11, 2003.

14. Venables, J. D.; Tadros, M. E.; Ditchek, B. M., Durability of adhesively bonded aluminum structures and method for inhibiting the conversion of aluminum oxide to aluminum hydroxide. US patent 4,308,079, December 29, 1981.

15. Liakos, I. L.; Newman, R. C.; McAlpine, E.; Alexander, M. R. *Surf. Interface Anal.* **2004,** *36* (4), 347-354.

16. Van Alsten, J. G. *Langmuir* **1999,** *15* (22), 7605-7614.

17. Hofer, R.; Textor, M.; Spencer, N. D. *Langmuir* **2001,** *17* (13), 4014-4020.

18. Raman, A.; Dubey, M.; Gouzman, I.; Gawalt, E. S. *Langmuir* **2006,** *22* (15), 6469-6472.

19. Gao, W.; Dickinson, L.; Grozinger, C.; Morin, F. G.; Reven, L. *Langmuir* **1996,** *12* (26), 6429-6435.

20. Fontes, G. N.; Malachias, A.; Magalhães-Paniago, R.; Neves, B. R. A. *Langmuir* **2003,** *19* (8), 3345-3349.

21. Guerrero, G.; Mutin, P.; Vioux, A. *Chem. Mater.* **2001,** *13* (11), 4367-4373.

22. Adden, N.; Gamble, L. J.; Castner, D. G.; Hoffmann, A.; Gross, G.; Menzel, H. *Langmuir* **2006,** *22* (19), 8197-8204.

23. Gawalt, E. S.; Avaltroni, M. J.; Koch, N.; Schwartz, J. *Langmuir* **2001,** *17* (19), 5736-5738.

24. Paramonov, P. B.; Paniagua, S. A.; Hotchkiss, P. J.; Jones, S. C.; Armstrong, N. R.; Marder, S. R.; Brédas, J.-L. *Chem. Mater.* **2008,** *20* (16), 5131-5133.

25. Lee, H.; Kepley, L. J.; Hong, H. G.; Mallouk, T. E. *J. Am. Chem. Soc.* **1988,** *110* (2), 618-620.

26. Lee, H.; Kepley, L. J.; Hong, H. G.; Akhter, S.; Mallouk, T. E. *The Journal of Physical Chemistry* **1988,** *92* (9), 2597-2601.

27. Hoekstra, K. J.; Bein, T. *Chem. Mater.* **1996,** *8* (8), 1865-1870.

28. Hong, H. G.; Sackett, D. D.; Mallouk, T. E.. *Chem. Mater.* **1991,** *3* (3), 521-527.

29. Latos, E. J.; Payne, J. C., Corrosion inhibitors. US patent 4,409,121, October 11, 1983.

30. McNeel, T. E.; Harrell, J. A., Method for the reduction or prevention of tannin-staining on a surface susceptible to tannin-staining through the use of a complexing agent for a transition-metal ion and compositions containing such a complexing agent. US patent 5,320,872, June 14, 1994.

31. Bishop, M.; Bott, S. G.; Barron, A. R. *Chem. Mater.* **2003,** *15* (16), 3074-3088.

32. Schütte, M.; Kurth, D. G.; Linford, M. R.; Cölfen, H.; Möhwald, H. *Angew. Chem. Int. Ed.* **1998,** *37* (20), 2891-2893.

33. Linford, M. R.; Auch, M.; Möhwald, H. *J. Am. Chem. Soc.* **1998,** *120* (1), 178-182.

34. Lvov, Y.; Decher, G.; Moehwald, H. *Langmuir* **1993,** *9* (2), 481-486.

35. Caruso, F.; Niikura, K.; Furlong, D. N.; Okahata, Y. *Langmuir* **1997,** *13* (13), 3422-3426.

36. Jensen, D. S.; Kanyal, S. S.; Madaan, N.; Vail, M. A.; Dadson, A. E.; Engelhard, M. H.; Linford, M. R. *Surf. Sci. Spectra* **2013,** *20* (1), 36-42.

37. Madaan, N.; Kanyal, S. S.; Jensen, D. S.; Vail, M. A.; Dadson, A. E.; Engelhard, M. H.; Samha, H.; Linford, M. R. *Surf. Sci. Spectra* **2013,** *20* (1), 43-48.

38. Jensen, D. S.; Kanyal, S. S.; Madaan, N.; Hancock, J. M.; Dadson, A. E.; Vail, M. A.; Vanfleet, R.; Shutthanandan, V.; Zhu, Z.; Engelhard, M. H. *Surf. Interface Anal.* **2013,** *45* (8), 1273-1282.

39. Jiang, G.; Rivera, F.; Kanyal, S. S.; Davis, R. C.; Vanfleet, R.; Lunt, B. M.; Shutthanandan, V.; Linford, M. R. *Optical Engineering* **2011,** *50* (1), 015201-015201-10.

40. Synowicki, R. A. *Thin Solid Films* **1998,** *313–314*, 394-397.

41. Gervais, F., Aluminum Oxide (Al2O3). In *Handbook of Optical Constants of Solids*, Palik, E. D., Ed. Academic Press: Burlington, 1997; pp 761-775.

42. Madaan, N.; Diwan, A.; Linford, M. R. *Surf. Interface Anal.* **2015,** *47* (1), 56-62.

43. Saini, G.; Gates, R.; Asplund, M. C.; Blair, S.; Attavar, S.; Linford, M. R. *Lab on a Chip* **2009,** *9* (12), 1789-1796.

Chapter 5 Conclusions

5.1 Conclusions

I have described a new method for the preparation of SPME stationary phases by the sputtering of silicon. The sputtered coatings are porous and columnar. The introduction of C18 chains onto these surfaces was demonstrated. Prior to use, sputtered fibers were preconditioned at 320 °C for 3 h. Sputtered, silanized fibers outperformed a commercial fiber (7 μm PDMS) for most of the compounds tested. Sputtered fibers did not show any carry-over between extractions. The fibers were robust and showed no signs of degradation after 300 extractions. To the best of my knowledge, no one has reported in the literature the creation and preparation of adsorbents for SPME by sputtering or any other physical vapor deposition technique.

In my second project, I introduced a simple and fast method for the preparation of SHS. Rough topography for SHS could be prepared in 60 min by the aggregation of nanosilica during UF polymerization on both silicon and glass substrates. For glass, a priming layer of UF polymer was used. Vapor deposition of a fluorosilane was used to render the rough surfaces hydrophobic. These surfaces exhibited WCA greater than 150° with low sliding angles.

In my third project, a nine-layered assembly using an amino phosphonate and zirconium was prepared at room temperature on alumina. Ellipsometry showed a steady increase in thickness with the deposition of each layer. XPS and ToF-SIMS further confirmed the deposition of each layer. At a higher temperature (70 °C), assembly did not take place due to etching of the alumina layer.

5.2 Future Work

The primary objective of my graduate work was the development of new stationary phases for SPME that have better extraction capabilities than commercial ones. I have been successful in making such adsorbents. In my work, I prepared 1.0 and 2.0 µm sputtered coatings. I recommend that fibers with different sputtered layer thicknesses be prepared, such as, 3.0, 4.0, and 5.0 µm. These greater thicknesses should enhance the capacities of these fibers. I used a C18 monofunctional silane to coat these fibers. Investigation of polyfunctional silanes and silanes with other end groups will be important for achieving better selectivity and performance.

SHS prepared using a nanosilica-UF composite was unable to pass the Scotch tape test. To enhance the robustness of these surfaces, a pretreatment with a silane, such as, aminopropyltriethoxy silane (APTES), prior to deposition of nanosilica-UF composite should impart greater strength to these surfaces.

Nitrilotris(methylene)triphosphonic acid (NTMP) is a known corrosion inhibitor used in industry. In my work, I have successfully constructed a thin multilayer with this molecule. Commercial optical devices, such as polarisers, need protection from corrosion in moist temperatures. This multilayer assembly will provide better corrosion resistance than a single layer of NTMP. I recommend it be applied to commercial devices.

Appendix 1 Models in Ellipsometry: The ‘No Model’ Model (Just Monitoring Psi and Delta)

A1.1 Abstract

Modeling is a central part of data analysis in spectroscopic ellipsometry. Here I will discuss no model at all. That is, the simple monitoring of psi (ψ) and delta (Δ) values from a series of ellipsometric measurements as a function of time or some other experimental variable. This can be a valuable way of confirming that a change has taken place (or not taken place) in a thin film or material. I will show here the use of this approach for different material systems that include thin films of chromium of different thicknesses on silicon, the atomic layer deposition (ALD) of Er_2O_3 and Al_2O_3, the ALD of copper, the hydrogenation and dehydrogenation of Mg-Ni mirrors, and sputtered films of bismuth, tellurium, and selenium.

A1.2 Introduction

In 1887, Paul Drude introduced ellipsometry to the world.[1] Ellipsometry is an optical tool that provides information about the interaction of light with materials. It is fast, generally non-destructive, and non-invasive. It can be applied to characterize surfaces, interfaces, alloys, and multilayered films. It is a ratiometric technique so it (i) does not depend on the intensity of the light it employs, and (ii) provides highly sensitive, accurate, and reproducible results. Although, ellipsometry provides accurate information about film thicknesses, optical constants, roughnesses, and inhomogeneities, it is not capable of measuring any of these parameters directly. It only measures two quantities: ψ and Δ. The quantity Δ represents the phase difference between the p- and s-components of polarized light that are reflected from a surface. Tan ψ represents the ratio of their amplitudes.

To derive material properties from an ellipsometric measurement, one must in general build a model. Based on the physical laws that govern the interaction of light with matter, e.g., Fresnel's equations, predicted values of ψ and Δ are generated from one's model. In a subsequent regression analysis, the parameters of the model, e.g., film thickness or optical constants, are varied to minimize the difference between the predicted and experimental values of ψ and Δ.

To become successful in model building in ellipsometry, the following are important. First, data fitting requires practice. Second, it is helpful to read the literature and consult with more experienced colleagues. Third, it is useful to get to know some of the commonly used models that are used for different types of materials. These include the Cauchy, Sellmeier, Gaussian, Lorentzian, Drude, and Tauc-Lorentz models. Each is useful for a broad range of materials. There are also other models that one may wish to become familiar with. Fourth, when dealing with complex materials and building ellipsometric models for them, it is often very helpful to consider the information obtained from other analytical techniques. Information from atomic force microscopy (AFM), transmission electron microscopy (TEM), scanning electron microscopy (SEM), X-ray diffraction (XRD), etc. can guide the creation of an ellipsometric model so that it stays grounded in reality, remaining consistent with other reliable information.

In this contribution the ellipsometric model I consider is no model at all – I referred to this situation in the title (with a little humor) as the 'no model' model. Here one simply plots ψ and/or Δ as a function of some process variable, such as time, temperature, or exposure of one's material to a reagent. Alternatively, one may plot ψ and Δ against each other. The fundamental premise behind this approach is very simple. As long as ψ and Δ are not changing, one assumes that the material is not changing either. When ψ and Δ do change, one assumes something has happened to the material. Thus, simply monitoring ψ and Δ is a powerful way of studying many material processes.

A1.2.1 Examples from the Literature of the 'No Model' Model

A1.2.1.1 Example 1. Analysis of thin films of Cr on silicon.

Tompkins and coworkers[2] studied different thicknesses of chromium on silicon, plotting the resulting Δ and ψ values that were obtained at a single wavelength (632.8 nm), and at an angle of incidence of 70°. This is the wavelength of the HeNe laser that has been used in many single wavelength ellipsometers. Many people today use spectroscopic (multi-wavelength) ellipsometers. Figure A1.1 shows a plot of Δ vs. ψ for various thicknesses of the metal. The sensitivity of the technique to the thinner films is apparent in this plot – notice how much ψ and Δ change along the path between the film-free substrate and the 10 nm film. In contrast, Figure A1.1 teaches that ellipsometry has less and less power to differentiate between increasingly thick films of Cr – consider how little ψ and Δ change between the points corresponding to the 20 nm and 30 nm films. Of course, as soon as the Cr film is opaque to the light, i.e., once the light can no longer penetrate the film, be reflected by the substrate, and escape from the material again, the signal from the Cr-coated surface remains constant even with the deposition of additional material. At this point, ellipsometry is insensitive to Cr deposition. Of course, it is assumed here that film morphology and chemistry do not change as deposition continues.

Tompkins and coworkers also showed *spectroscopic* ellipsometry data. Figure A1.2 shows plots of ψ(λ) and Δ(λ) for 5 – 30 nm films of Cr on silicon. For this data, the angle of incidence was 75° and the wavelength range was 300 – 800 nm. These data suggest that over the range of thicknesses studied, Δ is more sensitive to changes in film thickness than ψ. That is, there is little difference between the ψ vs. wavelength curves for the thickest film and the opaque film, while there is still a large difference between the corresponding curves for Δ.

Data like that plotted in Figure A1.1 could potentially be useful for quality control in a deposition process. Indeed, as will be the case for the Willis work discussed below, the point corresponding to the film-free surface would be sensitive to the cleaning and preparation of the substrate, and the points along the Δ- ψ trajectory would be sensitive to film deposition conditions. Figure A1.2 similarly contains data that could be useful for quality control. Thus, if the ψ(λ) or Δ(λ) spectra deviated too much from those obtained from standard/accepted materials, one might judge one's material to be out of spec.

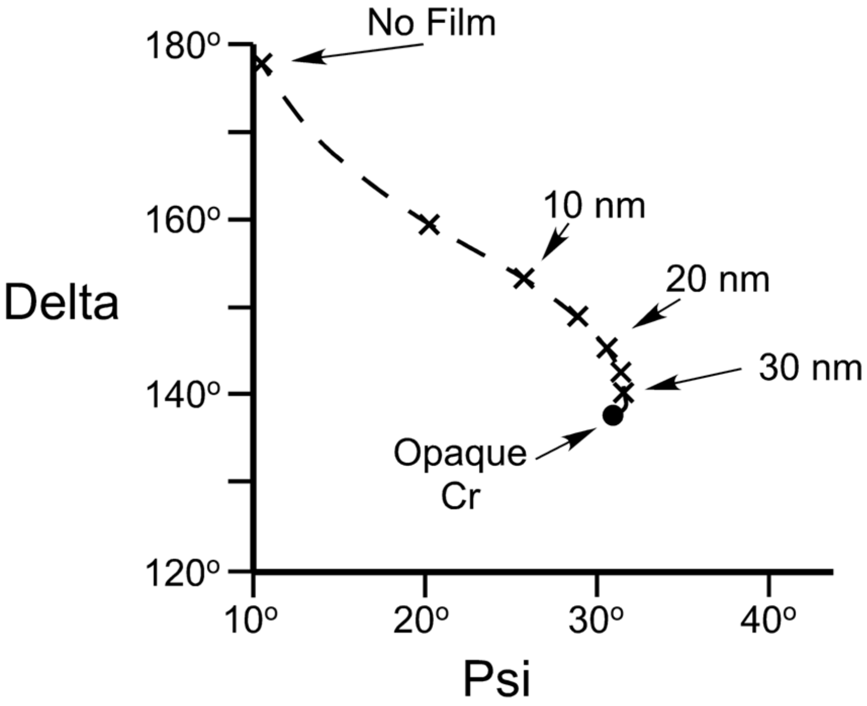

Figure A1.1 Plot of Δ vs. ψ for films of Cr of different thicknesses on silicon. Data from Harland Tompkins, with permission.

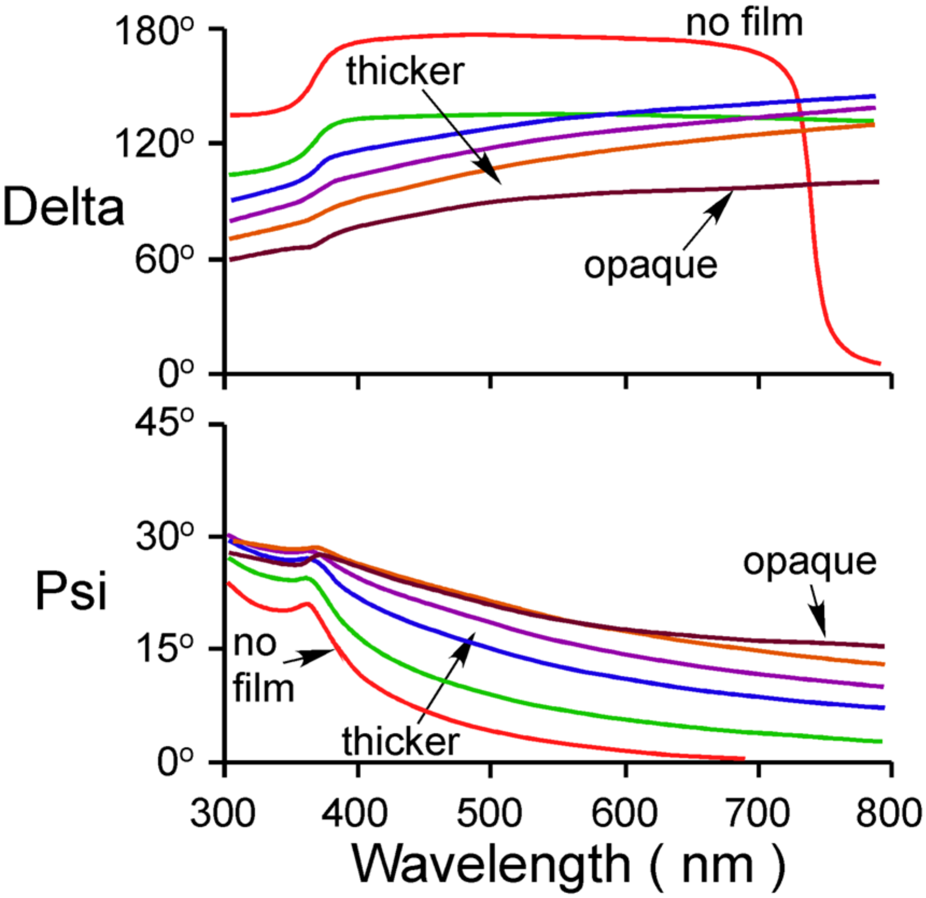

Figure A1.2 Ellipsometric data at multiple wavelengths from silicon surfaces with different thicknesses of chromium (5 – 30 nm) on them. (Data from Harland Tompkins, with permission.)

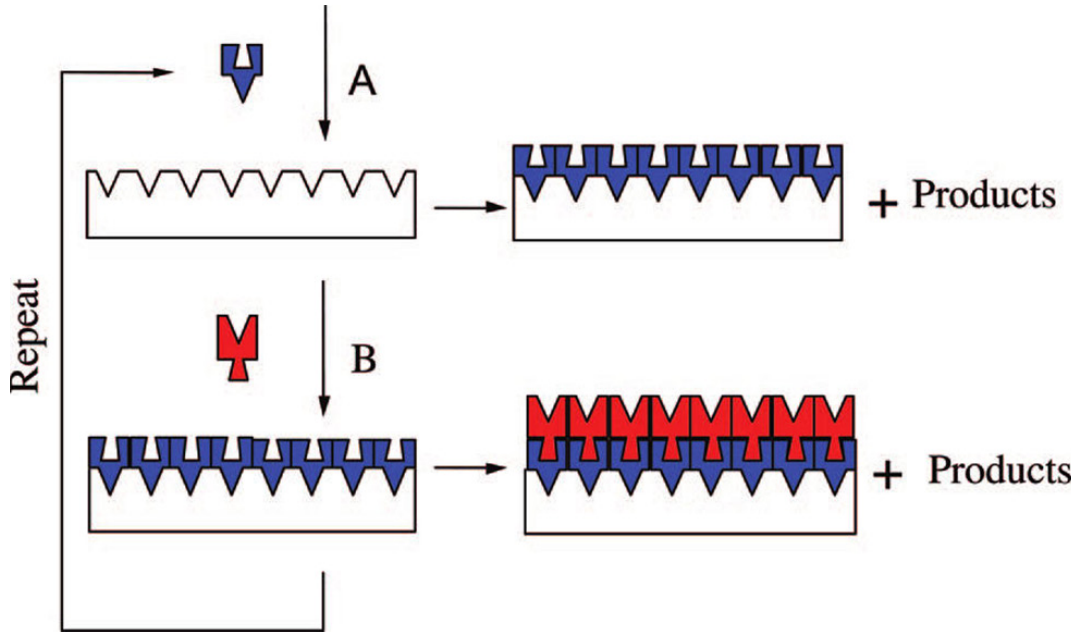

Figure A1.3 Idealized representation of ALD showing two self-limiting surface reactions. “Reprinted (adapted) with permission from (“Atomic Layer Deposition: An Overview” Chemical Reviews, Vol. 110, pgs 111-131 by Steven M. George). Copyright (2010) American Chemical Society."

A1.2.1.2 Example 2. In situ analysis of the ALD of Er_2O_3 and Al_2O_3

A few years ago, Kessels and coworkers published a review on the *in situ* spectroscopic ellipsometry analysis of films grown by atomic layer deposition (ALD).[3] Prior to discussing some of the ellipsometry results they showed in their article, I'll briefly review ALD. In theory, ALD is a simple technique. Ideally, it involves the deposition of thin and conformal films via sequential, self-limiting surface reactions. Figure A1.3 shows an idealization of the process. First, precursor A reacts with the surface. Note that (i) the chemistry of the surface and compound A have been chosen so that not more than one monolayer of species A can deposit on the surface, and (ii) compound A can neither react with itself in the gas phase nor with chemisorbed A. After this first reaction has taken place, any unreacted compound A, as well as any by-products of the first reaction, are removed from the chamber. Compound B is then introduced. This species is similarly designed to be able to react with the active surface created by the chemisorption of compound A, but not with itself. In the first reaction, surface-A bonds are formed. In the second, A-B bonds are formed. After removing unreacted B and any by-products of the reaction between chemisorbed A and B, the process is repeated. Compound A is then reintroduced. It reacts with the chemisorbed B. Ideally, ABAB type films are grown in this manner.

Note that the word 'ideally' was used twice and 'idealization' once in the preceding paragraph. That is, the picture of ALD suggested in Figure A1.3 is an *idealization*. There are a number of reasons why this may not be the case. Here are four. First, many, if not most, ALD reactions result in the deposition of sub-monolayer quantities of material, not the complete monolayers suggested in Figure A1.3. This fact leads to an important limitation of ALD: it is slow. Second, many ALD reactions require an induction period before they can begin, i.e., the surface may not be able to receive and react with the first (or even second) ALD reactant as depicted in

Figure A1.3. Third, multiple bonds may be formed between an adsorbate and the surface. Fourth, the compounds themselves, A or B, may react with themselves and/or they may decompose to some degree at the temperature of the reaction. Because of the *complexity* of many real ALD reactions, the ability to monitor them *in situ* is important. Spectroscopic ellipsometry is an ideal tool for this purpose.

Figure A1.4a shows a schematic of a spectroscopic ellipsometer attached to an ALD chamber. The optical path of the light from its source, into the chamber, off of the surface, and to the detector is represented by red arrows. Gate valves, represented by black X's, protect the windows of the system from deposition. Obviously they need to be opened before a measurement can be taken. However, a measurement can be taken after every deposition. The chamber has multiple inlets for precursors, a purge gas, ozone, a plasma feed gas, and reactants (H_2O and NH_3). Clearly, this is quite a versatile system. Perhaps the only significant limitation of this *in situ* approach is that the angle of the ellipsometer is fixed relative to the surface – it would not be possible to use an ellipsometric technique like interference enhancement,[4] which requires that data be collected at multiple angles. Nevertheless, the pros of this approach clearly outweigh any cons. Figure A1.4b shows a picture of a real spectroscopic ellipsometer attached to an ALD system.

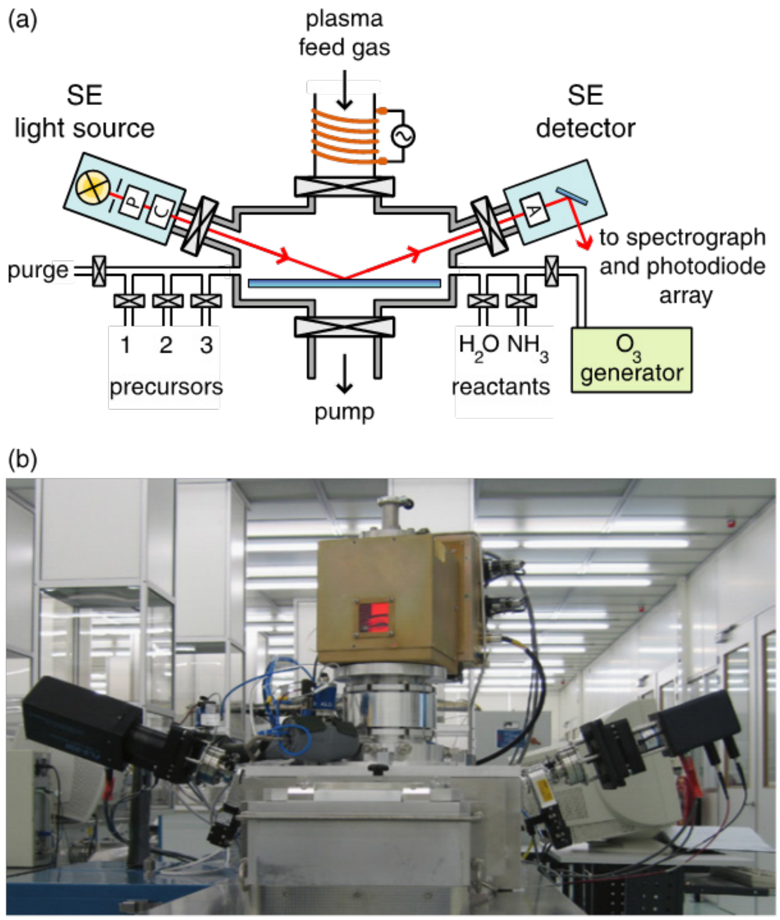

Figure A1.4 (a) Schematic of a spectroscopic ellipsometer attached to an ALD chamber. (b) Picture of such a system. E. Langereis, S.B.S. Heil, H.C.M. Knoops, W. Keuning, M.C.M. van de Sanden, W.M.M. Kessels ‘*In situ* spectroscopic ellipsometry as a versatile tool for studying atomic layer deposition’ J. Phys. D: Appl. Phys. 42 (2009) 073001 (19pp). doi:10.1088/0022-3727/42/7/073001. © IOP Publishing. Reproduced by permission of IOP Publishing. All rights reserved.

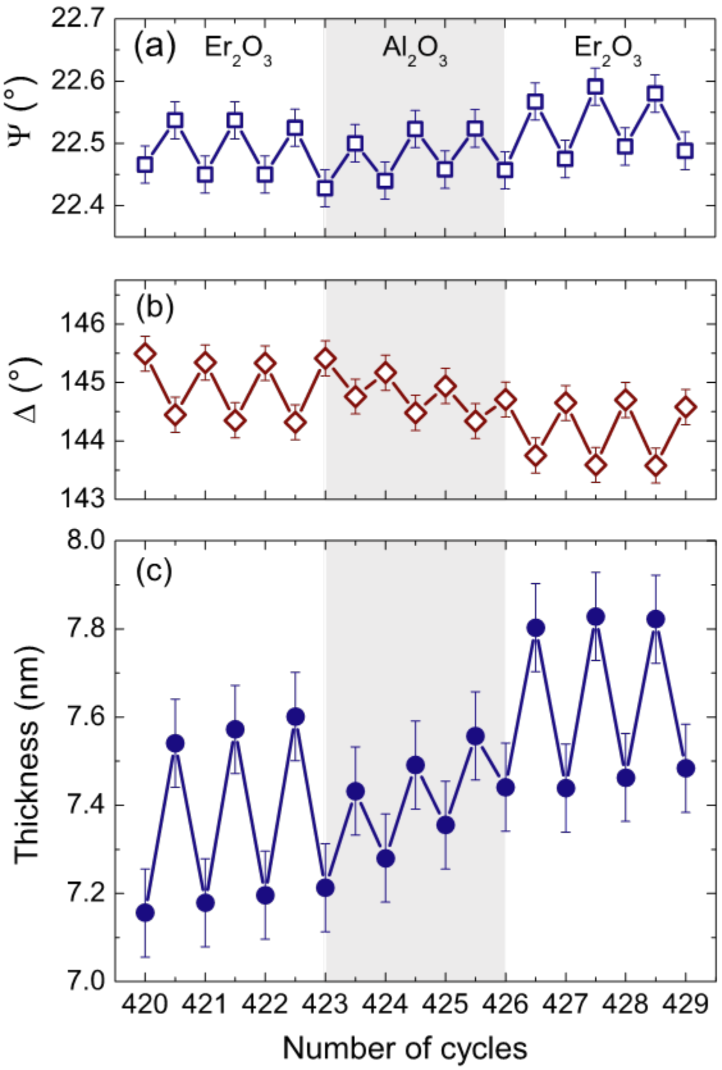

Figure A1.5 (a) ψ, (b) Δ, and (c) thickness values obtained from spectrscopic ellipsometry for the atomic layer deposition of Er_2O_3 and Al_2O_3. E. Langereis, S.B.S. Heil, H.C.M. Knoops, W. Keuning, M.C.M. van de Sanden, W.M.M. Kessels J. Phys. D: Appl. Phys. 42 (2009) 073001 (19pp). doi:10.1088/0022-3727/42/7/073001. © IOP Publishing. Reproduced by permission of IOP Publishing. All rights reserved.

Figure A1.5 shows plots of ψ, Δ, and film thickness vs. the number of ALD cycles for two different chemistries applied to the same substrate. The left and right parts of panels (a), (b), and (c) show results from the depositions of three layers of Er_2O_3. The center part of the plot (a), (b), and (c) contains results from the deposition of three layers of Al_2O_3. The plots of ψ and Δ vs. number of cycles indicate that *something* is happening to the surface with each deposition – ψ and Δ do not stay constant. Overall, these responses are larger for the adsorption of the Er precursor ($Er(thd)_3$) than for the Al precursor ($Al(CH_3)_3$). $Er(thd)_3$ is larger than $Al(CH_3)_3$ so it is reasonable to expect larger signals from it (see Figure A1.6), assuming the areal fraction of the surface covered with the adsorbates is about the same. (Note also that the structure of $Er(thd)_3$ given in Figure A1.6 is somewhat misleading. $Er(thd)_3$ is an octahedral complex composed of three bidentate ligands with six equivalent Er-O bonds. A simple electron pushing exercise allows one to draw an equivalent structure to the one in Figure A1.6 with the 'unbonded' oxygen atoms now bonded to Er.) In addition, while $Al(CH_3)_3$ is commonly depicted as shown in Figure A1.6, it has a strong tendency to dimerize into a species with a formula of $Al_2(CH_3)_6$ that contains two three-center, two-electron bonds. The other reactive species in these two ALD reactions is an oxygen plasma. Finally, the submonolayer sensitivity of spectroscopic ellipsometry is emphasized. As noted above, submonolayer quantities of material are deposited in most ALD reactions, but signals in Figure A1.5 that are clearly measurable for each deposition. The (c) panel of Figure A1.5 shows changes in the thickness of the film as estimated by a Cauchy model for the films. These results are consistent with slow and steady film growth, and also with the removal of the organic ligands with each oxygen plasma exposure.

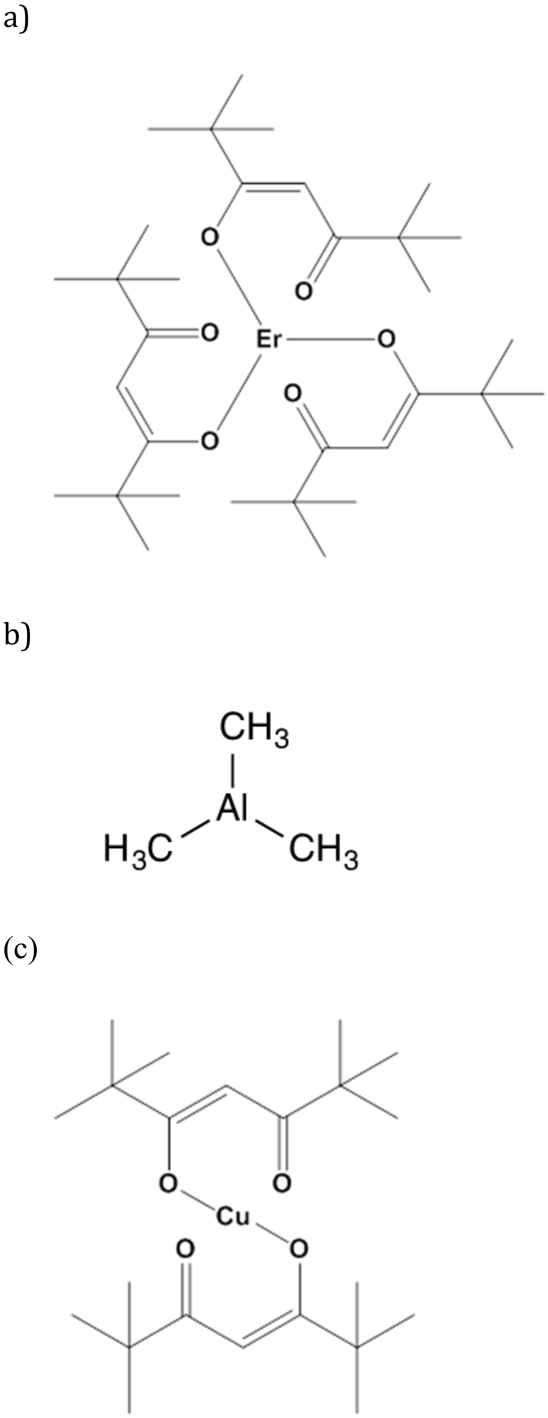

Figure A1.6 Structures of (a) $Er(thd)_3$, (b) $Al(CH_3)_3$, and (c) $Cu(thd)_2$.

A1.2.1.3 Example 3. In situ analysis of ALD of Cu on Pd

Willis and coworkers have also emphasized the significance of *in situ* ellipsometry in atomic layer deposition.[5] Their study focused on the ALD of copper on palladium seed layers. Similar to the case for the Er precursor in Figure A1.6a, the Cu precursor in Figure A1.6c is expected to have four equivalent Cu-O bonds. Interestingly, Willis and coworkers heated the windows of their system to prevent adsorption of reactants on them. The advantage of their approach (no gate valves) over the system described by Kessels and coworkers (see Figure A1.4) is the ability to monitor depositions as they occur, not at selective points during a deposition. However, with this approach the authors emphasized the need for precise control over window temperature (± 0.5 °C) to prevent the introduction of artifacts into the spectroscopic ellipsometry data. The other reactant used in their Cu depositions is hydrogen gas. The authors collected ellipsometry data over a fairly broad wavelength range: 370 – 1000 nm.

Saturation curves in ALD reveal the precursor/reactant dosages that are required to completely saturate a surface. If the system is behaving *ideally*, ALD film growth should stop at saturation. Beyond this point, deposition should be independent of the precursor/reactant dosage. Figures A1.7a and A1.7b show saturation curves for H_2 and $Cu(thd)_2$. These curves were obtained simply by plotting Δ vs. the dosage time for the precursors in question. In both cases, saturation occurred quickly, i.e., Δ levels off in 5 – 10 s. A simple monitoring of Δ was also used to study the He purge time. Figure A1.7c shows that Δ is largest for the shortest purge times. The very reasonable interpretation for these results, which was provided by the authors, is that low degrees of purging do not fully remove reactants from the system so that under these conditions film growth takes place by both ALD and chemical vapor deposition.

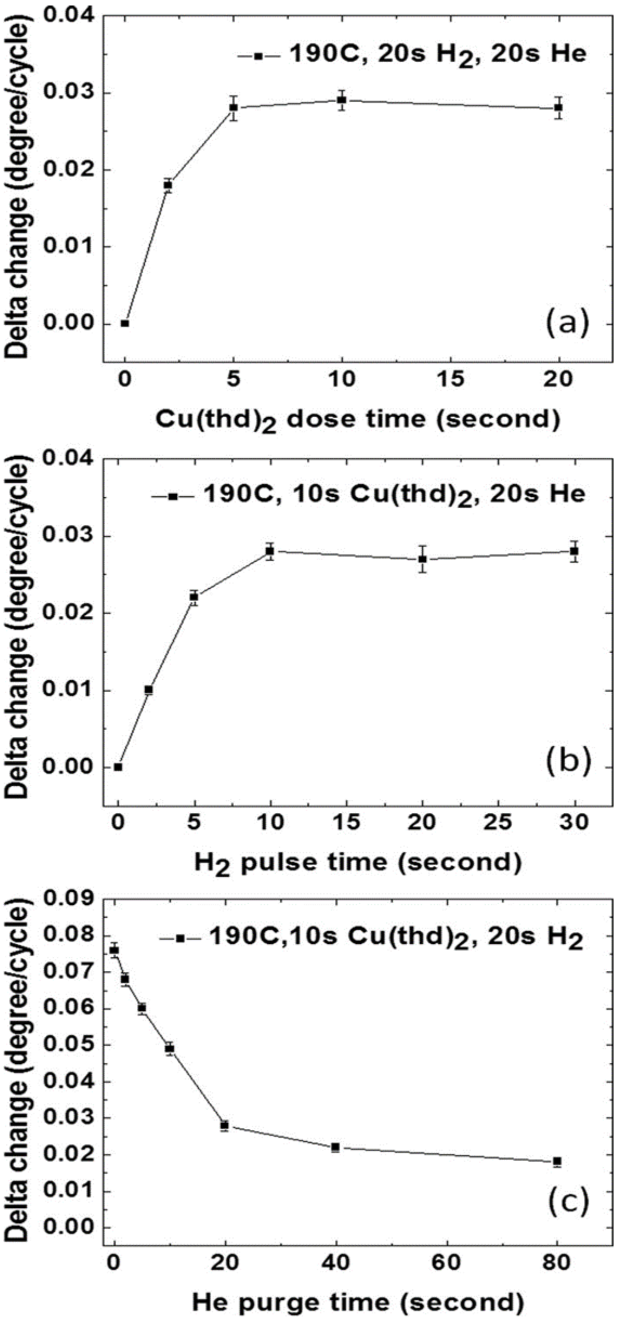

Figure A1.7 Saturation curves for (a) $Cu(thd)_2$ and (b) H_2 obtained by plotting the change in Δ with dose time. (c) Plot of Δ vs. He purge time. Reprinted with permission from ["*In-situ* spectroscopic ellipsometry study of copper selective-area atomic layer deposition of palladium" Journal of Vacuum Science and Technology A, Vol. 32, pgs. 041513-1 to 041513-10 by Xiaoqiang Jiang, Han Wang, Jie Qi, and Brian G. Willis]. Copyright [2014], American Vacuum Society.

As noted above, a plot of Δ vs. ψ can reveal valuable information about films and their growth processes. Figure A1.8 shows experimental and model plots of delta vs. psi for the ALD of Cu on Pd. While qualitatively similar to the experimental data, the model data were noticeably offset from the experimental results. Reasonable reasons for these differences are that (i) an ideal layer model was used to model the system – there was no allowance for interdiffusion between the layers, and (ii) bulk optical constants were used in the model calculations. As noted above, the position of the '0 cycle' (no film) point in the delta-psi space is sensitive to the preparation of the substrate, and the positions of the other points in the experimental curve are sensitive to their corresponding deposition conditions. Clearly, the Δ vs. ψ trajectory is a 'fingerprint' for the ALD process.

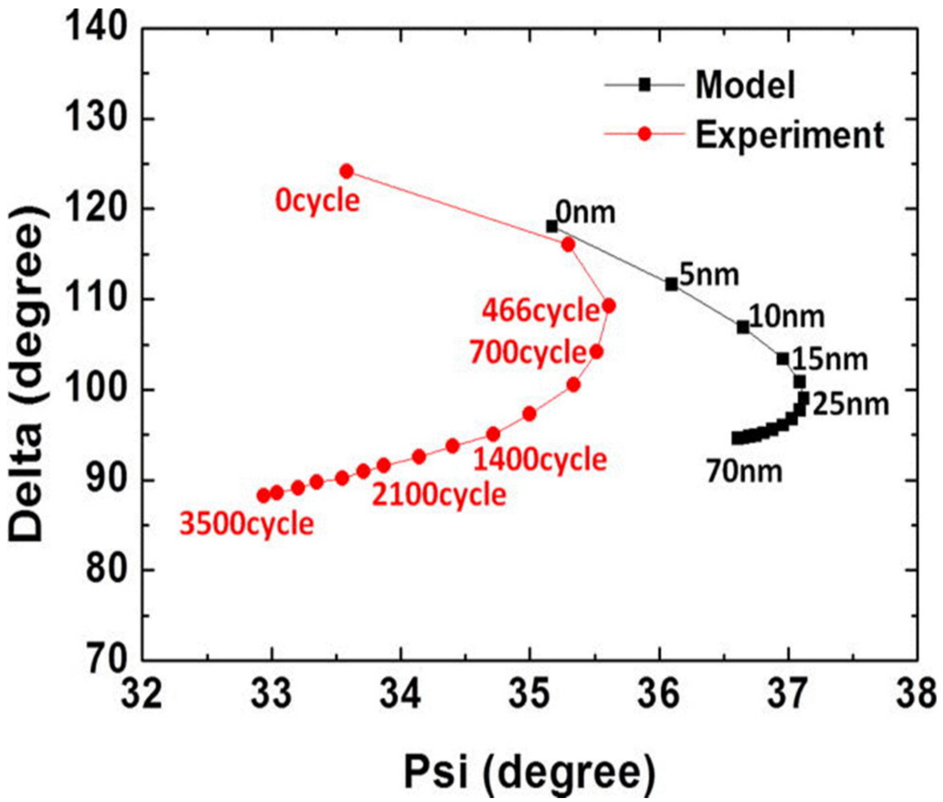

Figure A1.8 Experimental and model plots of Δ vs. ψ for the ALD of Cu on Pd. Reprinted with permission from ["*In-situ* spectroscopic ellipsometry study of copper selective-area atomic layer deposition of palladium" Journal of Vacuum Science and Technology A, Vol. 32, pgs. 041513-1 to 041513-10 by Xiaoqiang Jiang, Han Wang, Jie Qi, and Brian G. Willis]. Copyright [2014], American Vacuum Society.

A1.2.1.4 Example 4. In situ analysis of Mg_4Ni switchable mirrors

Yamada and coworkers deposited thin films of Mg_4Ni onto quartz substrates via the DC magnetron co-sputtering of Mg and Ni.[6] Without breaking vacuum, this Mg-Ni film was then capped with a sputtered layer of Pd. They reported (nominal) thicknesses of these films of ca. 35 nm and 7.5 nm, respectively. To test the hydrogenation of their mirrors, they exposed them to flowing 4% hydrogen in argon. The motivation for this work is as follows. In their metallic state, the metal alloy mirrors are reflective. However, the metal hydrides that are formed during hydrogenation are wide band gap semiconductors, i.e., the materials become transparent. To probe the optical changes in their materials during hydrogentation the authors measured ψ and Δ from 380 to 1650 nm every 2.8 s for more than 80 min. They then plotted the values of these parameters at 498, 617, 827, and 1228 nm as a function of time (see Figure A1.9). Interestingly, for the first ca. 18 min, the materials did not appear to change substantially. For the next ca. 5 minutes, significant changes in ψ and Δ were observed. The materials then appeared to asymptotically approach a final state. In addition to simply monitoring ψ and Δ, the authors built ellipsometric models for their materials to describe in detail the different materials in the different regions in their ψ/Δ vs. time plots. These latter analyses substantially increased their understanding of their materials. The authors also used this general approach to study the dehydrogenation (in dry air) of their materials (see Figure A1.10). Thus, this work nicely illustrates the monitoring of ψ and Δ in a material process, and also the value of subsequent, more detailed analysis of the data.

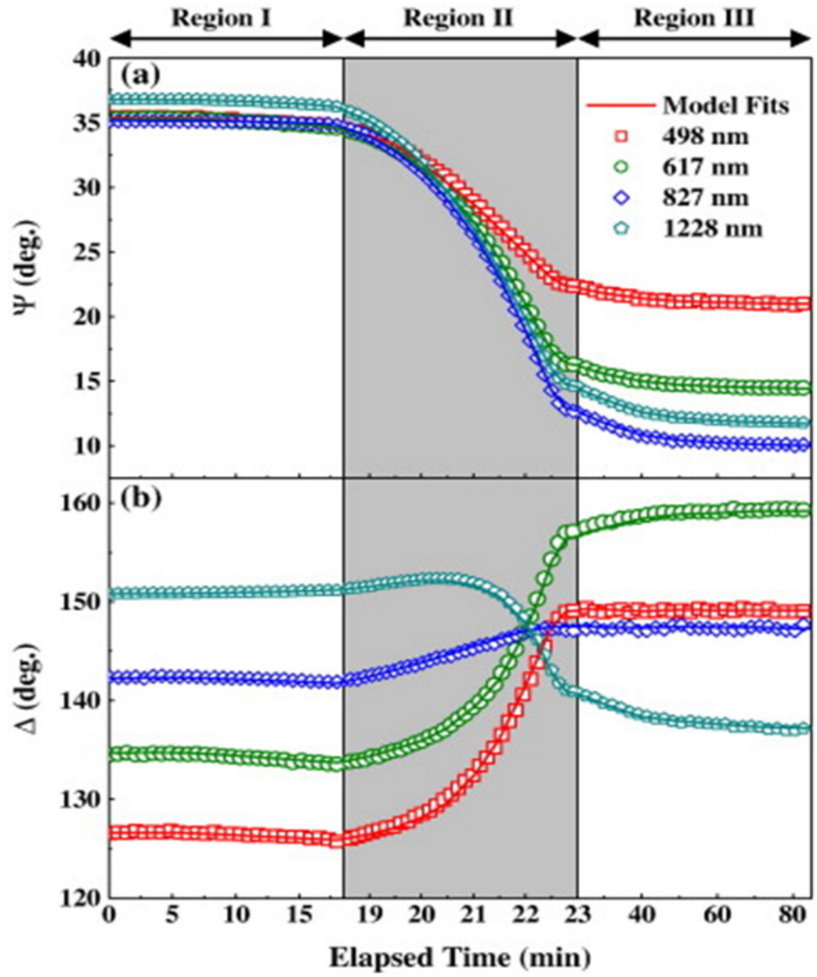

Figure A1.9 Values of ψ and Δ plotted at four different wavelengths against time during the hydrogenation of Mg-Ni mirrors.Reprinted with permission from "Ellipsometric study of optical switching processes of Mg-Ni based switchable mirrors" Thin Solid Films, 519, pgs 2941-2945 by Y. Yamada, K. Tajima, M. Okada, M. Tajawa, A. Roos, and K. Yoshimura. Copyright [2011], Elsevier.

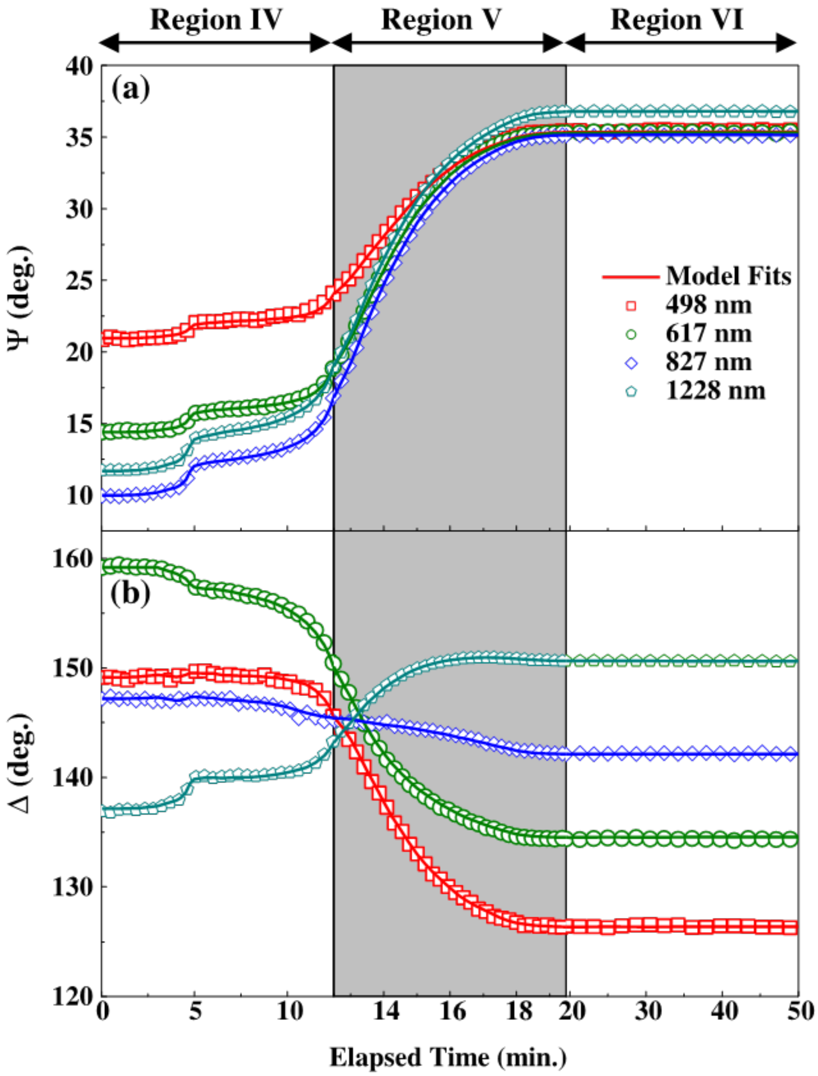

Figure A1.10 Values of ψ and Δ plotted at four different wavelengths against time during the dehydrogenation of Mg-Ni mirrors. Reprinted with permission from "Ellipsometric study of optical switching processes of Mg-Ni based switchable mirrors" Thin Solid Films, 519, pgs 2941-2945 by Y. Yamada, K. Tajima, M. Okada, M. Tajawa, A. Roos, and K. Yoshimura. Copyright [2011], Elsevier.

A1.2.1.5 Example 5. Analysis of materials for long-term digital data storage

During the past few years the Linford group at BYU has been actively working with collaborators Barry Lunt and Rob Davis, also at BYU, to develop new materials for long-term digital data storage.[7-9] This work contributed to the development of the M-DISC™ that is now sold by Millenniata (American Fork, UT, www.mdisc.com). Industry accepted longevity tests indicate that data stored on this DVD will last for more than 1000 years. The company has recently introduced a Blu-ray disk that also shows a high degree of longevity (hundreds of years). Plans are in the works to introduce a multilayer version of this Blu-ray product, which could have a capacity of 100 – 200 GBytes.

Some of the recent research at BYU from the Linford group in this area has focused on the development of other data storage media that could also have a high degree of permanence. To this end Linford and coworkers recently published a paper on the characterization of a sputtered bismuth-tellurium-selenium film that might function as the write layer for a permanent optical tape product.[10] To begin to understand the stability of this layer, it was left out in the air for ca. 100 days and analyzed regularly by spectroscopic ellipsometry. The plot of the ψ and Δ values for this analysis at four wavelengths (400, 600, 800, and 989 nm) are shown in Figure A1.11. The flat responses here suggest that significant changes are not taking place in this material. Now that this preliminary stability test has been completed, other more challenging ones can be contemplated.

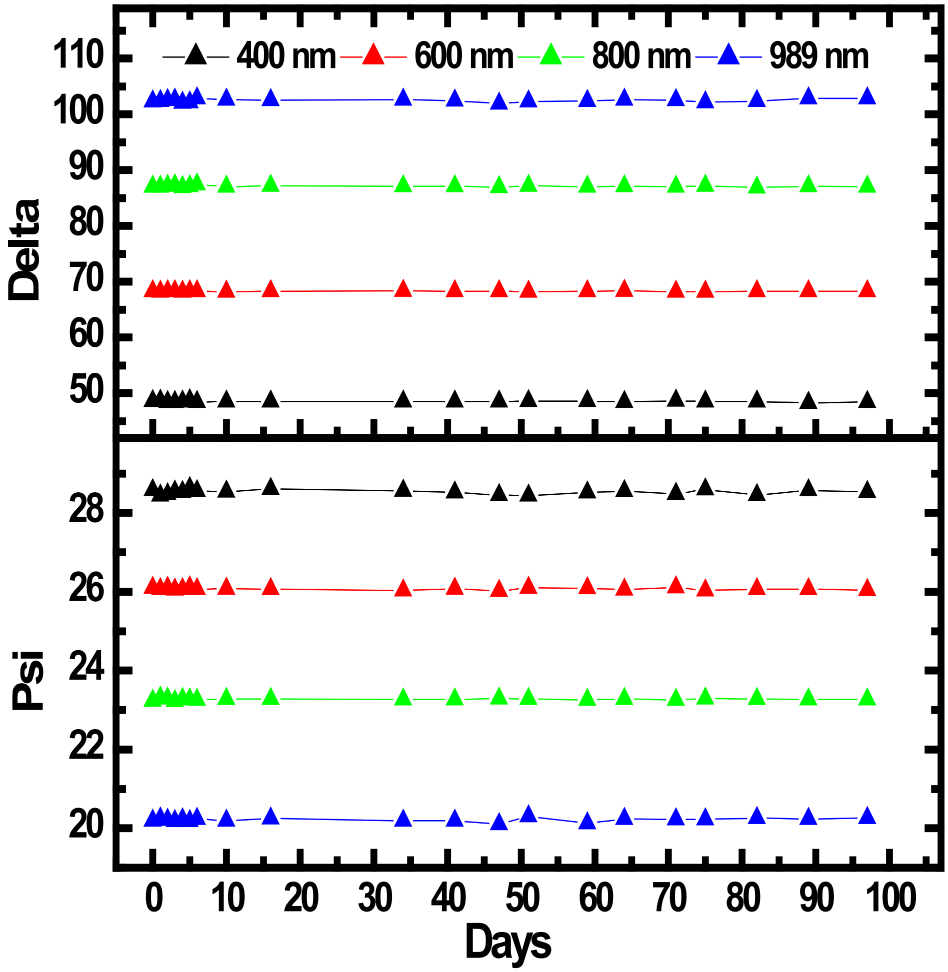

Figure A1.11 Values of ψ and Δ plotted at four different wavelengths taken over the course of ca. 100 days from a sputtered bismuth-tellurium-selenium film.

A1.3 Conclusions

The simple monitoring of ψ and Δ is a straightforward way of studying many material processes. If ψ and Δ change, one generally assumes that a change is taking place within one's material, and vice versa.

A1.4 References

1. Vedam, K. *Thin Solid Films* **1998,** *313*, 1-9.
2. Tompkins, H. G.; Tasic, S.; Baker, J. *Surf. Interface Anal.* **2000,** *29* (3), 179-187.
3. Langereis, E.; Heil, S.; Knoops, H.; Keuning, W.; Van de Sanden, M.; Kessels, W. *J. Phys. D: Appl. Phys.* **2009,** *42* (7), 073001.
4. McGahan, W. A.; Johs, B.; Woollam, J. A. *Thin Solid Films* **1993,** *234* (1–2), 443-446.
5. Jiang, X.; Wang, H.; Qi, J.; Willis, B. G. *J. Vac. Sci. Technol., A* **2014,** *32* (4), 041513.
6. Yamada, Y.; Tajima, K.; Okada, M.; Tazawa, M.; Roos, A.; Yoshimura, K. *Thin Solid Films* **2011,** *519* (9), 2941-2945.
7. Abbott, J.; Niederhauser, T. L.; Hansen, D. P.; Perkins, R. T.; Bell, D. A.; Bard, E. C.; Lunt, B. M.; Worthington, M. O.; Miller, C. M.; Hyatt, D. F. *ACS Appl. Mater. Interfaces* **2010,** *2* (8), 2373-2376.
8. Wang, H.; Lunt, B. M.; Gates, R. J.; Asplund, M. C.; Shutthanandan, V.; Davis, R. C.; Linford, M. R. *ACS Appl. Mater. Interfaces* **2013,** *5* (17), 8407-8413.
9. Pearson, A.; Jamieson, S.; Linford, M.; Lunt, B.; Davis, R. *Nanotechnology* **2013,** *24* (13), 135202.
10. Wang, H.; Madaan, N.; Bagley, J.; Diwan, A.; Liu, Y.; Davis, R. C.; Lunt, B. M.; Smith, S. J.; Linford, M. R. *Thin Solid Films* **2014**, 569, 124-130.

Appendix 2 An Introduction to Classical Least Squares (CLS) and Multivariate Curve Resolution (MCR) as Applied to UV-VIS, FTIR, and ToF-SIMS

A2.1 Abstract

Correct analysis of acquired data to extract information is critical in every field of science. In this chapter, I will discuss in detail two commonly used data analysis tools: classical least squares (CLS) and multivariate curve resolution (MCR). I will also review examples from the literature where these analysis tools were helpful in obtaining useful information from data.

A2.2 Introduction to Chemometrics

Chemometrics is the branch of analytical chemistry that deals with the statistical analysis of data. It includes all sorts of interesting tools for smoothing data, removing baselines, peak recognition, peak fitting, recognizing patterns, categorizing data, etc. Different disciplines have different names for these tools. When the same statistical methods are applied to biological data, the field is called bioinformatics. Regardless of what we call them, these analyses/tools show up in a number of areas of science and engineering, including in surface and material analysis – they can be helpful for getting the most information possible out of one's data. Ultraviolet-visible (UV-VIS) absorption spectroscopy is a useful tool for studying materials. I'll use our discussion of UV-VIS as a springboard for discussing and explaining two important data analysis tools: classical least squares (CLS) and multivariate curve resolution (MCR). Of course there are other very important tools that can also be applied to data analysis. Two of these are principal components analysis (PCA) and cluster analysis. Here, I'll give an example from research performed in the Linford lab of how CLS provided useful insights into the Fourier transform infrared (FTIR) spectra of some hydrogen- and deuterium-terminated diamond particles that had been functionalized.[1] I'll then provide examples of how MCR has provided insight into surface/material data. In particular, MCR has been rather extensively used to analyze time-of-flight secondary ion mass spectrometry (ToF-SIMS) and FTIR images.

A2.3 Ultraviolet-Visible (UV-VIS) Spectroscopy

A common problem in analytical chemistry is the determination of the concentration of an analyte (molecule of interest) in a solution. This is often done by ultraviolet-visible (UV-VIS) absorption spectroscopy using Beer's law:

$$A = \epsilon bc \tag{A2.1}$$

where A is the absorbance of the analyte, ε is its molar absorptivity, b is the path length of the light through the solution, and c is the concentration of the analyte. Notice in Equation A2.1 that the absorption of light, A, by the analyte is directly proportional to the three quantities just mentioned: molar absorptivity (a constant for the molecule of interest or material), path length, and concentration. Obviously there could be more than one analyte in the solution. Typically, the solvent in which the analytes are dissolved is chosen to be transparent over the range of wavelengths of interest for the analysis. Water is transparent to visible light and well into the UV, so it is commonly used in many UV-VIS analyses.

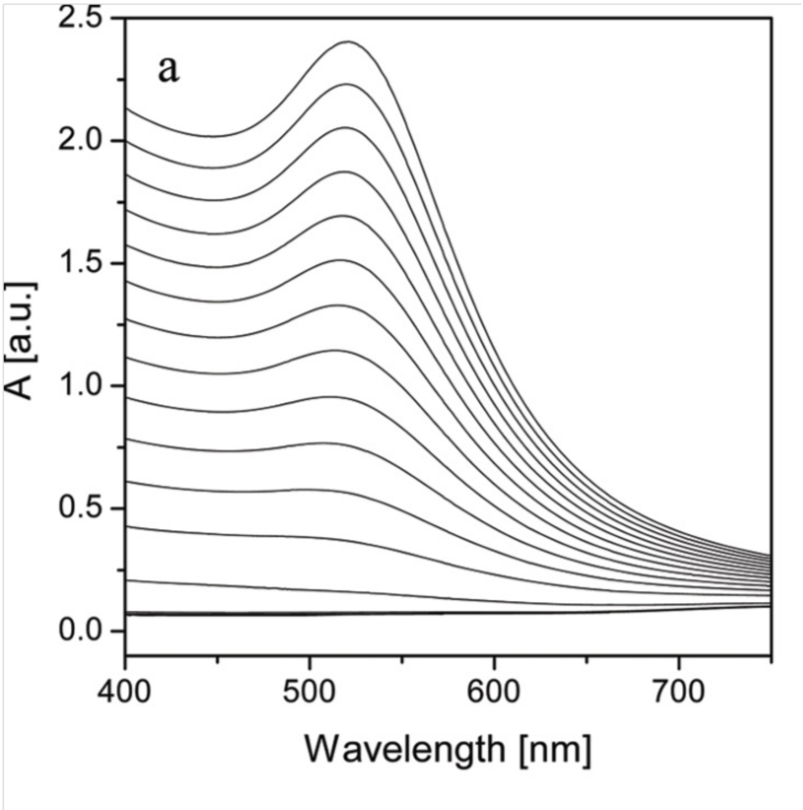

Figure A2.1 UV-VIS spectra (absorbance vs. wavelength) taken at 10 minute intervals of a reaction mixture containing growing gold nanoparticles. The particles were prepared from a gold precursor: chloro gold(I)-triphenylphosphine and a borane reductant with dodecanethiol present as a stabilizer. Reprinted (adapted) with permission from ("In Situ UV/Vis, SAXS, and TEM Study of Single-Phase Gold Nanoparticle Growth" by Hilmar Koerner, Robert I. MacCuspie, Kyoungweon Park, and Richard A. Vaia in *Chem. Mater.*, 2012, *24* (6), pp 981–995) Copyright (2012) American Chemical Society.

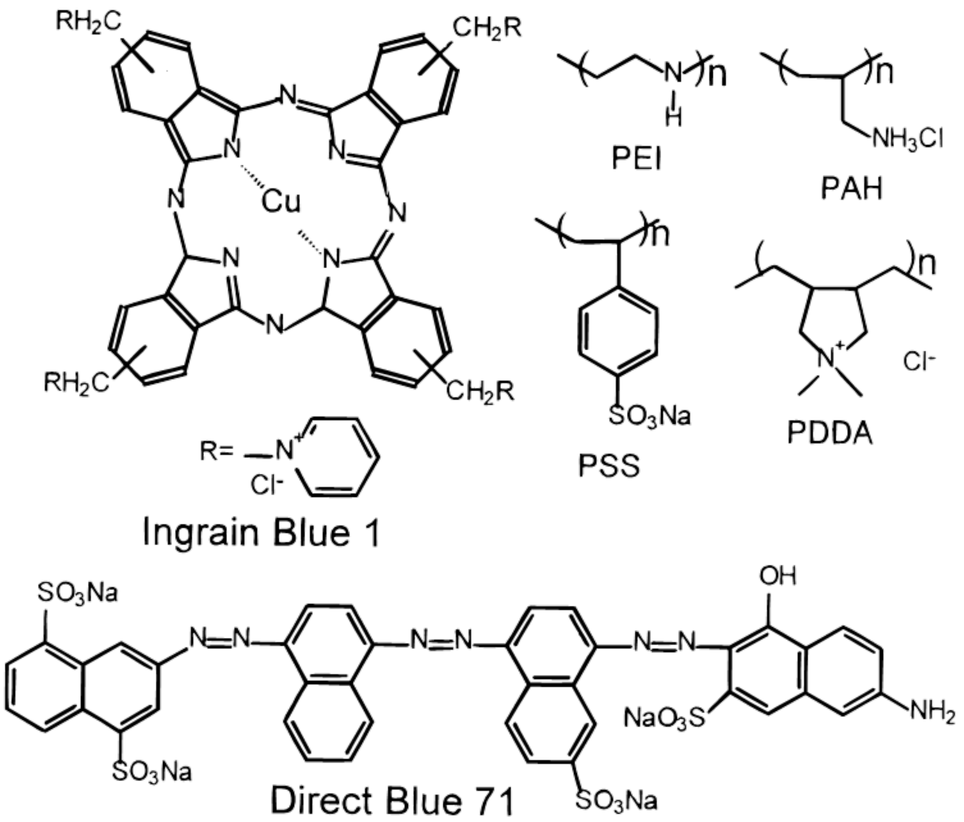

Figure A2.2 “Molecular structures of copper phthalocyanine dye (Ingrain Blue 1), poly(ethylenimine) (PEI), poly(allylamine hydrochloride) (PAH), poly(styrenesulfonate sodium salt) (PSS), poly(diallyldimethylammonium chloride) (PDDA), and Direct Blue 71.” Reprinted (adapted) with permission from (“Nonmonotonic Effect of Ionic Strength on Surface Dye Extraction during Dye-Polyelectrolyte Multilayer Formation” by Matthew R. Linford, Mark Auch, and Helmuth Möhwald in J. Am. Chem. Soc. 1998, 120, 178-182). Copyright (1998) American Chemical Society.

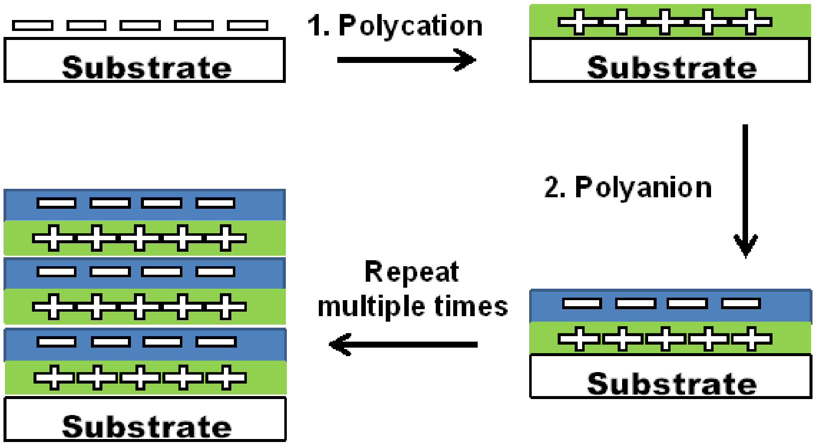

Figure A2.3 A general depiction of the layer-by-layer deposition of polyelectrolytes on surfaces starting with a negatively charged substrate and proceding through the sequential and repeated deposition of a polycation and a polyanion. The surface charge flips with the deposition of each polyelectrolyte.

UV-VIS spectroscopy has been used to characterize polyelectrolyte multilayers. In general, polyelectrolytes are water soluble polymers that contain a multiplicity of either cationic (positively charged) or anionic (negatively charged) groups. Interestingly, it is possible to deposit them in a sequential and self-limiting fashion on surfaces. For example, fused silica (amorphous SiO_2) has a negative charge in solution because of the presence of acidic SiOH groups at its surface. Accordingly, if a fused silica surface is immersed in an aqueous solution that contains a polycation (a positively charged polymer), the polycation will spontaneously adsorb to the silica surface. Clearly this adsorbtion is driven by electrostatic interactions between the surface and the polycation. Figure A2.2 shows three common polycations: PEI, PAH, and PDDA. Note that the degree to which PEI and PAH are charged depends on the solution pH. Now, an interesting phenomenon takes place during the adsorption of a polyelectrolyte. In the case under consideration here, the polycation adsorbs to the negatively charged fused silica surface and in this process changes (flips) the charge on the surface. That is, after adsorption of the polycation, the surface will have a positive charge. Now, once a layer of a polycation has adsorbed onto the anionic surface, the remaining polycations in solution will be repelled from this surface. Thus, the adsorption of the polycation is self-limiting. Typically, about a nanometer of polymer is adsorbed in such a deposition cycle, although the actual degree of adsorption can be controlled to some degree, e.g., by addition of a salt to the solution to screen the charges on the polyelectrolyte so that thicker films are deposited. Now, a negatively charged polymer (a polyanion) can be allowed to adsorb at the positively charged surface. Its adsorption again flips the surface charge so that the surface becomes negatively charged. The PSS shown in Figure A2.2 is an example of a common polyanion. This process (see Figure A2.3) continues with the subsequent immersion of the surface in a solution of a polycation. Complex and interesting materials can be built up in this manner.

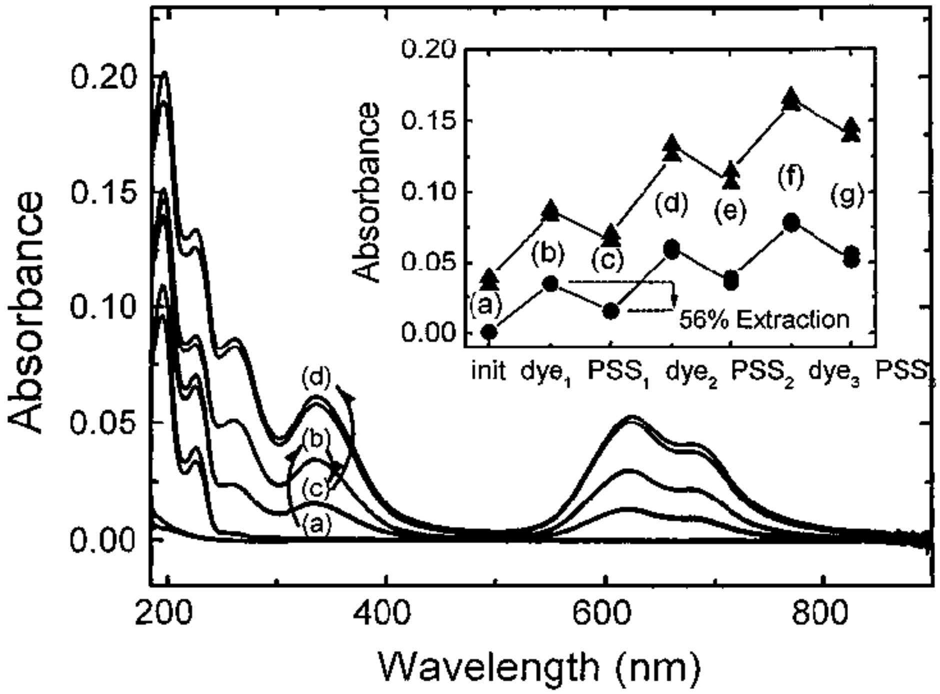

Figure A2.4 UV-VIS absorption spectra of fused silica surfaces coated sequentially with (a) PEI (lower two spectra) followed by PSS (upper two spectra), (b) Ingrain Blue 1, (c) PSS, (d) Ingrain Blue 1, (e) PSS, (f) Ingrain Blue 1, and (g) PSS. The inset shows absorbances of the spectra at 225 nm (triangles) and 335 nm (circles). Reprinted (adapted) with permission from ("Nonmonotonic Effect of Ionic Strength on Surface Dye Extraction during Dye-Polyelectrolyte Multilayer Formation" by Matthew R. Linford, Mark Auch, and Helmuth Möhwald in J. Am. Chem. Soc. 1998, 120, 178-182). Copyright (1998) American Chemical Society.

The adsorption of a multiply charged molecule in the place of one of the polyelectrolytes typically used in a layer-by-layer deposition has been studied.[2] For example, the polycation in a layer-by-layer deposition has been replaced with a dye with four permanent positive charges (Ingrain Blue 1, see Figure A2.2). The polyanion in this deposition was PSS. Both PSS and Ingrain Blue 1 show strong UV-VIS absorbance, so their adsorption could be followed by UV-VIS. The UV-VIS spectra in Figure A2.4 illustrate the somewhat unexpected results that were obtained. Fused silica substrates were initially immersed in PEI, which is cationic polymer that created a positive charge on the surface. PEI has a high affinity for this glass. The bottom two spectra in Figure A2.4 (below the '(a)' label) correspond to this PEI layer. This film is beginning to absorb a little light around 200 nm. Eventually, all organic molecules will absorb UV light if the wavelength of the light gets short enough. PSS was then allowed to adsorb to this surface. The aromatic rings in PSS absorb UV light well. The resulting spectra from this surface are also shown below the '(a)' label in the figure. As expected, PSS shows considerable absorption of light around 200 nm. The surface was then immersed in a solution of Ingrain Blue 1. This dye adsorbed nicely to the surface as evidenced by the UV-VIS spectra labeled '(b)'. Here, absorbances were also observed for the first time in the visible part of the spectrum (between about 550 and 750 nm), which is consistent with the dye being colored. However, when this dye-terminated surface was immersed in a solution of PSS, the absorbance of the thin film dropped (spectra labeled '(c)'). In this study it became clear that the PSS was not depositing in exactly the expected fashion. Rather it would extract a fraction of the dye at the surface during its deposition. When this PSS-terminated surface was then placed again in a solution of the dye, the absorbance rose significantly (see spectra labeled '(d)'), indicating that dye was sticking to this surface. This type of deposition continued, leading to the ‘sawtooth’ type growth observed in the inset to Figure A2.4. In other words, thin films of Ingrain Blue 1 and PSS could be deposited, but it was ‘two steps forward, one step back’ with a fraction of the Ingrain Blue 1 lost with each PSS deposition.

A2.4 Classical Least Squares (CLS)

As suggested in Figures A2.1 and A2.4, the molar absorptivity of an analyte/species of interest will not be the same at all wavelengths of light, λ. In other words, there may be wavelengths of light passing through a solution or material that the analyte absorbs strongly and others where little, if any, absorption occurs. Accordingly, the molar absorptivities at the different wavelengths under consideration could be written as:

$$A_{200} = \epsilon_{200} bc \qquad \text{(A2.2)}$$

$$A_{201} = \epsilon_{201} bc$$

$$A_{202} = \epsilon_{202} bc$$

…

where, for example, A_{200} is the absorbance of our material at 200 nm and ε_{200} is the molar absorptivity of the material at that same wavelength. Obviously the path length and analyte concentration are the same at all the wavelengths. Alternatively, and more concisely, all of the absorbances and molar absorptivities in Equation A2.2 could be represented as:

$$A_{\lambda} = \epsilon_{\lambda} bc \qquad \text{(A2.3)}$$

Because many UV-VIS peaks are broad (see again Figures A2.1 and A2.4), collecting data at every integer value of the wavelength of light will usually be sufficient to map out one’s peaks. It should also be pointed out that in practice the linearity of the above equation will begin to break down when the absorbance of the solution/material is too high, i.e., it is assumed here that low enough concentrations of the analytes are used so that this will not be an issue.

If the solution contains more than one analyte, and if they are noninteracting, which will often be a good approximation, Beer's law can be expanded as follows:

$$A_\lambda = \epsilon_{\lambda,1} b c_1 + \epsilon_{\lambda,2} b c_2 \tag{A2.4}$$

where $\epsilon_{\lambda,1}$ is the molar absorptivity of analyte 1 and $\epsilon_{\lambda,2}$ is the molar absorptivity of analyte 2. As might be expected, this equation can be generalized to include a series of analytes:

$$A_\lambda = \sum_i \epsilon_{\lambda,i} b c_i \tag{A2.5}$$

To illustrate the use of classical least squares in spectral analysis, I introduce here some mock spectra that will be analyzed (see Figure A2.5). They were made in MATLAB by combining Gaussians of different widths and heights. I will assume that each represents the UV-VIS spectrum of a different imaginary analyte. I'll call the blue line from Figure A2.5 Spectrum 1 (from an imaginary analyte 1) and the green line Spectrum 2 (from imaginary analyte 2). I'll assume that these spectra were taken at a standard concentration, which I'll take here to be 1.0 M. Next I'll assume that the pathlength of the light is 1.0 cm, which is a common value for UV-VIS solution measurements. The consequence of c = 1.0 M and b = 1.0 cm in Equation A2.3 is that the spectra (absorbances, $A(\lambda)$) in Figure A2.5 are equal to the molar absoptivities, $\varepsilon(\lambda)$, for their respective compounds. Absorbance itself has no units, so the units on molar absorptivities are cm^{-1} M^{-1}.

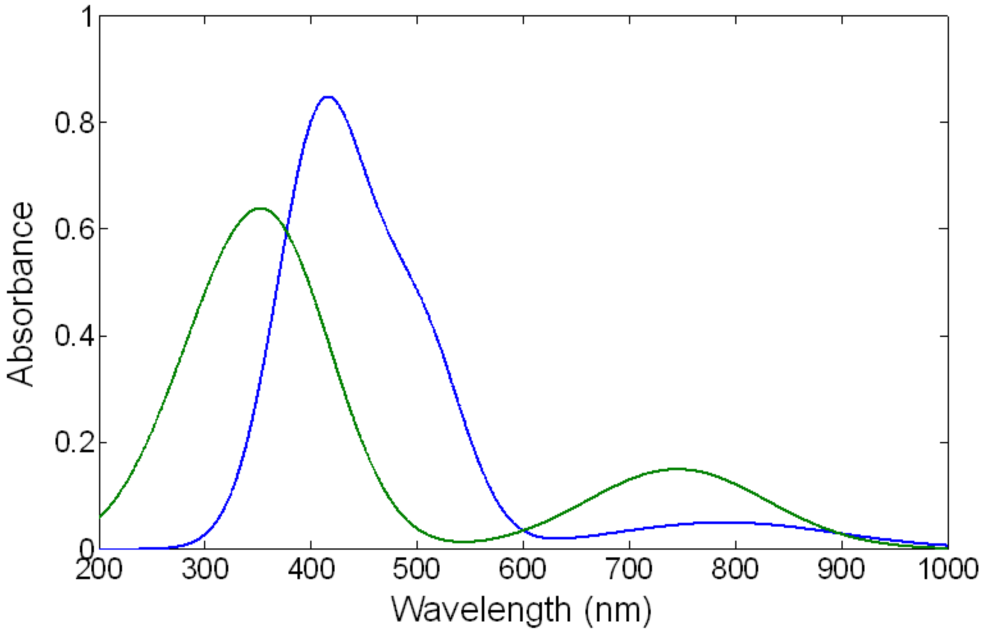

Figure A2.5 Mock spectra of two analytes. ‘analyte 1’ is represented by the blue line (maximum around 420 nm) and ‘analyte 2’ is represented by the green line (maximum around 330 nm).

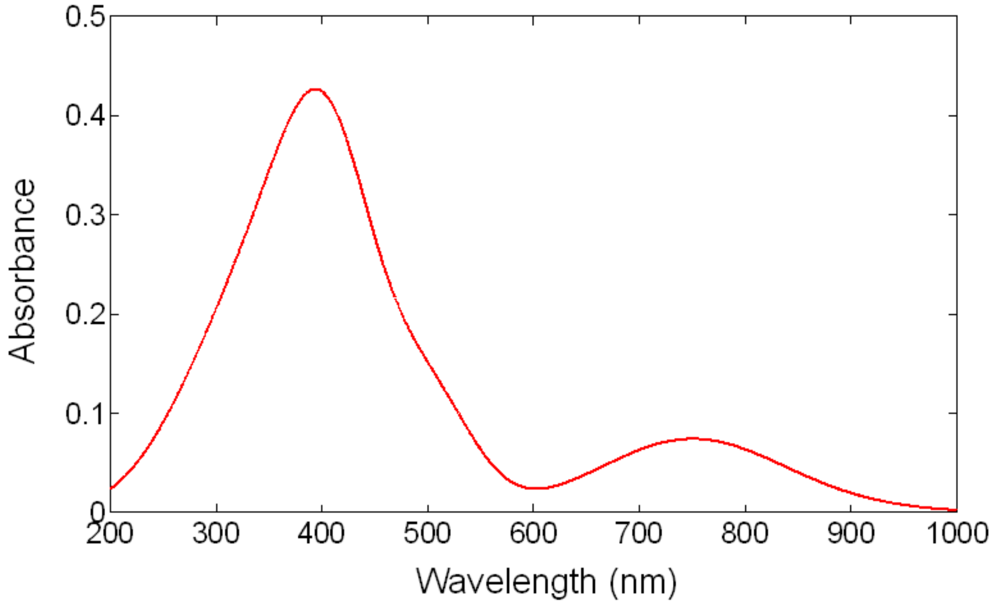

Figure A2.6 Mock, ‘unknown’ spectrum consisting of absorptions of analyte 1 (0.28 M) and analyte 2 (0.41 M).

Consider a solution that is a mixture of analytes 1 and 2. Its UV-VIS absorption spectrum is then measured to obtain the spectrum shown in Figure A2.6. The question now is this: given the pure component spectra in Figure A2.5, how could we determine the concentrations of analytes 1 and 2 that gave us the spectrum in Figure A2.6? This problem is formulated in terms of matrix algebra, where the absorbance of the two-component mixture can be described as:

$$A_\lambda = \epsilon_{\lambda,1} c_1 + \epsilon_{\lambda,2} c_2 \tag{A2.6}$$

which is equivalent to:

$$\begin{bmatrix} A_{200} \\ A_{201} \\ A_{202} \\ \vdots \\ A_{799} \\ A_{800} \end{bmatrix} = \begin{bmatrix} \varepsilon_{200,1} \\ \varepsilon_{201,1} \\ \varepsilon_{202,1} \\ \vdots \\ \varepsilon_{799,1} \\ \varepsilon_{800,1} \end{bmatrix} c_1 + \begin{bmatrix} \varepsilon_{200,2} \\ \varepsilon_{201,2} \\ \varepsilon_{202,2} \\ \vdots \\ \varepsilon_{799,2} \\ \varepsilon_{800,2} \end{bmatrix} c_2 \tag{A2.7}$$

That is, the total absorption of the solution at each wavelength is equal to the sum of the molar absorptivity for each pure compound multiplied by its respective concentration. Now, these two equations can be combined together as follows:

$$\begin{bmatrix} A_{200} \\ A_{201} \\ A_{202} \\ \vdots \\ A_{799} \\ A_{800} \end{bmatrix} = \begin{bmatrix} \varepsilon_{200,1} & \varepsilon_{200,2} \\ \varepsilon_{201,1} & \varepsilon_{201,2} \\ \varepsilon_{202,1} & \varepsilon_{202,2} \\ \vdots & \vdots \\ \varepsilon_{799,1} & \varepsilon_{799,2} \\ \varepsilon_{800,1} & \varepsilon_{800,2} \end{bmatrix} \begin{bmatrix} c_1 \\ c_2 \end{bmatrix} \tag{A2.8}$$

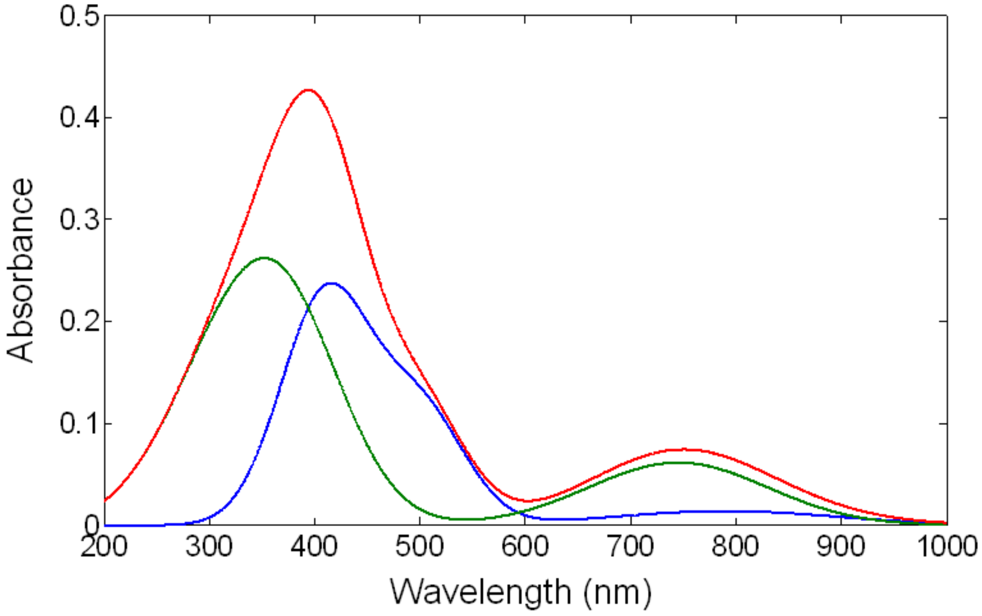

Figure A2.7 Red line: unknown spectrum from Figure A2.6. Blue 1: spectrum of analyte 1 from Figure A2.5 multiplied by 0.28. Green line: spectrum of analyte 2 from Figure A2.5 multiplied by 0.41.

Of course Equation A2.8 can be easily solved – it is a rather straightforward matrix algebra problem. However, to better understand CLS it will be written as:

$$\mathbf{a} = \mathbf{Ec} \tag{A2.9}$$

where **a** is the column vector of absorbance values in Equation A2.8 that has dimensions of 801 x 1, i.e., one data point is being taken at each wavelength between 200 and 1000 nm. **E** refers to the 801 x 2 matrix filled with the molar absorptivities for analytes 1 and 2, and **c** stands for the 2 x 1 column vector containing the two concentrations. At this point I'm switching to the convention used in linear algebra: bold capital letters refer to matrices, lower case bold letters refer to column vectors, and lower case italic letters refer to scalars.

Now, **c** is unknown in Equation A2.9 and it is desirable to solve for it. Ideally, both sides of Equation A2.9 would be left multiplied by the inverse of **E** to get **c** alone on the right side of the equation. However, **E** is clearly not a square matrix and only square matrices have inverses. The trick here is to recognize that multiplication of a matrix by its transpose yields a square matrix, and the product of a matrix with its transpose (a square matrix) may have an inverse. Thus, assuming $\mathbf{E}^{\mathrm{T}}\mathbf{E}$ has an inverse, I proceed as follows:

$$\mathbf{E}^{\mathrm{T}}\mathbf{a} = \mathbf{E}^{\mathrm{T}}\mathbf{Ec} \tag{A2.10}$$

$$(\mathbf{E}^{\mathrm{T}}\mathbf{E})^{-1}\mathbf{E}^{\mathrm{T}}\mathbf{a} = (\mathbf{E}^{\mathrm{T}}\mathbf{E})^{-1}\mathbf{E}^{\mathrm{T}}\mathbf{Ec} \tag{A2.11}$$

$$(\mathbf{E}^{\mathrm{T}}\mathbf{E})^{-1}\mathbf{E}^{\mathrm{T}}\mathbf{a} = \mathbf{Ic} \tag{A2.12}$$

$$\mathbf{c} = (\mathbf{E}^{\mathrm{T}}\mathbf{E})^{-1}\mathbf{E}^{\mathrm{T}}\mathbf{a} \tag{A2.13}$$

The calculations that correspond to Equation A2.13 were performed in MATLAB. Here, the spectrum in Figure A2.6 was taken as the matrix **a**, the spectra in Figure A2.5 as the pure component spectra, which provided the matrix **E**, and calculated **c**. For **c**, values of 0.28 for component 1 and 0.41 for component 2 were obtained. The spectrum in Figure A2.6 was created by adding together *exactly* these amounts of analytes 1 and 2, so the theory is self-consistent to this point. Figure A2.7 shows the unknown spectrum, along with component 1 multipled by 0.28 and component 2 multiplied by 0.41.

Arguably, the problem I just solved wasn't much of a challenge for the theory. The 'unknown' spectrum was made by adding together two pure component spectra. There was no noise, no extraneous peaks from unknowns, no distortions of the baseline, no offset, etc. The situation was perfect. I'll make things a little more complex to show that CLS is pretty robust. To the unknown and pure component spectra in Figures A2.5 and A2.6, noise at a level corresponding to about ± 5% of the maximum signal in the unknown spectrum was added. The new, moderately noisy spectra are shown in Figure A2.8. The noise level on these spectra is higher than in many of the UV-VIS spectra I have worked with (compare the noise level in these spectra to those in Figures A2.1 and A2.4), so this is a fairly reasonable challenge for CLS. Now, using CLS to fit the noisy pure component spectra in Figure A2.8 to the noisy unknown spectrum that is also in Figure A2.8, contributions of component 1 and 2 to the unknown spectrum of 0.2794 and 0.4118, respectively, were found. Obviously these values round to the previous ones that were obtained with the 'perfect' spectra in Figures A2.5 and A2.6 (0.28 and 0.41). CLS does very well here. Now, things can be taken one step further by doubling the amount of noise in the spectra (see noisier spectra in Figure A2.9). When CLS is run on these spectra (pure components and 'unknown') contributions of component 1 and 2 to the unknown spectra of 0.2798 and 0.4071, respectively, are obtained. These results remain solid. Thus, CLS is not strongly affected by the noise in these spectra, and it appears to be a rather robust technique for this type of data analysis. In the literature you can find more extensive explorations of the parameters that influence CLS – noise, extraneous peaks, baseline offsets, etc.[3]

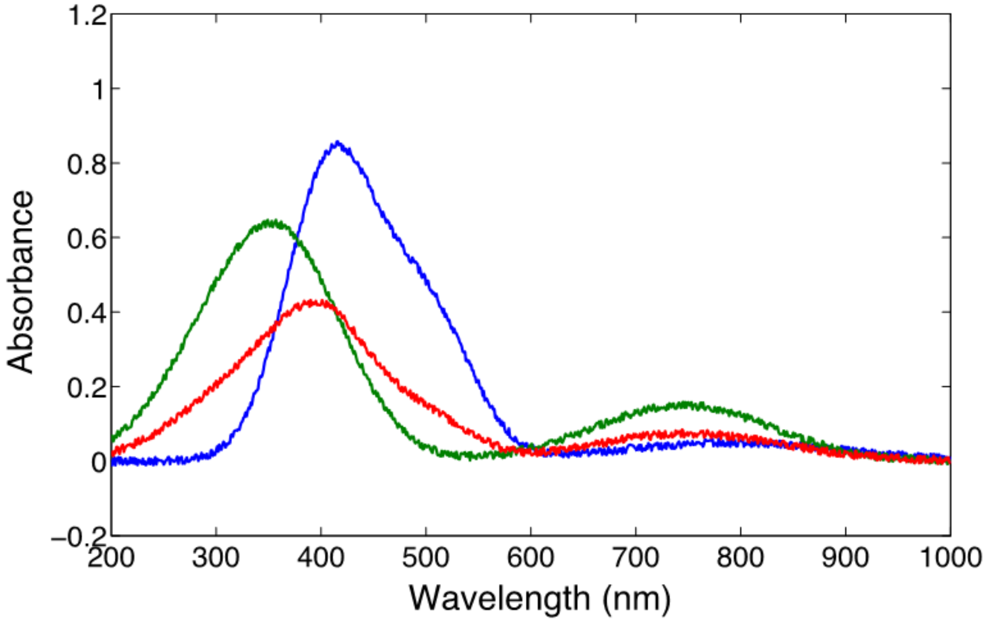

Figure A2.8 The pure component spectra in Figure A2.5 (blue and green lines) and the unknown spectrum in Figure A2.6 (red line) with added noise.

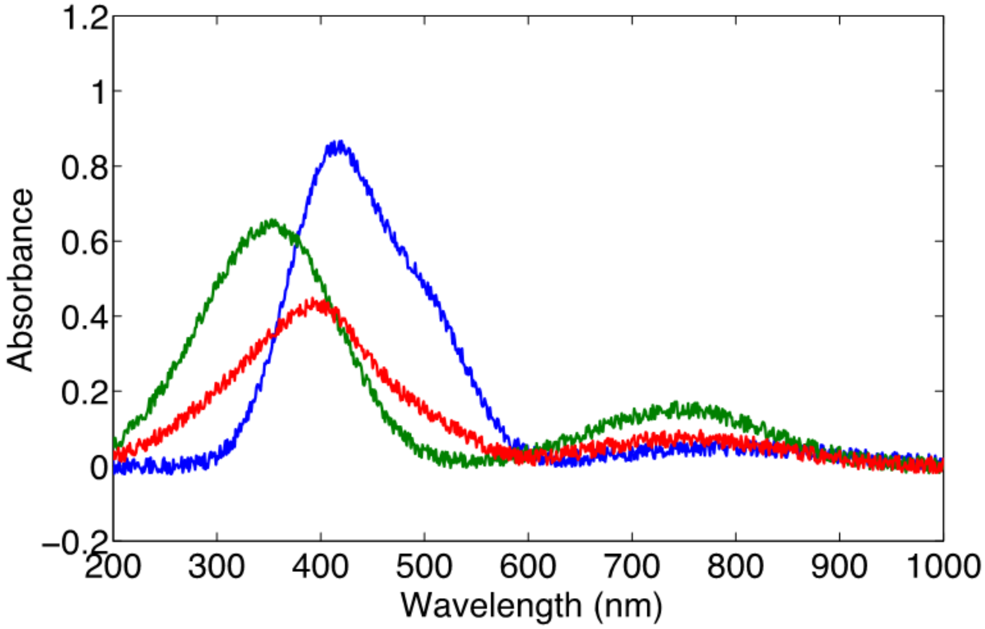

Figure A2.9 The pure component spectra in Figure A2.5 (blue and green lines) and the unknown spectrum in Figure A2.6 (red line) with twice the noise in Figure A2.8.

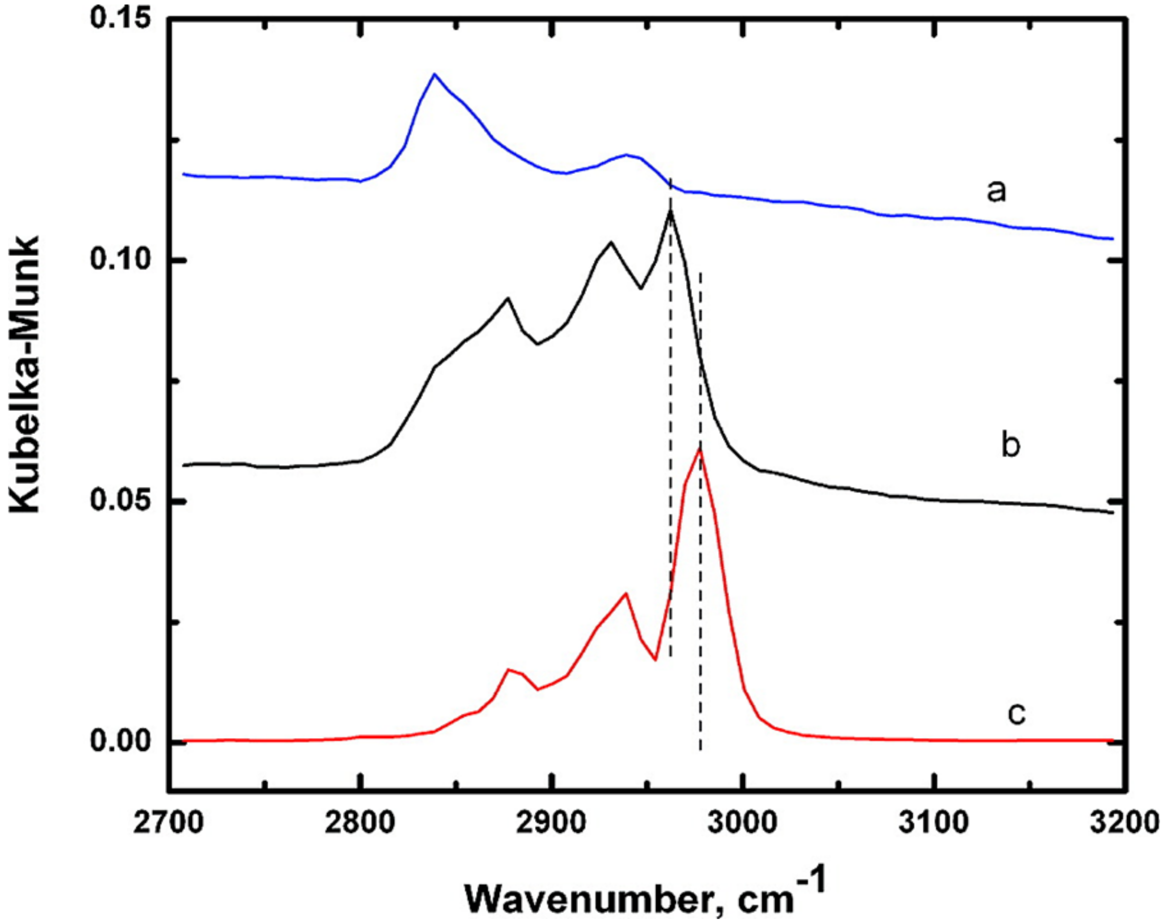

Figure A2.10 DRIFT of (a) hydrogen-terminated diamond particles, (b) hydrogen-terminated diamond after treatment with di-tert-amyl peroxide for 24 h at 130 °C, (c) pure di-tert-amyl peroxide. Reprinted with permission from ("Functionalization of Deuterium- and Hydrogen-Terminated Diamond Particles with Mono- and Multilayers of Di-tert-amyl Peroxide and Their Use in Solid Phase Extraction" by Li Yang, Michael A. Vail, Andrew Dadson, Milton L. Lee, Matthew C. Asplund, and Matthew R. Linford in *Chemistry of Materials* 2009, *21*, 4359-4365.) Copyright (2009) American Chemical Society.

A2.4.1 An Example of Surface/Material Analysis with CLS

A few years ago the Linford group became interested in the chemical functionalization of diamond.[1] To create a well defined starting material for this work, they reduced diamond particles in heated (900 °C), flowing 5 – 6% H_2 or D_2 in argon. This relatively low concentration of hydrogen or deuterium in an inert gas is known as forming gas. The hydrogen/deuterium-terminated diamond particles produced with this procedure were exposed to heated di-tert-amylperoxide (DTAP). DTAP, a peroxide, has a relatively weak O-O bond. It was believed that upon heating, the molecule breaks at this bond to form a reactive, oxygen-centered radical. This species in turn would be expected to react with the diamond surface and deposit on it. Thus, a monolayer of DTAP fragments would be expected to deposit on the diamond. With longer deposition times, thicker films might be obtained.

FTIR probes the vibrational modes of molecules. It can be a powerful tool for understanding organic materials. Fourier transform infrared (FTIR) spectra of hydrogen-terminated diamond particles, pure DTAP, and hydrogen-terminated diamond particles reacted with DTAP were collected. The C-H stretching region (around 3000 cm^{-1}) of these spectra is shown in Figure A2.10. Here, the spectrum of the hydrogen-terminated diamond primarily shows two peaks, the DTAP shows three, and the spectrum of the functionalized surface appears to be, more or less, a mixture of these two spectra. To better understand functionalized materials, CLS was performed on their spectra using the spectra of the DTAP and hydrogen-terminated diamond as the pure component spectra. Interestingly, it was found that the spectrum of the DTAP-functionalized diamond could not be adequately described by CLS using these pure component spectra. Only part of the spectrum of the functionalized material could not be adequately explained using a linear combination of the other two spectra. This surprising result caused us to perform a series of first principles calculations of DTAP fragments on carbon clusters. These calculations suggested that a DTAP fragment attached to diamond would show a shift in its FTIR spectrum. The shift predicted by these calculations was in agreement with the shift found in the FTIR spectra of the functionalized diamond, which provided additional evidence for surface functionalization of our hydrogen-terminated diamond with DTAP. Thus, CLS played an important role in our fundamental understanding of these materials.

A2.5 Multivariate Curve Resolution (MCR)

Fundamentally, CLS involves the fitting of an unknown spectrum to pure component spectra. But now let's consider a more complicated, and also all too realistic, scenario. Suppose there is a series of complex spectra and one does not know the pure component spectra from which they are made. This situation arises very frequently in ToF-SIMS imaging and depth profiling. Data sets of SIMS images and depth profiles can contain tens of thousands of spectra. Wouldn't it be nice if there were a way to figure out what the underlying 'pure component' spectra are for such complex set of spectra?

MCR addresses this issue. It is arguably much more powerful and much more interesting than CLS. To derive the governing equations of MCR, I'll start with a modified form of Equation A2.9.

$$\mathbf{A} = \mathbf{EC} \tag{A2.14}$$

Here I recognize that instead of dealing with a single column of numbers, **a**, which represent a single spectrum, I am dealing with a matrix, **A**, that contains hundreds, if not thousands, of spectra. Again, all I know here is **A**, where each column in **A** is one of the spectra in our data set. I am also dealing here with a matrix, **C**, which contains one column of concentrations for each spectrum in matrix **A**. **E**, of course, if the matrix that contains our pure component spectra.

Now, using the procedure outlined above, I solve Equation A2.14 for the two unknowns in it (**E** and **C**), obtaining:

$$\mathbf{C} = (\mathbf{E}^{\mathrm{T}}\mathbf{E})^{-1}\mathbf{E}^{\mathrm{T}}\mathbf{A} \tag{A2.15}$$

$$\mathbf{E} = \mathbf{A}\mathbf{C}^{\mathrm{T}}(\mathbf{C}\mathbf{C}^{\mathrm{T}})^{-1} \tag{A2.16}$$

Now, at this point you may be thinking that there is not enough information to proceed. Actually there is a way forward. It turns out that there are various approaches in chemometrics that have been developed to guess the pure component spectra in a set of unknown spectra. Using one of these methods, which should be part of the software program you'd be using to do MCR, a set of guesses for these pure component spectra is made. You can tell the software how many pure components you are looking for: 1, 2, 3, … These guesses are then made into a matrix, **E**, where each column represents one of the pure component spectra. You will notice that with these guesses it is now possible to solve Equation A2.15 for the concentrations (contributions) of the pure component spectra to the actual spectra. Now, with the concentrations obtained from Equation A2.15, Equation A2.16 can be solved. That is, by taking the values of **E** from Equation A2.16 and put them back into Equation A2.15. This process can be continued, taking the results from the previous equation and inserting it into the next equation – going back and forth solving Equations A2.15 and A2.16. If the initial guesses were reasonable and if the system is well behaved, the values of **C** and **E** will converge in this process, giving us the pure component spectra and their contributions (concentrations) for the set of unknown spectra. Thus, MCR can be a powerful approach for understanding the underlying variation in large sets of spectra.

It is probably worth mentioning here a few other important details about MCR. The first is the nonnegativity constraints placed on **E** and **C** in the algorithm. That is, in the iterative process of determining **E** and **C** from Equations A2.15 and A2.16, the mathematics of the problem may want to give negative values to elements in the **E** and **C** matrices. Obviously this is unphysical – one can't have negative concentrations or negative absorbances. Accordingly, MCR forbids any negative elements in **E** or **C**. Thus, the pure component spectra obtained from MCR look like real spectra, so its output is easier for the uninitiated to interpret than the results (scores and loadings) from principal components analysis (PCA). One final issue is that of determining the number of pure component spectra that belong to a data set, i.e., the software will generally give you as many pure components as you want so you will generally have to figure out how many are appropriate to keep. A plot of variation captured vs. number of pure components in the model can be helpful in determining the number to keep. Once a significant fraction of the variation in the original data set has been captured, it may be best not to consider any more pure components. The information from other analytical methods can also help justify the number of components to keep; other surface/material analyses may point to the number of components that should be present in the materials. Finally, it is a good idea to look at the pure component spectra generated by MCR to make sure that they seem chemically reasonable. Once they start looking like noise they may no longer describe any real chemical variation in your spectra.

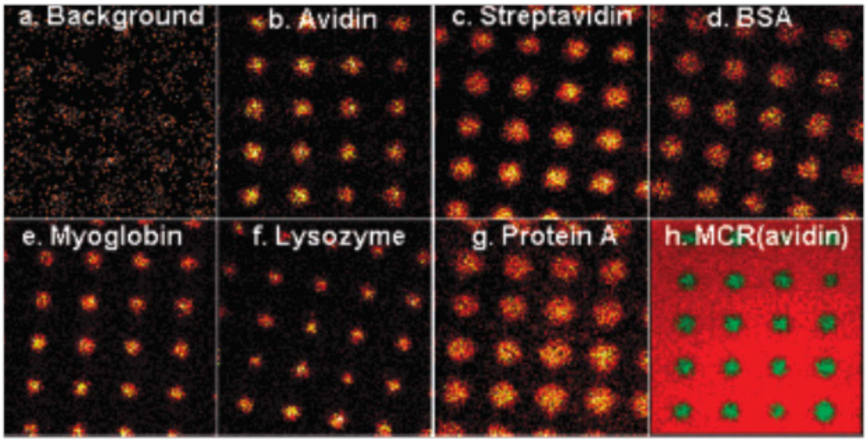

Figure A2.11 a. – g. TOF- SIMS negative ion, CN-, images. Panel a. image of a bioarray before protein adsorption. Panels b. – g. images after adsorption of various proteins. Panel h. results from an MCR analysis of the mass spectra from the avidin array. Reprinted (adapted) with permission from ("Direct Adsorption and Detection of Proteins, Including Ferritin, onto Microlens Array Patterned Bioarrays" by Feng Zhang, Richard J. Gates, Vincent S. Smentkowski, Sriram Natarajan, Bruce K. Gale, Richard K. Watt, Matthew C. Asplund, and Matthew R. Linford in J. AM. CHEM. SOC. 2007, 129, 9252-9253). Copyright (2007) American Chemical Society.

A2.5.1 Examples of Multivariate Curve Resolution

Microlens arrays are arrays of miniature lenses on a transparent substrate, where each lens in these optical elements may have dimensions of 10 – 100 μm. The lenses may be arranged (packed) in various patterns, e.g., square or hexagonal. A few years ago, the Linford lab at BYU used microlens arrays to prepare bioarrays.[4] The microlenses in these arrays were 100 μm across in a square pattern, which gave 10,000 lenses/cm^2 on these devices. To create the bioarrays, they began by functionalizing silicon surfaces with about a monolayer (15 Å) of a PEG (polyethylene glycol) silane: $(CH_3O)_3Si(CH_2)_3(OCH_2CH_2)_{6-9}OCH_3$. Silanes deposit/adsorb onto silica surfaces, and PEG has the interesting and important property of resisting protein adsorption.[5-6] To make the bioarrays, a microlens array was positioned above a PEG silane-terminated silicon surface and a 4 ns pulse of laser light was fired through it. In the areas where the light was focused by the microlenses, it burned away the PEG, leaving an exposed surface. Proteins would then selectively deposit into the 'wells' created by the laser. The presence of adsorbed proteins in the spots was confirmed by ToF-SIMS. Figure A2.11a shows a ToF-SIMS CN^- image of a microlens array patterned surface before its immersion in a solution of a protein. ToF-SIMS images are generated by taking a mass spectrum at every pixel in the image. The intensity of a signal of interest from these mass spectra is then plotted. In general, a lighter color in an image indicates higher peak intensity. Figures A2.11b – g are plots of the intensity of the CN^- ion from surfaces prepared by adsorption of different proteins in our microarrays. The CN^- ion is characteristic of nitrogen-containing organic materials, including proteins.[7] Clearly, protein adsorption took place preferentially in the wells generated by the focused laser.

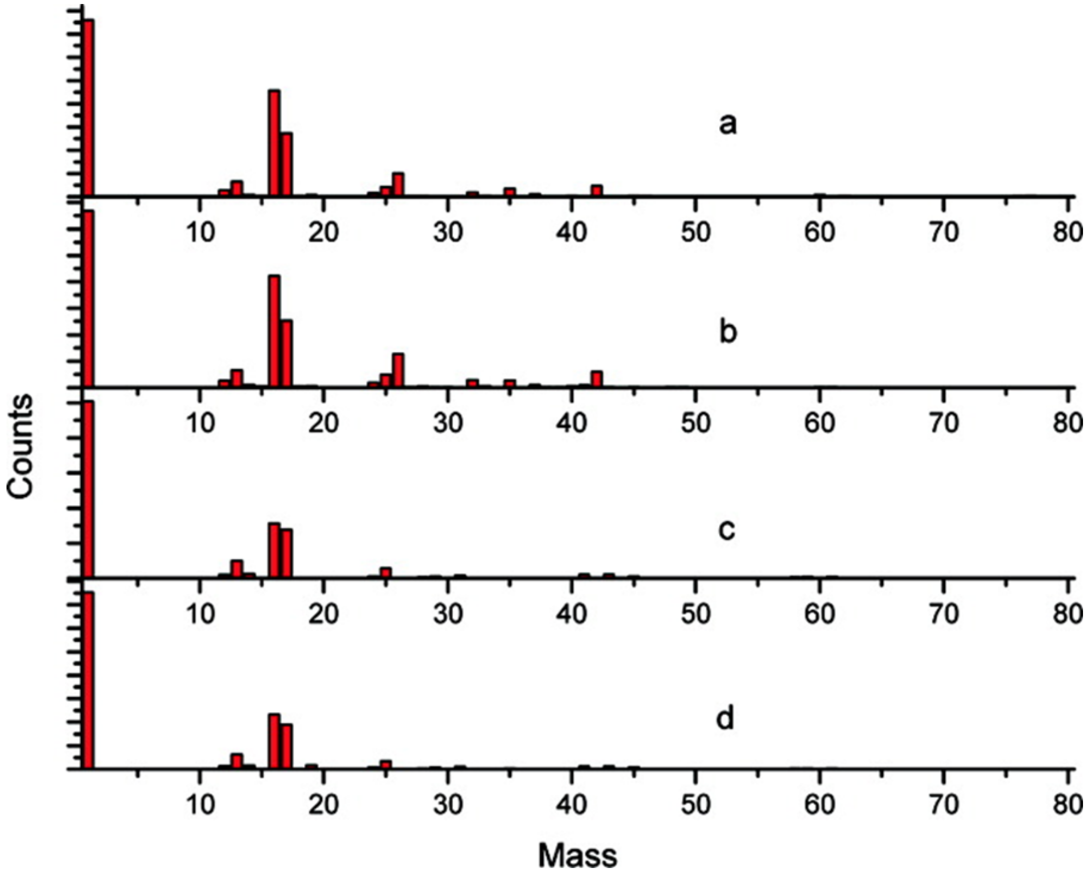

Figure A2.12 a. MCR component corresponding to the avidin spots in Figure A2.11h. b. ToF-SIMS spectrum of an avidin-coated, planar silicon surface. c. MCR component corresponding to the background to the avidin spots in Figure A2.11h. d. ToF-SIMS spectrum of a PEG silane on silicon. Reprinted (adapted) with permission from ("Direct Adsorption and Detection of Proteins, Including Ferritin, onto Microlens Array Patterned Bioarrays" by Feng Zhang, Richard J. Gates, Vincent S. Smentkowski, Sriram Natarajan, Bruce K. Gale, Richard K. Watt, Matthew C. Asplund, and Matthew R. Linford in J. AM. CHEM. SOC. 2007, 129, 9252-9253). Copyright (2007) American Chemical Society.

ToF-SIMS imaging is a powerful technique for understanding surface patterning. Clearly then, the amount of information in the CN^- images in Figure A2.11 is only a small fraction of the total information that was collected. In order to better consider all of this information, MCR was performed on the mass spectra in the SIMS images. In each case, the data could be well described by two components. The results from the adsorption of avidin in the bioarray are shown in Figure A2.11h, where green represents one component and red the other. To better understand these components, mass spectra were collected from the surfaces that they suspected would best represent them: a planar, homogeneous PEG silane-terminated surface and an unpatterned, unfunctionalized, native oxide terminated silicon surface to which avidin was allowed to adsorb. The comparison between the two components found by MCR and these mass spectra is shown in Figure A2.12. Figures A2.12a and A2.12b show the MCR component of the spots in the array and the spectrum from the planar silicon surface covered with avidin, respectively. The agreement between these spectra is extremely good. Figures A2.12c and A2.12d show the MCR component from the background of the array and a planar PEG-silane terminated surface, respectively. Again, the agreement is excellent. Clearly, the background of arrays stayed as PEG and protein adsorbed selectively in wells. Thus, MCR helped them understand their surface chemistry in a way that probably would not have been possible in a univariate fashion.

As a second example, Budevska and coworkers analyzed a biological material (corn kernel sections) by FTIR imaging.[8] Similar to the ToF-SIMS images discussed above, each pixel of their hyperspectral images corresponded to a complete spectrum. And, again, because of the immense amount of information that was collected in this analysis, they applied MCR to their spectra. Five MCR components were generated for one of their images, along with false color images that showed the regions of the image where these components best explained the variation in the spectra. The considerable differences between these false color images suggested a high degree of heterogeneity in their sample. They compared their MCR components to spectra from pure materials found in a spectral library. MCR components 1, 2, and 5 had characteristic features of carbohydrates. In particular, MCR component 5 very closely matched the spectrum of starch. MCR component 4 had almost exactly the same spectrum as zein (a protein from corn). Thus, this MCR analysis helped them understand the distribution and nature of the chemical species in their complex sample. In contrast, a spectrum-by-spectrum analysis of their huge data set would have been challenging. For a more detailed description of MCR, the reader is referred to a review article by Anna de Juan and Romà Tauler.[9]

A2.6 Conclusions

The statistical analysis of data can provide valuable insights into complex data sets. Classical least squares (CLS) is a straightforward techinque. It can be well applied when one has a relatively simple mixture and the spectra of its components are known. MCR is a more powerful tool for understanding multivariate data. It can be applied to a complex data set even when no information is available initially about its pure components.

A2.7 References

1. Yang, L.; Vail, M. A.; Dadson, A.; Lee, M. L.; Asplund, M. C.; Linford, M. R. *Chem. Mater.* **2009,** *21* (19), 4359-4365.

2. Linford, M. R.; Auch, M.; Möhwald, H. *J. Am. Chem. Soc.* **1998,** *120* (1), 178-182.

3. Kramer, R., *Chemometric techniques for quantitative analysis*. CRC Press: 1998.

4. Zhang, F.; Gates, R. J.; Smentkowski, V. S.; Natarajan, S.; Gale, B. K.; Watt, R. K.; Asplund, M. C.; Linford, M. R. *J. Am. Chem. Soc.* **2007,** *129* (30), 9252-9253.

5. Malmsten, M.; Emoto, K.; Van Alstine, J. M. *J. Colloid Interface Sci.* **1998,** *202* (2), 507-517.

6. Gombotz, W. R.; Guanghui, W.; Horbett, T. A.; Hoffman, A. S. *J. Biomed. Mater. Res.* **1991,** *25* (12), 1547-1562.

7. Saini, G.; Gates, R.; Asplund, M. C.; Blair, S.; Attavar, S.; Linford, M. R. *Lab on a Chip* **2009,** *9* (12), 1789-1796.

8. Budevska, B. O.; Sum, S. T.; Jones, T. J. *Appl. Spectrosc.* **2003,** *57* (2), 124-131.

9. de Juan, A.; Tauler, R. *Crit. Rev. Anal. Chem.* **2006,** *36* (3-4), 163-176.